Diss. ETH No. 30028

WATER SOLUBILITY IN MANTLE PHASES AND ITS EFFECT ON PHYSICAL PROPERTIES

A thesis submitted to attain the degree of

DOCTOR OF SCIENCES
(Dr. sc. ETH Zurich)

presented by

THOMAS THÉODORE MAXIMILIEN DE SELVA-DEWINT
MSc ETH in Earth Sciences

born on 13.12.1996

accepted on the recommendation of

Prof. Dr. M. Murakami, examiner
PD Dr. A. Khan, co-examiner
Prof. Dr. K. Ohta, external co-examiner

2024

To Noah

Abstract

Water is essential for our species' survival on this planet and its behavior and presence inside of the Earth has been a topic of interest for many years. On the Earth's surface water is ubiquitous and calculating its quantity is relatively straight-forward. Determining the quantities present in the Earth's deep interior is much more challenging. To investigate the current water content of the Earth's mantle, a combined experimental and geophysical approach is required. The solubility of water and its effect on the physical properties of mantle minerals has to be disentangled by laboratory experiments. These results can then be compared to geophysical observations of Earth's mantle to assess the presence of water.

This work contributes to the understanding of the water presence in the interior of Earth and rocky planets in general. The first part of this thesis consists of investigating the presence of water in bridgmanite and its effect on elasticity, as will be explained in Chapter 2. Bridgmanite is the major mantle phase in the Earth's lower mantle, and its water solubility has been a controversial topic for the past 20 years. By using a combination of Fourier Transform Infrared Spectroscopy and Atom Probe Tomography, the presence of hydrogen in the crystal lattice of bridgmanite is confirmed in this work. The first measurements of shear wave velocity in a hydrous bridgmanite sample containing ∼1054 ppm wt H_2O and 3.44 wt.% Al_2O_3 are presented. These measurements indicate that the presence of water in bridgmanite causes the material to stiffen, expressed as a 6% decrease in shear modulus (G_0), and a 5% increase in the first pressure derivative of G_0 (G_0'). Modeling the effect of water on the velocity profile of the lower mantle and comparing it to known geophysical reference models like the Preliminary Reference Earth model, shows that no significant amount of water is to be expected however.

Secondly, the phase transition from stishovite to $CaCl_2$-type SiO_2 is studied using Brillouin Scattering Spectroscopy. The phase transition is found to take place at ∼30 GPa, which is lower than most previous studies on this topic. The possible reasons for this are examined in Chapter 3 of this work, and its implications on geophysical interpretations for this phase transition are discussed. Most importantly, this result suggests that mantle scatterers at a 1000–1200 km depth range could be explained by the phase transition.

The last part of this thesis consisted in developing a method to optimize thermodynamic parameters used in geophysical modeling to better represent experimental results. Thermodynamic databases used for studies of the deep interior have thus far never included the established effect of water on mantle phases' stability and physical properties. Preliminary results of solving this issue are given in Chapter 4.

Résumé

L'eau est essentielle à la survie de notre espèce sur cette planète et son comportement et sa présence à l'intérieur de la Terre sont un sujet d'intérêt depuis de nombreuses années. À la surface de la Terre, l'eau est omniprésente et le calcul de sa quantité est relativement simple. Déterminer les quantités présentes dans les profondeurs de la Terre est beaucoup plus difficile. Pour étudier la contenu actuel en eau du manteau terrestre, une approche expérimentale et géophysique combinée est nécessaire. La solubilité de l'eau et son effet sur les propriétés physiques des minéraux du manteau doivent être identifiés par des expériences en laboratoire. Ces résultats peuvent

ensuite être comparés aux observations géophysiques du manteau terrestre afin d'évaluer la présence d'eau.

Ce travail vise à contribuer à la compréhension de la présence d'eau à l'intérieur des planètes rocheuses. La première partie de cette contribution a consisté à étudier la présence d'eau dans la bridgmanite et son effet sur son élasticité, comme sera expliqué dans le Chapître 2. La bridgmanite est la principale phase du manteau inférieur de la Terre, et sa solubilité de l'eau est un sujet controversé déjà depuis 20 ans. En combinant la Spectroscopie Infrarouge à Transformée de Fourier et la Tomographie par Sonde Atomique, la présence d'hydrogène dans la structure cristalline de la bridgmanite est confirmée par ce travail. Les premières mesures de la vitesse des ondes transversales dans un échantillon de bridgmanite hydratée contenant containing ∼1054 ppm wt de H_2O et 3.44 wt.% de Al_2O_3 sont également présentées ici. Ces mesures indiquent que la présence d'eau dans la bridgmanite provoque une rigidification du minéral, exprimée par une diminution de 6% du module de cisaillement (G_0), et une augmentation de 5% de la première dérivée de pression de G_0 (G_0'). La modélisation de l'effet de l'eau sur le profil de vitesse du manteau inférieur et sa comparaison avec des modèles géophysiques de référence connus, tel que le Modèle Terrestre Préliminaire de Référence, montrent qu'il ne faut pas s'attendre à une quantité significative d'eau.

Secondement, la transition de phase entre la stishovite et la SiO_2 de type $CaCl_2$ est étudiée à l'aide de spectroscopie de diffusion Brillouin. La transition est détectée à ∼30 GPa, ce résultat est inférieur à ceux de la plupart des études précédentes sur ce sujet. Les raisons possibles de ce phénomène sont examinées dans le Chapître 3 de ce travail, et ses implications sur les interprétations géophysiques de cette transition de phase sont également abordées. Principalement, ces résultats suggèrent que les diffuseurs du manteau dans la gamme des 1000–1200 km de profondeur pourraient être expliqués par cette transition de phase.

La dernière partie de cette thèse a consisté à développer une méthode pour optimiser les paramètres thermodynamiques utilisés dans la modélisation géophysique, afin de mieux représenter les résultats expérimentaux. Les bases de données thermodynamiques utilisées pour les études de l'intérieur profond n'ont jusqu'à présent jamais inclus l'effet établi de l'eau sur la stabilité et les propriétés physiques des phases du manteau. Les résultats préliminaires de la résolution de ce problème sont présentés dans le Chapître 4.

Contents

Chapter 1

Introduction

1.1 The presence of water in the Earth's interior

In order to estimate how much water could be present in the Earth's interior, it is essential to understand how much would have been present during the planet's accretion. After this amount is determined, a comparison can be made between the current water mass of the hydrosphere and water content of Earth's building blocks in order to estimate how much water could be left in the interior. Chondrite meteorites for example, which are thought to have a similar overall composition to the Bulk Silicate Earth, contain ∼0.1 wt% of water (Smyth and Jacobsen, 2006). Comparing this concentration to the hydrosphere's water content would suggest that 75% of all the Earth's hydrogen should either have been lost through degassing or is still present inside of the planet, or a combination of both (Smyth and Jacobsen, 2006).

When looking at isotopes, Pd-Ag, Mn-Cr, and Rb-Sr chronometers can be used to trace the volatile evolution during planet formation (Schönbächler et al., 2010). This data suggests that a considerable amount of volatile-rich material would have to be available in building blocks during the later stages of Earth's accretion, a lot of which could still be present in the interior. The possibility of degassing, and therefore loss of hydrogen, is mostly relevant during the magma ocean stage of planet formation. In terrestrial planets like the Earth or Mars, this magma ocean stage is thought to have

lasted only about 5 to 10 Ma. Due to the high solubility and compatibility of water in silicate melt (Peslier et al., 2017), it is possible to retain a significant amount of water in the silicate mantles of all terrestrial planets (Elkins-Tanton, 2008). Only for melt fractions below ∼30% would hydrogen start degassing intently, a point at which a surface lid has been argued to already have been formed, thereby trapping most of the water into the planet's interior (Bower et al., 2022).

Several attempts have been made to quantify the current water content of the mantle. Studies thereby usually subdivide the mantle into its three parts: the upper mantle, transition zone, and lower mantle. Peslier et al. (2017) calculate that the upper mantle would contain 0.1 ocean masses, the transition zone 0.9–1.4 ocean masses, and the lower mantle 0.2–4.5 ocean masses, based on water contents in natural samples. Based on global geophysical observations, Ohtani (2020) estimate that the upper mantle would contain ∼0.4 ocean masses, the mantle transition zone ∼0.2–1 ocean masses, and the lower mantle <2 ocean masses.

To be comprehensive in regards of the total water content of Earth, the metal core plays an important role due to potential core-mantle water partitioning. The possibility of hydrogen incorporation into metallic melts has been a topic of much interest of the last few years. Results from partitioning experiments and ab-initio calculations diverge somewhat on whether hydrogen prefers to partition into a silicate or metal melt. Even though there is evidence for hydrogen being lithophile at low pressure (Clesi et al., 2018; Malavergne et al., 2019), increasing pressure makes it more siderophile (Li et al., 2020; Malavergne et al., 2019). An increase in temperature has been shown to have the opposite effect though, making hydrogen more lithophile again (Li et al., 2020).

The limiting factor in geophysical studies is usually the available experimental data wherein there are high uncertainties on the water content values. This is caused by the large discrepancies in the reported solubilities between works. Only through performing even more experiments in these different systems will a better understanding of the behavior of water in the Earth's interior be attained. In this work, only mantle minerals

are considered, the properties of which will be covered in detail in this introduction.

1.2 The effect of water on mineral physical properties

The hydration of silicate minerals is known to have an effect on many of its physical properties.

Discontinuities in the mantle are generally caused by phase transitions. Since the presence of water in a mineral has an effect on its Gibbs free energy, and thereby its thermodynamic stability field, the pressure and temperature at which a phase transition occurs change with varying water contents (Karato, 2006; Smyth and Frost, 2002; Wood, 1995). Liquidi and solidi of mantle minerals have been shown to decrease significantly due to the presence of water (Gaetani and Grove, 1998; Hirth and Kohlstedt, 1996; Mierdel et al., 2007), with important implications on the melting behavior of certain phases in the mantle. The phase transition from olivine to wadsleyite becomes broader when the presence of water in its crystal lattice is considered. The onset pressure of the phase transition is dictated by the water content in olivine, and will be lower than in a dry system. Experimental evidence has shown that water preferentially partitions into wadsleyite (e.g., Litasov et al., 2006), meaning that as the phase transition is taking place, the remaining olivine will slowly get depleted of its water content. As water content in olivine decreases, the pressure at which the phase transition ends will correspond to the 'dry' phase transition pressure, which is higher than in a wet system (Karato, 2006). The phase transition will therefore be 'dragged' over a larger pressure span and become broader. According to Smyth and Jacobsen (2006), the sharpness of the velocity jump observed seismically at 410 km depth would be in line with a hydrous wadsleyite containing 1.5 wt% after the transition.

Transport properties of materials such as electrical or thermal conductivity have also be shown to be affected by the presence of water (Huang et al., 2005; Karato, 1990; Simpson and Tommasi, 2005). Adding H_2O in olivine increases the electrical conductivity by a factor of 100 000 (Wang et al., 2006a). Electrical conductivity has been used as

a geophysical tool combined with electromagnetic sounding to investigate the water content of the Earth's mantle. Generally, the presence of hydrogen increases the electrical conductivity of mantle minerals (Karato, 2006). With regards to thermal conductivity, the addition of 0.7 wt% H_2O in olivine for example lowers its thermal conductivity by half (Chang et al., 2017), while the addition of 1.17 wt% H_2O into ringwoodite lowers it by 40% (Marzotto et al., 2020).

Rheological properties such as the viscosity, elasticity or anelasticity of materials have also been established to change with the addition of water. Adding H_2O into olivine reduces its viscosity by a factor of 140 (Hirth and Kohlstedt, 1996). This effect is often referred to as 'hydrolytic weakening' (Di Genova et al., 2023; Karato et al., 1986), could have significant consequences on global convection dynamics (Muir and Brodholt, 2018). Anelastic relaxation [1] of a material gets enhanced when water is added to it (Karato and Jung, 1998), therefore influencing the way seismic waves get attenuated when traveling through the mantle (Dodd and Fraser, 1965; Liu et al., 2023).

The property most of interest for the purpose of this study is elasticity. The elasticity of a material represents its 'stiffness' or compressibility, i.e., its ability to resist a distorting force and to return to its original size and shape after that force is removed. Elasticity has been shown to be affected by the presence of hydrogen in the crystal lattice of many minerals, the evidence of which will be presented in Section 1.4. The addition of a small amount of water into a mineral's crystal lattice seems to have a much more dramatic effect on its elastic properties, compared to the addition of a similar amount of other elements like Fe and Al contents or a small change in temperature. For example, at ambient pressure, the effect of adding 1 wt% of H_2O has the same effect on ringwoodite's shear modulus as increasing the temperature from 800 to 1000°C (Jacobsen et al., 2004; Wang et al., 2003). Elasticity is also a property that can be examined using seismology. Seismic wave velocities in the Earth's interior depend on the density of the material that they travel through, which will therefore reflect elasticity. The presence of hydrogen tends to reduce the bond-strength and density of

1. Describes the 'softness' of a material, i.e., how it reacts to non-elastic deformation.

a material, and therefore cause a reduction in seismic wave velocity Karato (2006).

The growing understanding of the link between chemistry and seismic velocities of mantle minerals challenges previous perceptions. The notion to attribute any change in velocity to differences in temperature in tomographic models is likely not realistic (Marquardt and Thomson, 2020). Low velocity anomalies can be caused by an increase in temperature, but the presence of Fe, Al, H or melts has a similar effect. It is only through a good understanding of how each of these parameters affects the elasticity of a given mineral, and subsequent combination of geophysical tools that conclusions can be drawn. Karato (2006) mentions that the combination of measuring seismic wave velocities, seismic wave attenuation, seismic anisotropy, discontinuity topography and sharpness is necessary to really understand what quantity of water could be present in the mantle.

1.3 Incorporation of water in the crystal lattice of mantle minerals

The phases present in the Earth's mantle are generally thought of as 'Nominally Anhydrous Minerals' (NAMs) and often referred to as such in the frame of studies examining their water content. They are called nominally anhydrous because they do not contain more than a few wt% H_2O an therefore do not explicitly have hydrogen in the structural formula, unlike for example amphiboles, serpentine, chlorite, and clay minerals. Hydrogen can be present in NAMs in two ways. The first possibility is that it is present under the form of molecular H_2O at the surface of the sample or along the sample grain boundaries. If water is only present in this form, no significant conclusions can be drawn regarding the Earth's interior, as water molecules would have been lost long before the material reaches significant depths. The second option is that hydrogen is present as 'structural' water, i.e. inside of the sample's crystal lattice. It would thus be present as H^+ or OH^-, bonded to another atom in the crystal. The hydrogen would thereby represent an 'imperfection' or so-called point-defect in the crystal. Three types

processes are usually described to be able to create such imperfections in the literature:

- **Creation of vacancies**: In this case, a major atom like Si^{4+} or Mg^{2+} that is supposed to be present in the crystal lattice has been missing since crystallization or has been removed by a chemical reaction that took place (Wright, 2006). The free site in the lattice can be taken up by one or more hydrogen atoms, depending on the charge balance. This type of imperfection has been shown to be an efficient way to incorporate hydrogen in olivine (Libowitzky and Beran, 1995).
- **Interstitial substitutions**: Here, a hydrogen atom is able to wriggle its way through the crystal lattice and bind to another atom while remaining in between the other atoms, i.e., not on a normal lattice site (Wright, 2006). Karato (2008) proposes that this process would become more significant as pressure increases, as it involves a smaller activation volume compared to water incorporation through vacancies.
- **Charge-balancing substitutions**: When an atom present in the crystal lattice gets replaced or 'substituted' by another and the charge of the new atom does not correspond to what is expected for that site. This generates the need for another atom to come in and even out the charge. For example, if an Al^{3+} atom substitutes a Si^{4+} atom on the tetrahedral site, an extra H^+ would be welcome in the lattice to restore the charge balance. In enstatite for example, the presence of Al has been shown to have a drastic effect on its water solubility (e.g. Rauch and Keppler (2002); Stalder (2002)). Another common substitution that takes place in mantle minerals is the Fe^{2+}/Fe^{3+} redox-exchange reaction, where the difference in charge can again be balanced by addition of H^+ or OH^- (Ingrin and Blanchard, 2006). This process has been described experimentally in clinopyroxene (Skogby, 1994) and olivine (Bell and Rossman, 1992).

In general, no matter on which site hydrogen is present, or whether it is interstitial, it is considered to be bonded to one of the oxygen atoms surrounding it (which are always present in silicates). The presence of water can therefore either be thought of

as H^+ being incorporated, or OH^-, but both are equivalent. The terms 'water' and 'hydrogen' are therefore synonymous in the context of this work.

1.4 Water solubility and its effect on mineral elasticity

Since several hydrous mantle phases are discussed both in Chapter 2 and 4 of this work, a more detailed review of previous research on hydrous mantle minerals follows hereafter. For each phase, previously reported water contents, incorporation mechanisms, partition coefficients relative to coexisting phases, and effects on elasticity are discussed. Understanding the partitioning of hydrogen between different mantle phases is important to be able to constrain which minerals would be the main water sinks of the mantle, and how phase transitions could be affected by the presence of water.

An important distinction has to be made between the maximum water storage capacity of minerals, and actual water storage in the mantle. The experimental results shown in this chapter tend to represent an upper limit to how much water can be incorporated. Only comparison to direct geophysical data will be able to unveil how much water could actually be present in those phases in the mantle.

Olivine

Olivine ($(Mg, Fe)_2SiO_4$) is the most important mineral in the Earth's upper mantle, making up ∼60% of its total volume (Hirose, 2006). It has an orthorhombic structure and belongs to the *Pbnm* space group. The Mg and Fe solid-solution endmembers of olivine are forsterite and fayalite respectively. Natural mantle olivines are usually found as diamond inclusions present in xenoliths inside of kimberlites. These olivines contain water contents ranging between 1 and ∼400 ppm (Bell and Rossman, 1992; Bell et al., 2003, 2004; Koch-Müller et al., 2006; Matsyuk and Langer, 2004; Miller et al., 1987; Mosenfelder et al., 2006). A chronological summary of the experimental works examining the incorporation of H_2O into the olivine structure is given in Table 1.1. Reported water contents are generally below 1 wt%, with the exception of some results

by Chen et al. (2002). Water contents in natural samples are generally smaller than those measured in synthetic samples from experiments.

The water solubility in olivine is affected by other elements being present in the crystal lattice. The amount of Fe was found to positively correlate with the water solubility in olivine (Mosenfelder et al., 2006; Zhao et al., 2004). This is probably due to the charge-balancing incorporation of H^+ when Fe^{3+} reduces to Fe^{2+} (Bell and Rossman, 1992).

Regarding the site occupancy of H^+ in olivine, both the octahedral (Mg^{2+}/Fe^{2+}) (ichiro Karato, 2015; Manghnani et al., 2013; Mosenfelder et al., 2006; Otsuka and ichiro Karato, 2011) and tetrahedral Si^{4+} (Kovács et al., 2010; Lemaire et al., 2004; Umemoto et al., 2011; Xue et al., 2017) sites have been proposed as options for the incorporation of hydrogen. Based on the coupling behavior of Raman modes, Hushur et al. (2009) finds that out of the two octahedral M1 and M2 sites, M1 is the more likely to have a vacancy. Ab-initio computational simulations have shown that the most energetically favorable way of having hydrogen point defects in the olivine crystal lattice is most likely through vacancies of the Mg^{2+} sites (Brodholt, 1997; Churakov et al., 2003; Kudoh, 2008).

Experimentally determined partitioning coefficients [2] of hydrogen between olivine and wadsleyite range between a $D^{wad:ol}$ of 4:1 and 11:1 in favor of wadsleyite (e.g., Litasov et al., 2006). Water systematically prefers to partition into wadsleyite, no matter the pressure and temperature. As a consequence, the stability field of wadsleyite would grow at the expense of olivine at higher water fugacities (Chen et al., 2002; Smyth and Frost, 2002; Smyth and Jacobsen, 2006). This means that in regions with higher water contents, the 410 km discontinuity, related to wadsleyite formation, would become shallower.

Mao et al. (2010) used Brillouin scattering to investigate both the shear and bulk moduli of hydrous forsterite with 0.9 wt% H_2O up to 14 GPa, and observed that

2. Represent the ratio $D^{A:B}$ of concentrations of a certain element in two coexisting minerals at equilibrium.

Table 1.1 – Water contents in olivines.

Mg#	P (GPa)	T (K)	H_2O (wt%)	Method	Reference
90	2.5–13	1273–1373	0.01–0.15	FTIR	Kohlstedt et al. (1996)
100	1.5	1273–1373	0.18	NMR	Kohn (1996)
90–100	13–15	1473	0.2–3.5	SIMS	Chen et al. (2002)
83–100	$\sim$ 0.3	1273–1573	0.01–0.16	FTIR	Zhao et al. (2004)
97–100	12	1523–1873	0.10–0.89	FTIR	Smyth and Jacobsen (2006)
90–100	2–12	1273–1573	0.03–0.64	FTIR	Mosenfelder et al. (2006)
90	12.5–14	1473–1773	0.14–0.18	FTIR	Litasov et al. (2006)
90	4	873–1273	0.01–0.08	FTIR	Wang et al. (2006a)
90–95	12.5–14	1373–2273	0.02–0.62	FTIR	Litasov et al. (2007b)
100	7–13	1373–1573	0.07–0.43	SIMS	Withers and Hirschmann (2007)
92–95	8	1673–1873	0.03–0.15	FTIR	Withers and Hirschmann (2008)
100	2.5–9	1273–1673	0.01–0.20	FTIR	Bali et al. (2008)
100	12	1523	0.89	FTIR	Hushur et al. (2009)
89–98	8–14	1573–2273	0.10–0.54	FTIR	Litasov et al. (2009)
90	3–5	1623–1713	0.09– 0.11	SIMS	Tenner et al. (2009)
50–100	3	1473–1773	0.01–0.08	FTIR	Withers et al. (2011)
90	5–8	1673–1773	0.01–0.02	SIMS	Ardia et al. (2012)
90	10–12	1623–1723	0.03–0.09	SIMS	Tenner et al. (2012)
87–94	2.5–9	1448–1673	0.01–0.21	FTIR	Férot and Bolfan-Casanova (2012)
100	8	1523	0.05–0.30	FTIR	Fei and Katsura (2020)
90	3–5	1373–1573	0.03–0.09	FTIR	Kang and Karato (2023)

Short forms: FTIR–Fourier Transform Infrared Spectroscopy; NMR–Nuclear Magnetic Resonance spectroscopy; SIMS–Secondary Ion Mass spectroscopy.

both moduli increase at a greater rate compared to their anhydrous counterparts, i.e. the hydrous component becomes stiffer faster. An increase of 7% in K_0' and 25% in G_0' is reported. The acoustic velocities of hydrous forsterite start off lower compared to dry forsterite, but a cross-over occurs around 3–4 GPa. Below this point located at $\sim$120 km, acoustic velocities in hydrous forsterite are faster than its anhydrous counterpart. Jacobsen et al. (2008) determined based on their experiments that the combined effect of adding 3 mol% Fe and 0.8 mol% H_2O reduced the shear and bulk moduli by 7.5% and 3.5% respectively. More recently, Faccincani et al. (2023) examined the acoustic velocities of $Mg_{0.9}Fe_{0.1}SiO_4$ with 0.2 wt% H_2O, and reported no significant difference in the bulk and shear modulus compared to its anhydrous counterpart. The K_0' and G_0' were observed to increase by $\sim$2.5–5% due to the presence of H_2O.

The experiments on the elasticity of mantle minerals and their reported water contents

were not added to Table 1.4, because they often do not represent equilibrium conditions, and therefore do not reflect equilibrium solubilities of these minerals at the conditions investigated. This is also valid for all other sections in this chapter.

Pyroxene

Pyroxenes represent a large group of minerals, which can generally be subdivided into two major groups: orthopyroxenes which are orthorhombic, and clinopyroxenes which are monoclinic. They can by described with the general formula $XYSi_2O_6$, where X and Y are cation sites available for elements such as Mg, Fe, Ca, and Na depending on the pyroxene in question. Pyroxenes are a major mineral in the Earth's crust and some varieties are stable well into the upper mantle. Below ∼400 km the mineral will transform to garnet.

The pyroxene varieties stable at upper mantle conditions either have the composition $(Mg, Fe)_2Si_2O_6$, which represents the enstatite – ferrosilite solid solution when it is orthorhombic (*Pbca* space group), and clinoenstatite – clinoferrosilite solid solution when monoclinic ($P2_1/b$ space group), or $Ca(Mg, Fe)Si_2O_6$, which represents the monoclinic diopside – hedenbergite solid solution ($B2/b$ space group). At lower temperatures found in subduction zones, jadeite ($Na(Al, Fe^{3+})Si_2O_6$, $B2/b$ space group) and omphacite [2] would also be able to form at upper mantle pressures.

The water solubility in pyroxene at upper mantle conditions has been studied experimentally. A summary of previous works is given in Table 1.2, which shows that water concentrations are generally not exceeding 1 wt%. In enstatite, the presence of Al has been shown to have a major effect in increasing its water solubility (Andrut et al., 2003; Koch-Müller et al., 2004; Mierdel and Keppler, 2004; Peslier, 2010; Rauch and Keppler, 2002; Sakurai et al., 2014; Stalder, 2002), with the solubility reaching up to 1 wt% at 15 kbar and 800°C (Mierdel and Keppler, 2004). Withers and Hirschmann (2007) report an increase in the water content of clinopyroxene with increasing pressures, going from 0.08 wt% H_2O at 8 GPa to 0.67 wt% at 13.4 GPa, but this effect gets diminished

2. $(Na, Ca, Fe^{2+}, Mg)(Al, Fe^{3+}, Fe^{2+}, Mg)Si_2O_6$

at higher temperatures. Bromiley and Keppler (2004) however observe an opposite effect of pressure, describing a decrease in water content with increasing pressure and temperature. A partition coefficient $D^{ol:en}$ of 0.65:1 and 0.87:1 was found in this study, showing that water preferentially partitions into pyroxene compared to olivine. When measuring the partitioning of water between Al-bearing enstatite and olivine, Sakurai et al. (2014) measured even higher values with coefficients going up to 35:1 in favor of pyroxene. Kang and Karato (2023) found a $D^{ol:cen}$ ranging between 1:0.88 and 1:3.20 between 3 and 5 GPa, again confirming mostly the same behavior (only 2 out of 24 measurements had a $D^{cen/ol}$ below 1).

Table 1.2 – Water contents in pyroxenes.

Endmember	P (GPa)	T (K)	H_2O (wt%)	Method	Reference
Clinoenstatite	15.5	1473–1573	0.6–0.8	FTIR	Inoue et al. (1995)
Clinoenstatite	15	1773	0.06	FTIR	Bolfan-Casanova et al. (2000)
Enstatite	7.5	1373	0.09	FTIR	Rauch and Keppler (2002)
Clinoenstatite	13–14	1673–1773	0.32–0.45	SIMS	Yamada et al. (2004)
Enstatite	1.5–3.5	1073–1373	0.1–0.7	FTIR	Mierdel et al. (2007)
Clinoenstatite	8–13	1373–1673	0.08–0.67	SIMS	Withers and Hirschmann (2007)
Enstatite	2–5	1623–1713	0.08–0.14	SIMS	Tenner et al. (2009)
Enstatite	6	1473	0.04–0.08	SIMS	Withers et al. (2011)
Ortho- & Clino-En	2.5–9	1448–1673	0.01–0.13	FTIR	Férot and Bolfan-Casanova (2012)
Clinoenstatite	10–13	1673–1723	0.06–0.15	SIMS	Tenner et al. (2012)
Enstatite	1.5–6	1573–1723	<0.01	FTIR	Sakurai et al. (2014)
Al-enstatite	1.5–6	1573–1723	<0.01–0.04	FTIR	Sakurai et al. (2014)
Enstatite	0.2–3	1073–1473	<0.01–0.03	FTIR	Liu and Yang (2020)
Clinoenstatite	0.2–3	1073–1473	<0.01–0.02	FTIR	Liu and Yang (2020)
Fe-Enstatite	3-5	1373–1573	0.04-0.13	FTIR	Kang and Karato (2023)

Short forms: FTIR–Fourier Transform Infrared Spectroscopy; SIMS–Secondary Ion Mass spectroscopy.

Natural pyroxenes like jadeite and diopside have commonly been found to contain 0.01–0.13 wt% H_2O (Skogby et al., 1990). In diopside, the fact that two sites can commonly have substitutions leading to charge imbalances (Al instead of Si, and Na instead of Ca), has been thought be the an important facilitating factor to the incorporation of hydrogen. The highest water contents found in natural mantle xenoliths, have come from pyroxenes (mostly omphacites; Bell and Rossman, 1992; Bell et al., 2004;

Bolfan-Casanova, 2005; Skogby, 2006), which strongly supports the idea that pyroxene would be the NAM with the highest water content in the upper mantle. However, their lower modal abundance compared to olivine could still result in most of the upper mantle's water being stored in olivine (Keppler and Bolfan-Casanova, 2006). Pyroxenes have a larger modal abundance in subduction slabs though, increasing their relevancy in such settings.

A few studies have examined the effect of hydrogen on the elasticity of pyroxenes. Gavrilenko et al. (2010) investigated the effect of the incorporation of Al and H on the bulk modulus and its first derivative in Diopside using X-ray diffraction up to 10 GPa. They observed increases in both K_0 and K_0' in diopside upon the addition of Al. The addition of water seemed to have a similar, but lesser effect compared to Al. Jacobsen et al. (2010) showed that the incorporation of 1300 ppm H_2O in pyroxene lowers the phase transition from low-pressure clinoenstatite to high-pressure clinoenstatite by 2 GPa, which could explain certain seismic reflectors in the upper mantle. Mans et al. (2019) measured the elasticity of natural omphacite containing ∼710 ppm H_2O at ambient conditions and found that it does not have an effect on its elastic moduli. Hou et al. (2022) also found that only the C_{13} & C_{23} elastic moduli are affected significantly when adding 842–900 ppm H_2O and 1.64 wt% Al_2O_3 into enstatite, but not G_0 and K_0.

Garnet

Garnets are a large mineral group that can be represented with the formula $X_3Y_2(SiO_4)_3$. In the frame of high-pressure studies, two endmembers are mostly relevant: pyrope ($Mg_3Al_2(SiO_4)_3$, $Ia3d$ space group in the cubic crystal system) and majorite ($Mg_3(MgSi)(SiO_4)_3$, $I41/a$ space group in the tetragonal crystal system). Mantle garnets are often thought to lie somewhere between those two endmembers. Garnet makes up ∼15 vol% of the upper mantle right below the Moho, but gradually becomes more abundant as pyroxene decomposes to garnet, and reaches 40 vol% in the transition zone (Hirose, 2006), before completely decomposing to bridgmanite in the shallow lower

mantle at ∼750 km.

Experiments on the solubility of water in high-pressure garnets are quite scarce, but the few that exist are represented in Table 1.3. This data shows that garnet is not able to take up that much water compared to previously discussed phases (< 0.13 wt%), probably making it the driest phase in the upper mantle and transition zone. Partition coefficients $D^{ol:grt}$ between garnet and olivine reported in these studies vary between 0.14:1 and 2.5:1, mostly in favor of olivine. Partition coefficients $D^{grt:px}$ between garnet and pyroxene determined by Tenner et al. (2009) at 5 GPa and 1713 K are 5.6:1 and 14:1 in favor of pyroxene.

Table 1.3 – Water contents in garnets.

Endmember	P (GPa)	T (K)	H_2O (wt%)	Method	Reference
Pyrope	2–5	1073–1273	0.02–0.07	FTIR	Geiger et al. (1991)
Pyrope	1.5–10	1073–1273	<0.01–0.02	FTIR	Lu and Keppler (1997)
Pyrope	2–13	1273	0.00–0.10	FTIR	Withers et al. (1998)
Majorite	17.5	1773	0.07	FTIR	Bolfan-Casanova et al. (2000)
Majorite	20	1673–1773	0.11–0.13	SIMS	Katayama et al. (2003)
Pyrope	5	1713	0.01–0.03	SIMS	Tenner et al. (2009)
Pyrope-rich	5–9	1373–1473	<0.01–0.06	FTIR	Mookherjee and Karato (2010)
Pyrope	1–3	1073–1273	<0.01	FTIR	Zhang et al. (2022b)

Short forms: FTIR–Fourier Transform Infrared Spectroscopy; SIMS–Secondary Ion Mass spectroscopy.

Crustal garnets like grossular and spessartine are known to be able to incorporate up a few wt% of water due to the so-called hydrogarnet substitution mechanism where four H^+ replace a Si^{4+} (Cohen-Addad et al., 1967; Kobayashi and Shoji, 1983; Sheng et al., 2007; Xia et al., 2005). Natural pyrope samples however have very low contents, with the famous Dora Maira pyrope containing only 58 ppm for example (Rossman et al., 1989). This observation, combined with the very low water contents found in garnet experimentally led to the idea that the hydrogarnet mechanism would only be relevant for Ca-bearing garnets, and not be sustainable at higher pressures (Bolfan-Casanova et al., 2000). Calculations by Pigott et al. (2015) however suggest that even if water contents in majorite at high pressures are very low, the most favorable substitution

mechanism remains the hydrogarnet substitution. Smyth et al. (2005) also suggested that H would prefer to fill the tetrahedral Si site.

Fan et al. (2017) studied the elasticity of pyrope containing 900 ppm H_2O using X-ray diffraction and found that the bulk modulus K_0 decreases by 7%, paired with a slight increase in K_0'. When measuring a pyrope sample with the same water content using Brillouin scattering up to 18 GPa and 700 K, Fan et al. (2019) found that K_0, G_0 and G_0' do not change significantly compared to anhydrous pyrope. Only K_0' was found to increase by ∼2%.

Wadsleyite

Wadsleyite ($(Mg, Fe)_2SiO_2$) is a high pressure polymorph of olivine and marks the beginning of the transition zone by forming at a depth of 410 km. It has an orthorhombic crystal structure, like olivine, but is part of space group: $Imma$ (Price et al., 1983). The incorporation of water into wadsleyite has been established to change its crystal symmetry to monoclinic, transforming to the space group $I2/m$ (Smyth et al., 1997).

Table 1.4 shows a summary of the water solubility studies on wadsleyite throughout the years. The water contents from these studies are often above 1 wt% and go up to 2–3 wt%. These contents are large in comparison to the results for e.g. olivine in Table 1.1. Indeed, wadsleyite is believed to be the mantle phase that is capable of incorporating the largest quantity of H. The reason for this is thought to be related to the fact that the wadsleyite structure contains an 'underbonded', non-silicate oxygen atom (O1), with which H could more easily form a bond (Smyth et al., 1997). Ab-initio studies have confirmed that hydrogen is indeed most likely to bind to the O1 atom (Haiber et al., 1997), and that vacancies of the Mg^{2+} site are energetically most favorable as a position for hydrogen (Walker et al., 2006). Out of the octahedral Mg^{2+} sites, M3 is the best candidate for water to be present, as it is the closest to the O1 atom. Hydrogen partition coefficients of wadsleyite in equilibrium with other mantle phases are reported in the sections pertaining to the latter.

Experiments have shown that the water content in wadsleyite decreases with increasing temperature (Bolfan-Casanova, 2005; Demouchy et al., 2005; Hirschmann et al., 2005; Litasov and Ohtani, 2007). Reports on the effect of pressure vary however, with Demouchy et al. (2005) reporting no effect, and Litasov and Ohtani (2007) reporting a decrease in water concentration with increasing pressures. These results suggest that the transition zone is likely to be more hydrated towards the top.

The presence of water in the crystal structure of wadsleyite has been proven to have an important effect on its elasticity. The bulk modulus of wadsleyite has been found to decrease by almost 10% and the density by 3% with the addition of 2.5 wt% H_2O (Yusa and Inoue, 1998). Mao et al. (2008) measured Mg-wadsleyites with different water contents and reported a linear decrease of its elastic moduli. The addition 1 wt% H_2O led to a decrease of 7% and 7.6% in the shear and bulk moduli respectively. Later, Mao et al. (2011) measured the effect of water on the elasticity of Fe-bearing wadsleyite and observed a decrease of 9.3% and 8.1% for G_0 and K_0 respectively when adding 1.93 wt% H_2O. The decrease in shear wave velocities was not linear this time, with a reported increase in G_0' of 20%. Buchen et al. (2018) reports a decrease of 10% and 1.5% for G_0 and K_0 using a wadsleyite sample with similar Fe content and 0.24 wt% H_2O. They report an increase of 17% in G_0' and decrease of 4% in K_0'. Finally, Zhou et al. (2021) measured an Fe-bearing sample containing 0.14 wt% H_2O and describes a decrease of 10% and 2% for G_0 and K_0 respectively compared to the dry Mg-endmember. An increase of 35% and 20% in G_0' and K_0' is reported.

Ringwoodite

Ringwoodite ($(Mg, Fe)_2SiO_2$) is another polymorph of olivine. It was first found in nature in the Tenham meteorite by Binns et al. (1969) and described to be part of the cubic crystal system, more specifically the $Fd\bar{3}m$ space group. If forms from wadsleyite at ∼520 km depth, and makes up ∼60% of the deeper half of the transition zone Hirose (2006). A summary of previous experimental studies measuring the solubility of water in ringwoodite is given in Table 1.5. Similar to wadsleyite, water contents are commonly

Table 1.4 – Measured water contents in wadsleyite.

Mg#	P (GPa)	T (K)	H_2O (wt.%)	Method	Reference
90	14–15	1373	2.13–2.41	FTIR	Kohlstedt et al. (1996)
83	13.5–16.5	1573–1773	1.52–2.89	SIMS	Kawamoto et al. (1996)
90	17.5	1673	2.24	FTIR	Smyth et al. (1997)
100	15	1573	0.22	FTIR	Bolfan-Casanova et al. (2000)
91	13–14.4	1473	1.90–3.40	SIMS	Chen et al. (2002)
100	16–18	1673–2373	0.01–1.06	FTIR	Jacobsen et al. (2005)
100	15	1173–1673	0.93–2.6	SIMS	Demouchy et al. (2005)
90	12.5–14	1473–1773	0.67–1.77	FTIR	Litasov et al. (2006)
89	12–20	1473–2273	0.07–2.12	FTIR	Litasov and Ohtani (2008)
100	14–20	1473–2173	0.22–2.07	FTIR	Litasov et al. (2011)
83–100	15–19	1473–1923	0.16–3.11	ERDA	Bolfan-Casanova et al. (2018)
90	16	1923	0.95	FTIR	Sun et al. (2018)
100	17	1673	0.61–1.25	FTIR	Druzhbin et al. (2021)
75–100	17.5–20	1500–2100	0.58–2.42	FTIR	Fei and Katsura (2021)

Short forms: FTIR–Fourier Transform Infrared Spectroscopy; SIMS–Secondary Ion Mass spectroscopy. ERDA–Elastic Recoil Detection Analysis.

higher than 1 wt% (Tab. 1.4), and clearly higher than olivine (Tab. 1.1). Also like in wadsleyite, Mg^{2+} site vacancies seem to be the most common way to incorporate water in ringwoodite (Kudoh et al., 2000), but substitutions on the Si^{4+} have also been argued to be possible (Ye et al., 2012).

Higher Fe contents in ringwoodite increase the amount of water that can be incorporated (Bodnar et al., 2013). Experiments on the partitioning of water between wadsleyite and ringwoodite consistently show that wadsleyite is able to take up more water compared to ringwoodite, with Inoue et al. (2010) reporting partition coefficients $D^{wd/rw}$ ranging between 1.63:1 and 2.2:1. These values decrease somewhat towards higher temperatures though, as the solubility of water in ringwoodite decreases more slowly compared to wadsleyite with increasing temperatures (Demouchy et al., 2005; Ohtani et al., 2000). This would have implications for the exact depth of the 520 km discontinuity, that could thus become shallower in hotter areas of the mantle.

Aside from the meteoritic sample, a natural ringwoodite sample was first found as a diamond inclusion in a kimberlite from Juína, Brazil (Pearson et al., 2014), containing 1 wt% H_2O. This water content aligns with experimental observations and suggests

Table 1.5 – Measured water contents in ringwoodite.

Mg#	P (GPa)	T (K)	H_2O (wt.%)	Method	Reference
100	15.5	1473–1573	1.10–3.10	SIMS	Inoue et al. (1995)
90	14–15	1373	2.13–2.41	FTIR	Kohlstedt et al. (1996)
100	19	1200–1300	0.06–0.78	FTIR	Bolfan-Casanova et al. (2000)
100	20–23	1573–1723	0.20–2.60	SIMS	Ohtani et al. (2000)
88–100	18–22	1673–1773	0.20–1.07	FTIR	Smyth et al. (2003)
90	24	1673	0.14	FTIR	Bolfan-Casanova et al. (2003)
6–100	19–22	1573–1973	0.02–1.83	ERDA	Bolfan-Casanova et al. (2018)
75–100	23	1600–2000	0.25–2.03	FTIR	Fei and Katsura (2020)

Short forms: FTIR–Fourier Transform Infrared Spectroscopy; SIMS–Secondary Ion Mass spectroscopy. ERDA–Elastic Recoil Detection Analysis.

that the transition zone might indeed at least locally contain a considerable amount of water, as this sample would be coming directly from it. Pearson et al. (2014) proposes two scenarios for the formation of this ringwoodite. Either it formed syngenetically with the diamond from a hydrous fluid at transition zone depth, or it is protogenetic and representative of the actual water content of ringwoodite in the transition zone.

As for olivine and wadsleyite, Brillouin measurements on ringwoodite show a consistent drop in the shear and bulk moduli when water is present. Inoue et al. (1998) observed a drop of 10% and 16% in shear and bulk moduli respectively upon hydration of 2.3 wt%. Wang et al. (2003) also examined a sample containing 2.3 wt% at ambient conditions, but found ess pronounced drops of 3.6% and 10% for the shear and bulk modulus respectively. When measuring an iron-bearing ringwoodite sample with 1 wt% of H_2O, Jacobsen et al. (2004) observed a drop of 6% and 13% in shear and bulk moduli respectively. Wang et al. (2006b) also studied the behavior of Mg-ringwoodite containing 2.3 wt% at higher pressure and described an increase of 7% for the K_0' and 30% for G_0'. Jacobsen and Smyth (2006) confirms an increase of K_0' and G_0' by 30% and 53% respectively when investigating ringwoodite containing 1 wt% H_2O and 10 mol% FeO, which would cause the velocities of hydrous ringwoodite to cross the anhydrous trend around 12 GPa. Mao et al. (2012) studied an Fe-bearing sample with 1.1 wt% H_2O and report that the elastic moduli of ringwoodite get reduced by 5–9% at ambient conditions, but no effect was found on the pressure derivatives of

these moduli. An effect of increasing temperature is observed though, causing an even stronger decrease of the moduli (1.3–2.4% for every 100 K). Schulze et al. (2018) measured different samples with water contents ranging between 0.21 wt% and 1.71 wt% and Mg# between 89 and 100. According to these results, a sample containing 9 mol% and 1.5 wt% H_2O would cause a reduction of 8.5% in G_0, 8% in K_0, and an increase of 19% in G_0' and 11% in K_0'.

Bridgmanite

Bridgmanite ($(Mg, Fe)SiO_3$) is be part of the *Pnma* space group in the orthorhombic crystal system and was first found in nature in a shocked meteorite (Tschauner et al., 2014). It is thought to make up 80–90% of the lower mantle, along with ferropericlase and davemaoite. Bridgmanite transforms into post-perovskite at the very bottom of the lower mantle at ∼120 GPa or 2600 km depth. The presence of water in these minerals is understudied when compared to the upper mantle or transition phases. For a full review of previous works studying the incorporation of water into bridgmanite, see Chapter 2. **?** investigated the partitioning of water between bridgmanite and other possible coexisting mantle phases computationally. The partition coefficient $D^{ring:brg}$ between ringwoodite and bridgmanite was reported to be 10-13:1 in favor of ringwoodite, which is quite close to the experimental result of 15:1 by Inoue et al. (2010).

How the presence of water influences the partitioning of Fe and Al between bridgmanite and a coexisting melt phase has been investigated by a few studies performing high pressure melting experiments. When comparing the results of Al-bearing and Al-barren bridgmanite experiments, performed under dry (Boujibar et al., 2016; Corgne et al., 2005; Ito et al., 2004) and wet (Amulele et al., 2021; Kawamoto, 2004; Nakajima et al., 2019) conditions, results show that when no Al is present, the partitioning is not significantly affected by the presence of water (Amulele et al., 2021). In Al-bearing systems though, a clear increase in the partition coefficients $D^{brg:melt}_{Fe/Mg}$ and $D^{brg:melt}_{Si/Mg}$ is reported at wet conditions, making the bridgmanite enriched in Fe and Si and the

melt enriched in Mg compared to dry conditions. Thus, the presence of both Al and H seems to be necessary to affect the chemistry of bridgmanite.

When considering that the addition of Fe, Al or H have an effect on physical properties of bridgmanite, it is not unreasonable to consider it would also have an influence on the phase boundary between ringwoodite and bridgmanite. Different elements seem to have varying effects, with Fe causing a shift of the phase boundary to lower pressures (Ito and Takahashi, 1989), while the addition of Al and H causes a shift to higher pressures (Bolfan-Casanova, 2005; Ghosh et al., 2013; Weidner and Wang, 1998). Ghosh et al. (2013) specifically report a shift at 1800 K from 22 GPa in dry $MgSiO_3$ to 23.4 GPa in a $MgSiO_3$ sample where 2 wt.% H_2O was added to the starting material. The water concentration of the resulting bridgmanite is not reported.

Ferropericlase

Ferropericlase ((Mg,Fe)O), is part of the $Fm3m$ space group of the cubic crystal system. Around 10 vol% of this phase is thought to be present in lower mantle (Hirose, 2006), but the exact amount depends on how much bridgmanite is present. Reported solubilities of water in ferropericlase are wide-ranging. Murakami et al. (2002) found that 1900 ppm of H_2O would be present in periclase (MgO) at 25.5 GPa and 1600°C. To the contrary, Bolfan-Casanova et al. (2000) reports only ∼2 ppm wt of H in periclase at 24 GPa and 1500°C and Bolfan-Casanova et al. (2002) reported 20 ppm H_2O in ferropericlase at 25 GPa and 2000°C.

Litasov et al. (2003) reported a maximum water content of 180 ppm in Al-bearing ferropericlase at 25 GPa and 1800°C . When performing experiments at 25 GPa and 1400–2000°C, Litasov (2010) found that periclase containing 0.9–1.2 wt% Al_2O_3 could incorporate 11–25 ppm H_2O, and ferropericlase containing 0.9–2.9 wt% Al_2O_3 could take up 14–79 ppm H_2O. Presence of Al thus seems to have an effect on the water content, even though it remains very low. Yang et al. (2023) recently suggested that the reaction of water with ferropericlase would create periclase (MgO) + xFeOOH ('Pyrite-phase') + H_2 based on Laser Heated Diamond Anvil Cell (LHDAC) experiments

performed at 95–121 GPa and 2000–2250 K. The partition coefficient $D^{brg:fp}$ between bridgmanite and ferropericlase was found to be 90:1 in favor of bridgmanite in that study. Ab-initio experiments confirm that water would indeed preferentially partition into bridgmanite (**?**).

Davemaoite

Davemaoite is part of the $Pm3m$ space group of the cubic crystal system, and has the chemical composition $CaSiO_3$. It could make up a few vol.% of the lower mantle (Hirose, 2006). Davemaoite was originally suggested to be able to contain 4000 ppm wt H_2O in experiments by Murakami et al. (2002). Keppler and Bolfan-Casanova (2006) and Hirschmann (2006) suggested that the phase would be dry however. Németh et al. (2017) suggested their samples could contain 0.58–3.05 wt% H_2O based on Electron Probe Micro-Analyzer (EPMA) measurements, but were not able to measure FTIR due to the amorphization of the sample upon quenching. Chen et al. (2020) performed in-situ FTIR measurements on a LHDAC at 19–120 GPa and 1400–2200 K, and detected a significant amount of water ranging 0.5–1 wt%. These high water contents prompted the undertaking of a Density Functional Theory study by Shim et al. (2022) to understand the water incorporation mechanisms into the crystal lattice of davemaoite. The conclusion of this study was that H^+ would be incorporated directly through substitution of $2H^+$ on the Ca^{2+} site or $4H^+$ on the Si^{4+} site, rather than through charge-balancing substitution.

Stishovite

Stishovite has the composition SiO_2 and is part of the $P4_2/mnm$ space group of the tetragonal crystal system. No significant amount of stishovite is thought to be present in the Earth's mantle, except for subduction slabs where it could make up to 20 vol.% of the mineral assemblage (Hirose, 2006). SiO_2 goes through two phase transitions, to $CaCl_2$-type SiO_2 and later α-PbO_2-type SiO_2 at lower mantle conditions. This is described in more detail in Chapter 3. Pawley et al. (2019) established quite early that

even though pure SiO_2 is not able to contain a lot of water (∼500 ppm), the addition of Al in stishovite increases its water solubility significantly (1.5 wt%). This would again be due to charge-balanced substitution of Si^{4+} by Al^{3+} and H^+. Experiments by Chung and Kagi (2002) and Litasov et al. (2007a) found 844 ppm H_2O at 15 GPa and 1700 K, and 3010 ppm at 20 GPa and 1700 K respectively in Al-bearing samples. Based on these results, stishovite could be an important water carrier in subduction slabs. The presence of H_2O in SiO_2 has also been found to have an effect on the transition pressure of stishovite to $CaCl_2$-type SiO_2 (Criniti et al., 2023; Lakshtanov et al., 2007; Nisr et al., 2017; Zhang et al., 2022c), which is further discussed in Chapter 3. Zhang et al. (2022c) recently measured that the presence of Al and H in stishovite causes the shear wave velocity to drop by 29%.

Post-perovskite

Post-perovskite has the composition $MgSiO_3$ and is part of the *Cmcm* space group of the orthorhombic crystal system. The effect of water on the elasticity of post-perovskite has not been investigated experimentally, and only a first-principle study exists by Townsend et al. (2016). This study investigated hydrogen partitioning between bridgmanite and post-perovskite, and found that in a Al-free system bridgmanite is favored 5:1 compared to post-perovskite, but in a Al-bearing system post-perovskite is favored 3:1 (and 8:1 in colder stabs). The water content of post-perovskite thus strongly depends on how much water could be present in bridgmanite, any water still present in bridgmanite at the bottom of the lower mantle would partition into post-perovskite based on these results. The effect of Al and Fe on the elasticity of post-perovskite has also been studied using first-principles, concluding that these elements would have an even greater effect on its elasticity when compared to bridgmanite (Tsuchiya and Tsuchiya, 2006).

1.5 Dense Hydrous Mantle Silicates

Instead of NAMs, it is possible that water in the mantle would be present in so-called 'Dense Hydrous Magnesium Silicates' (DHMSs). These would be minor phases somewhere in the MgO – H_2O – SiO_2 system, that take up a high quantity of hydrogen into their structure. Hydrogen would get incorporated into these phases through dehydration of other phases in the upper mantle like serpentine for example (Irifune et al., 1998).

Many phases with slightly different stoichiometry of these three components exist, and the pressures and temperatures at which they can exist vary. Ringwood and Major (1967) were the first to describe the existence of three such phases, which were named Phase A ($Mg_7Si_2O_8(OH)_6$), Phase B ($Mg_{12}Si_4O_{19}(OH)_2$) & Phase C ($Mg_{10}OSi_3O_{14}(OH)_4$). Phase A contains ∼12 wt% H_2O and is stable between 3 and 18 GPa. Phase B contains ∼2.4 wt% H_2O and is stable between 11 and 17 GPa and up to ∼1200°C. Phase A & B would thus not be stable in the lower mantle.

Pacalo and Parise (2000) described the existence of another phase, which they called Superhydrous Phase B, and was later found to be equivalent to the aforementioned Phase C (Kanzaki, 1993). The name superhydrous phase B nevertheless persisted over Phase C from that point on. This phase is stable between 14 and 30 GPa and up to 1400°C (Ohtani et al., 2000, 2003) and contains ∼6 wt% H_2O (Kakizawa et al., 2018). Pressure-wise it would be stable down to the shallowest part of the lower mantle, but 1400°C is well below the mantle geotherm, making colder subduction slabs the only viable option for its existence. A recent study by Li et al. (2022) has found that the incorporation of 11.7 wt% Al_2O_3 expands the stability field of superhydrous phase B by 400–800°C, which could make it stable at mantle geotherm temperatures. This study suggests that Al prefers to partition into superhydrous phase B, compared to bridgmanite.

Phase D ($MgSi_2O_4(OH)_2$) was discovered by Liu (1987). This phase is thought to be stable up to ∼50 GPa and 1300°C (Frost and Fei, 1998; Shieh et al., 1998), well into

the lower mantle but at temperatures below the geotherm, again restricting it to colder subduction slabs. Kanzaki (1991) reported the existence of two more DHMS phases, which were named Phase E ($Mg_{2.08}Si_{1.16}O_{2.08}(OH)_{3.2}$) & Phase F. Phase F was later found to be identical to Phase D (Ohtani et al., 1998). Ohtani et al. (1997), Kudoh et al. (1997) and Hexiong Yang et al. (1997) all describe the same Phase G, which was later found to also be equivalent to Phase D. Ghosh and Schmidt (2014) established that the stability of Phase D is extended by 200°C by adding 1 wt% Al_2O_3, but that the addition of FeO would have the opposite effect. It is still somewhat unclear whether the presence of Al would increase its water solubility (Xu and Inoue, 2019) or decrease it (Nakatsuka et al., 2022). It has also been suggested that Phase D could form from superhydrous phase B (Li et al., 2022), and that the dehydration of Phase D might be responsible for the presence of free water at the very top of the lower mantle (Xu and Inoue, 2019).

Phase Egg ($Al_5Si_5O_{17}(OH)$) is technically not a DHMS because it does not contain any Mg, but is worth a mention since it contains 7.5 wt% H_2O (Fukuyama et al., 2017) and is stable up to 17 GPa and ∼1500°C (Fukuyama et al., 2017; Sano et al., 2004). This phase has also been found as inclusions in a diamond from Brazil (Wirth et al., 2007).

The last noteworthy DHMS phase is called Phase H ($MgSiO_2(OH)_2$) (Bindi et al., 2014; Nishi et al., 2014; Tsuchiya, 2013), which forms a solid solution with a phase called δ-AlOOH (A. Suzuki, E. Ohtani, 2000; Sano et al., 2008; Sano-Furukawa et al., 2009). This solid solution is remarkable because it represents the only phases that could clearly be stable at high enough temperatures to be present outside of subduction slabs, with its stability field extending from 33 to 134 GPa, and up to ∼2000°C (Sano et al., 2008), thus spanning the entire lower mantle. This has caused it to get much attention and studies looking at its physical properties in more detail have thus been conducted.

Tsuchiya and Tsuchiya (2009) initially performed ab-initio calculations to determine what the shear and pressure wave velocities of δ-AlOOH would be at lower mantle

conditions. Resulting sound wave velocities were similar to Mg-bridgmanite, which would make this phase difficult to detect with seismology (Ohtani, 2015). Mashino et al. (2016) carefully performed experiments up to 40 GPa at room temperature, finding body wave velocities lower than the ones reported by Tsuchiya and Tsuchiya (2009). They determined that the V_S of polycrystalline δ-AlOOH is 20–30% higher than transition zone minerals, and ∼7% lower than Mg-bridgmanite, which would be reflected in seismic data by means of positive V_S anomalies in the transition zone and negative anomalies in the lower mantle. These lower velocities have therefore been proposed as a possible explanation for the Ultra-Low Velocity Zones at the bottom of the lower mantle (Duan et al., 2018; Ohtani, 2020). Wang et al. (2022) did the same type of measurements for δ-AlOOH on a single crystal and determined a V_S 8.8% higher and V_P 5.2% higher compared to the results from Mashino et al. (2016), but still lower than bridgmanite. A few studies have investigated the effect of Fe on the elasticity of δ-AlOOH, which seem to show a trend of decreasing body wave velocities as more Fe gets added (Ohira et al., 2021; Satta et al., 2021; Su et al., 2023, 2021). Conductivity measurements on δ-AlOOH have suggested that it could be responsible for high-conductivity regions in subduction slabs (Su et al., 2023).

The creation of δ-AlOOH has been suggested to be possible from the decomposition of Phase D into δ-AlOOH and stishovite (Sano et al., 2004). A study by Ohira et al. (2014) suggested that Al-bearing bridgmanite and water could react with each other at lower mantle depths the create $MgSiO_2(OH)_2$ – δ-AlOOH. The water could come from other previously discussed DHMS phases which dehydrate at similar conditions, or it could have survived in between mineral grains in subduction slabs all the way down to the shallow lower mantle (Ono et al., 2002). Song et al. (2022) however, suggested based on density functional theory calculations, that Phase H would dehydrate into bridgmanite between ∼1300–1700 km depth in the lower mantle and thereby cause a positive velocity jump at those depths.

To conclude, the presence of the DHMS phases in the lower mantle is unlikely anywhere other than in subduction slabs, due to their inability to remain stable at higher

temperatures. The only exception is the Phase H – δ-AlOOH solid solution, although it is also more likely to exist close to subduction zones, where Al and H are more abundant. Further potential geophysical implications are discussed in Section 1.6.

1.6 Low velocity zones in the shallow lower mantle

The manuscripts in Chapters 2 & 3 carry potential geophysical implications about low-velocity zones in the shallow lower mantle. This section will introduce previous works on low velocity zones relevant to this thesis.

The presence of low-velocity zones below the 660 km discontinuity is well-established based on geophysical measurements of seismic velocities and attenuation at those depths (Deuss et al., 2013; Fukao and Obayashi, 2013; Kaneshima and Helffrich, 1998; Lawrence and Wysession, 2006; Liu et al., 2016, 2018; Niu and Kawakatsu, 1996; Niu et al., 2003; Omori et al., 2004; Schmandt et al., 2012; Simmons and Gurrola, 2000; Tauzin et al., 2013). So far, physical explanations for these lower seismic velocities have mostly involved the presence of melts. As shown in Section 1.4, the transition zone minerals wadsleyite and ringwoodite have the highest water solubilities when compared to the other NAMs in the mantle. This has led to the belief that the transition zone would be much wetter than the upper and lower mantle surrounding it. This idea has been supported by geophysical observations of high-attenuation anomalies close to subduction slabs at transition zone depths (Zhu et al., 2013), viscosity profiles (Fei et al., 2017), measurements of high electrical conductivit (Karato, 2011; Kelbert et al., 2009), body wave velocity anomalies (Li et al., 2013; Suetsugu et al., 2006; Wang et al., 2019), and geomagnetic diurnal observations (Zhang et al., 2022a). A recent finding of hydrous peridotite inclusions in diamonds from Botswana—containing ringwoodite, ferropericlase, enstatite (likely as a polymorphic inversion from bridgmanite), a hydrated DHMS phase, and probably coming from a depth of ∼660 km—also suggests that this region would be at least locally hydrated (Gu et al., 2022).

The seemingly large differences between possible water contents of the upper mantle,

transition zone, and lower mantle have led to the question of what happens to all the water in the transition zone, and what happens to this water at the boundaries between these different parts of the mantle. This is where the potential presence of melts in those regions arises. Melts have been proposed to be responsible for the reduction in seismic velocities in those regions (Sakamaki et al., 2006; Schmandt et al., 2014), and the possible alignment of melt inclusions could be responsible for observations of seismic anisotropy (Wookey et al., 2002). Two possibilities have been put forward to explain the presence of melts at this depth.

- Water is known to lower the liquidus temperature of minerals, and the argument has been made that if enough water is present around the boundaries of the transition zone, the liquidi of mantle phases might drop below the geotherm, which would cause partial melting (Hirth and Kohlstedt, 1996; Kawamoto, 2004; Ohtani, 2021). According to Karato et al. (2020) and Ohtani (2021), low-velocity regions observed at the top of the lower mantle could possibly be explained by this phenomenon. Whether these phases will start melting also depends on water solubility of lower mantle minerals, which as explained in Section 1.4 above remains quite unconstrained. To investigate this idea, Schmandt et al. (2014) performed laser-heated diamond anvil cell experiments on hydrous ringwoodite, in order to attempt to transform it into hydrous bridgmanite. Based on TEM analyses of the recovered sample, they concluded that ringwoodite dehydrates across the transition, forming intergranular partial melts.
- The second possibility is that melts get created around 660 km due to the dehydration of DHMS. Many of these phases are not stable beyond those depths (Sec. 1.5) and could thus decompose and create melts (Ohtani, 2015; Schmandt et al., 2014).

If melt were to exist at 660 km depth, whether it be through the dehydration of DHMS, the breakdown of hydrous ringwoodite, or partial melting of the mantle under wet conditions in the shallow lower mantle, it would have to coexist and be in chemical equilibrium with bridgmanite. As mentioned in Section 1.4, melting experiments at

high pressure and temperature have looked at the partitioning of Fe, Mg & Si between melt and bridgmanite under wet conditions. The results indicated that the melt would be depleted in the Fe & Si, and enriched in Mg compared to dry conditions (Amulele et al., 2021; Kawamoto, 2004; Nakajima et al., 2019). The absence of Fe and higher concentration of H would make this melt less dense compared a melt created in anhydrous conditions, making it more likely to remain buoyant at the top of the shallow mantle (Karki et al., 2021; Nakajima et al., 2019). An alternative hypothesis has been proposed, arguing that the melting of the mantle would be delayed to a depth ∼750 km where transition of water-bearing garnet to bridgmanite would induce partial melting (Karato et al., 2020; Panero et al., 2020) and explain seismic scatterers in that depth range (Jenkins et al., 2017; Kind et al., 2002; Maguire et al., 2018; Waszek et al., 2018).

Some push-back exists on the presence of melts in the shallow lower mantle being responsible for the observed negative velocity anomalies. This is based on the estimation that a large amount (a few vol.%) of it would be needed to actually provoke a detectable difference in the seismic signals (Takei, 2002), with a thickness comparable to the wavelength of the waves themselves (Karato et al., 2020). Moreover, for the reduction of seismic velocities to be efficient, melt has to be present over a large area, i.e., completely wetting (i.e. surrounding) all grain boundaries (Stocker and Gordon, 1975), which seems unlikely based on experimental data (Karato et al., 2020; Panero et al., 2014). The possibility of having hydrous melts right above and below the mantle transition zone has also been investigated in ab initio molecular dynamics simulations and was found to be unlikely due to buoyancy issues (Drewitt et al., 2022). This opens the potential to other explanations for the low-velocity zones in the shallow mantle. Chapter 2 will explore the possibility for hydrous Al-bearing bridgmanite to reduce seismic velocities at shallow lower mantle depths depending on its water content. Chapter 3 will show that the phase transition from stishovite to $CaCl_2$-type SiO_2 could take place at lower pressures than previously thought, especially when the effect of Al and H is considered. Low-velocities zones at depths of 800–1200 km could be explained by this phenomenon.

Chapter 2

Investigating the Effect of Water on the Elasticity of Bridgmanite

This chapter represents most of the work performed during the course of this doctorate. For the first ∼2.5 years, a pure $MgSiO_3$ bridgmanite sample, containing ∼2000 ppm H_2O, was measured. Initially, this sample was loaded into a Diamond Anvil Cell together with a dry sample with equivalent composition, to make direct comparison of sound velocities more robust. On a technical level, measuring this sample proved to be quite challenging, and this setup cannot be recommended for future studies. Acquired velocities were very different from what is expected for bridgmanite which led to confusion as to what exactly was being measured, considering that a KCl pressure medium was below and above both samples. After loading the hydrous sample by itself again and performing extra measurements on KCl, it became clear that the supposed 'bridgmanite' peaks were actually caused by KCl. Only when hydrous bridgmanite was measured without any pressure medium, a bridgmanite signal from this sample was detected. This result was not significantly different from dry $MgSiO_3$. This observation, combined with SEM findings of larger grains in the sample with a very different Mg/Si ratio and the high broadness of the peak measured with FTIR, led to the conclusion that water was most likely not structurally present in this sample. Measurements were therefore halted in September 2022.

Measurements were resumed on a Al-bearing hydrous bridgmanite sample in October 2022, the results of which are presented in this Chapter. Initially the interpretation of the Brillouin spectra from this sample was not straightforward, because multiple peaks were sometimes found as shown later in this Chapter. However, thanks to the previous measurements on KCl and literature data on superhydrous phase B, the bridgmanite peaks could be identified and fitted. At first, the goal of this study was to only characterize pressures corresponding to the shallow lower mantle regime, which is why more data points are present in between 25 and 45 GPa and why large 300 µm culets were used. When it became clear that the main effect of water is actually on the steepness of the velocity trend, the decision was made to measure two more points at higher pressures, to better constrain the finite strain fitting of the data. The last measurement at 85 GPa was finished on 08.12.2023. The DAC is still intact, and more measurements at higher pressures could be attempted, although the diamonds are expected to break at any moment due to their high culet size.

Investigating the Effect of Water on the Elasticity of Bridgmanite

Thomas de Selva-Dewint[1*], Motohiko Murakami[1], Takashi Yoshino[2]
Amir Khan[1], Luiz Morales[1], Federico D. Munch[3] Youyue Zhang[2],
Sho Kakizawa[4]

[1]Institute of Geochemistry and Petrology, ETH Zürich, Clausiusstrasse 25,
8092 Zurich, Switzerland

[2]Institute for Study of the Earth's Interior, Okayama University, Misasa,
Tottori-ken 682-0193, Japan

[3]Institute of Geophysics, ETH Zürich, Sonneggstrasse 5
8092 Zurich, Switzerland

[4]Japan Synchrotron Radiation Research Institute, 1-1-1,
Kouto, Sayo-cho, Sayo-gun, Hyogo 679-5198, Japan

The Earth's transition zone is thought to be a major water reservoir in the Earth's interior. Whether the lower mantle would also be able to incorporate a significant amount of water is thus an important question to address. Varying accounts concerning the water solubility of lower mantle phases and the general paucity of experimental data addressing this issue motivated this work, in which the presence of water in the main lower mantle phase, bridgmanite, was investigated. For this, the effect of water on the mineral's elasticity is determined. An Al-bearing polycristalline bridgmanite sample was measured, containing ∼1054 ppm H_2O. The sample's water content was examined using Fourier Transform Infrared spectroscopy (FTIR) and Atom Probe Tomography (APT). The elasticity of the sample was studied using Brillouin scattering

spectroscopy between 25 and 85 GPa. Compared to the Mg-bridgmanite endmember, a drop of ∼6% in the shear modulus, and an increase of 5% in the first derivative of the shear modulus is observed. The shear wave velocities of hydrous bridgmanite are lower compared to the dry endmember a lower pressures, but a cross-over happens around 55 GPa, after which hydrous bridgmanite becomes faster compared to its dry counterpart. These results have important geophysical implications. Firstly, by modeling the effect of water on a lower mantle bridgmanite–ferropericlase assemblage, and comparing it to PREM, no significant amount of water is expected to be present in the lower mantle. Secondly, the reduction of shear wave velocities in bridgmanite due to the presence of water could help explain low-velocity anomalies observed around subduction zones at those depths.

1 Introduction

Bridgmanite makes up 80–90% of the lower mantle (Hirose, 2006), and is therefore the most important mineral to research when trying to understand what the effect of minor elements are on the lower mantle. Bridgmanite has an orthorhombic crystal lattice and was classified as part of the *Pnma* space group when it was found naturally in a shocked meteorite (Tschauner et al., 2014). It is also sometimes described using the *Pbnm* space group, but both descriptions are equivalent. Experimentally, the phase was first observed in a laser-heated Diamond Anvil Cell (DAC) by Liu (1974) at 27 GPa and about 1400–1800 °C, where it transformed from garnet. Horiuchi et al. (1987) described the orthorhombic structure as a deviation from the cubic idealized form due to rotation and tilting of the cation octahedra. Distortions relative to the idealized structure increase with pressure (Fiquet et al., 2000) and increasing Al content (Walter et al., 2004;

Kojitani et al., 2007). The addition of Fe^{2+} on the other hand, lowers the distortion of the structure (Kudoh et al., 1990). Bridgmanite has so far never been found in natural diamond inclusions, as it seems to consistently transform to retrograde enstatite. The occurrence in coexistence with ferropericlase and the abnormally high Al concentrations in such enstatites are evidence that they were originally bridgmanite (Kaminsky, 2018). This retrograde phase has been observed in numerous diamond inclusions in placer deposits and kimberlites from Brazil (e.g. Wilding et al. (1991); Zedgenizov et al. (2015)), Guinea (e.g. Stachel et al. (2000)), Australia (e.g. Tappert et al. (2009)) and Canada (e.g. Scott Smith et al. (1984); Davies et al. (2004)).

Much like the olivine polymorphs, bridgmanite is a solid solution between the $MgSiO_3$ and $FeSiO_3$ endmember. The Mg# of retrograde enstatite diamond inclusions usually lies between 0.84 and 0.96, which corresponds to the range that is thought to be realistic for the lower mantle (Kaminsky, 2018). Inclusions commonly contain 1–3 wt% Al, with some samples even reaching around 10 wt% (Kaminsky, 2018). Realistic lower mantle bridgmanites are expected to contain 4–5 wt% Al_2O_3 Huang et al. (2021). The reason that bridgmanite contains so much Al can be traced back to the transition from garnet to bridgmanite around 750 km, which is the main Al sink at shallower depths (Wood, 2000). Experiments show that the Al concentration in bridgmanite tends to increase with pressure (Irifune et al., 1996; Wood, 2000; Liu et al., 2016). Liu et al. (2016) found that the Al_2O_3 content in bridgmanite doubles from 27 to 52 GPa. Also, Fe concentrations seem to positively correlate with the amount of Al present (Kaminsky, 2018).

Both the presence of Fe and Al have been described to have an important influence on the physical properties of bridgmanite. Their presence has an effect on phase equilibria (Wood and Rubie, 1996; Frost and Langenhorst, 2002; Nakajima et al., 2012), electrical conductivity (Xu et al., 1998), and rheology (Holzapfel et al., 2005). Their effect on the

compressibility and equation of state of bridgmanite has also been intensively investigated (Ono et al., 2004; Walter et al., 2004, 2006; Vanpeteghem et al., 2006; Andrault et al., 2007; Lundin et al., 2008; Nishio-Hamane et al., 2008; Saikia et al., 2009; Tange et al., 2009; Ballaran et al., 2010; Catalli et al., 2010, 2011; Ballaran et al., 2012; Glazyrin et al., 2014; Mao et al., 2017; Mashino et al., 2020; Fu et al., 2023). Experiments looking at the lattice occupation of Fe and Al in bridgmanite were performed in the work by Vanpeteghem et al. (2006), which shows that Fe^{2+} prefers to exclusively be on the octahedral Mg^{2+} site, and the Al^{3+} on the Si^{4+} site. Two main mechanisms have been proposed to explain the substitution of Al into the bridgmanite lattice. The first explains the presence of Al^{3+} through a charge-coupled substitution with both Si^{4+} and Mg^{2+}, entering both sites and thus balancing the overall charge imbalance (Shannon and Prewitt, 1969). The second involves the replacement of only Si^{4+} by Al^{3+}, with the creation of oxygen vacancies to balance the charge. There is evidence that both the first (Andrault et al., 1998; Stebbins and Kroeker, 2001) and second mechanism (Brodholt, 2000; Daniel et al., 2004) can take place.

1.1 Hydrogen solubility in bridgmanite

Varying reports on water solubility in the crystal lattice of bridgmanite from multi-anvil studies have made it difficult to determine whether this mineral could be an important H carrier in the lower mantle. An early study by Meade et al. (1994) suggested quite significant H contents in $MgSiO_3$ bridgmanite ($\sim$700 H atoms per 10^6 Si atoms), similar what would be expected for olivine or stishovite for example. They observed two clear H stretching bands by FTIR at 3483 and 3423 cm^{-1}. Bolfan-Casanova et al. (2000) however did not find any significant amount of water in $MgSiO_3$ bridgmanite. This might be due to the much shorter heating times in this study during synthesis, not allowing for enough

time to anneal the sample and create cation vacancies in the crystal lattice, which would be needed for the incorporation of water (Libowitzky and Beran, 2006). A study soon after by Higo et al. (2001) reported ∼500 ppm of H_2O in $MgSiO_3$ bridgmanite based on Secondary Ion Mass Spectrometry (SIMS) analyses.

As previously discussed, realistic lower mantle bridgmanite would contain a few wt% Al, which is relevant for the solubility of H in bridgmanite. The presence of Al has been suggested to increase the capacity for bridgmanite to take up water in its lattice, through oxygen defect substitution (Navrotsky, 1999). The oxygen vacancy created through one of the previously discussed substitution mechanisms for the incorporation of Al in bridgmanite, could be filled by an H^+ ion. Moreover, having Fe present in bridgmanite has also been shown to influence how much water could be incorporated (Jiang and Zhang, 2019), because the presence of Fe^{3+} in the A or B sites could easily be charge balanced with H^+. Therefore, it makes a lot of sense to study bridgmanite containing Al and Fe when trying to understand its water solubility.

Indeed, more studies exist that consider the solubility of water in an Al-ro Fe-bearing bridgmanite sample. Murakami et al. (2002) were the first to report a water content of ∼2000 ppm H_2O in a few bridgmanite samples containing realistic amounts of Al and Fe, based on the observation of a broad band around 3400 cm^{-1} in the FTIR spectra. When measuring a pure $MgSiO_3$ sample, Murakami et al. (2002) could only find <60 ppm H_2O, stressing the importance of Fe and Al being present. Litasov and Ohtani (2003) followed suit, performing 8 experiments with varying amounts of Al and Fe and reporting water contents in the examined bridgmanites between 47 and 1780 ppm based on FTIR bands around 3400 cm^{-1}. Another study shortly after by Bolfan-Casanova et al. (2003), also on Al- and Fe-bearing bridgmanite, observed FTIR bands around 3400 cm^{-1}, but attributed them to the presence of superhydrous phase B detected with Raman spec-

troscopy, therefore concluding that no considerable amount of water could be incorporated into bridgmanite, even if Al and Fe are present. Panero et al. (2003) came to a similar conclusion when doing experiments with coexisting stishovite and bridgmanite, reporting that most of the water partitions into stishovite, and only <50 ppm H_2O remains in Fe-Al-bridgmanite. Stishovite is however not expected to be present in any significant amount in the lower mantle, except in subduction slabs. Inoue et al. (2010) was able to measure water contents of 300, 600 and 700 ppm in Al-Fe-bearing bridgmanite coexisting with ringwoodite, based on SIMS analyses. While investigating the solubility of F in bridgmanite, Yoshino and Jaseem (2018) observed a concentration of ∼2000 ppm H_2O in Mg-bridgmanite, and reports even higher concentrations going up to ∼6000 ppm H_2O in Al-bearing bridgmanite when adding F to the starting composition. Bridgmanite is thought to be the Earth's main host of F, and its ability to form a complex with H would facilitate their coupled substitution into Si vacancies. Fu et al. (2019a) confirmed the presence of water in Al-Fe-bridgmanite again, reporting a water content of ∼ 1000 ppm based on FTIR and SIMS. FTIR spectra showed no OH-stretching bands at ∼3230 and ∼3460 cm^{-1}. TEM analyses was also performed on the samples, confirming that the H is indeed in the bridgmanite and not in hydrous inclusions. Amulele et al. (2021) performed high pressure and temperature melting experiments on bridgmanite to investigate the partitioning of elements between bridgmanite and coexisting melt under wet conditions, and reported a maximum water solubility of ∼1000–1500 ppm in bridgmanite based on FTIR measurements. They argue that the phase would be unquenchable though, with some of the water going into superhydrous phase B upon cooling. The two latest multi-anvil studies on the solubility of water in bridgmanite however, have again gone back to the idea that very little water would be present. Liu et al. (2021) suggested that the water concentration in Al-Fe-bridgmanite should not exceed ∼30 ppm, based on the absence

of significant OH-stretching bands in FTIR analyses of their samples. Ishii et al. (2022) reaches a similar conclusion, reportedly that the water content of their Al-bearing (but Fe-barren) bridgmanite sample would be below the detection limit of FTIR spectroscopy. This recent change in the balance towards experiments not observing any water in bridgmanite has added to the confusion regarding the ability of bridgmanite to incorporate water and refueled a debate on the question.

The mentioned works investigating the solubility of water in bridgmanite have all been based on multi-anvil experiments. There have been three studies however utilizing Laser Heated Diamond Anvil Cells (LHDAC) instead, in order to synthesize water-bearing bridgmanite in-situ. Schmandt et al. (2014) used hydrous ringwoodite as starting material to synthesize bridgmanite in the LHDAC, and measured OH-stretching bands at 3400 and 3680 cm^{-1} using synchrotron FTIR. However the presence of melt and brucite alongside bridgmanite in the sample chamber made it difficult to really assign to bands to bridgmanite. Panero et al. (2014) used enstatite as a starting material, and also observed several OH-stretching bands in the FTIR spectra, but concluded that most of the signal should be caused by melt present inbetween the bridgmanite grains, concluding that not more than 10 ppm of water is present in the sample. Recently, Yang et al. (2023) was able to solve this issue of having interstitial melts by melting silicate glass at 33 GPa and 3690 K and allowing bridgmanite to crystallizing from this melt, which remained completely separated from it. NanoSIMS analysis of this bridgmanite revealed that it contained ∼1100 ppm water, while being in equilibrium with the coexisting melt containing ∼4.4 wt% H_2O. This last study again provides evidence that bridgmanite crystallized at lower mantle conditions is physically capable of incorporating water.

The presence of Fe and Al are likely to increase the capacity for H to be structurally bound in the mineral lattice, but increasing temperature is thought to make its incorpo-

ration more difficult (Bolfan-Casanova, 2005). Increasing pressure however counteracts this effect as experimental evidence shows that the solubility of water increases with increasing pressures (Karato, 2008). Both these trends are confirmed by experiments on ceramic perovskites as analogues for bridgmanite (Navrotsky, 1999).

1.2 The elasticity of bridgmanite

The influence of water on the elasticity of bridgmanite is a topic that has not been studied experimentally before, and is therefore the topic of this work. Only ab-initio calculations by Jiang and Zhang (2019) exist, that predict a lowering of the shear and bulk moduli of bridgmanite and an increase of their first derivatives upon incorporation of water. A summary of the elasticity studies performed on dry bridgmanite is given hereafter to provide context for this work.

The earliest studies investigating the elasticity of bridgmanite were restricted to ambient pressures (Yeganeh-Haeri, 1994; Sinogeikin et al., 2004) or low pressures not relevant for the lower mantle (Sinelnikov et al., 1998; Li and Zhang, 2005). Brillouin scattering experiments measuring the shear wave velocity of the sample at multiple pressure points on pure $MgSiO_3$ were first performed by Murakami et al. (2007) on a polycrystalline sample. These results were close to previous computational ab-initio results from Wentzcovitch et al. (2004). A later study by Chantel et al. (2012) used ultrasonic measurements instead of Brillouin spectroscopy to investigate the acoustic velocities of polycrystalline $MgSiO_3$. This method allows for the measurement of both shear (V_S) and pressure (V_P) wave velocities. The shear wave velocities seem to be about 5% higher compared to previous results from Murakami et al. (2007), but it is difficult to directly compare the results as the measured pressure range does not overlap. The results from Chantel et al. (2012) are in good agreement with a different ab initio study by Oganov et al. (2001). The latest

Brillouin scattering study on pure $MgSiO_3$ was performed by Criniti et al. (2021), on a single crystal sample. Their bulk velocity trend for shear and pressure wave velocity is comparable to the results from Chantel et al. (2012).

The effect of Al and Fe on the elasticity of bridgmanite was studied by Li et al. (2005) using Density Functional Theory calculations. They predict a decrease in sound velocity due to the addition of Fe in the bridgmanite crystal lattice, with it having a stronger effect on shear modulus than the bulk modulus. The difference between the effect of Al alone, and the combined effect of Al and Fe was calculated to decrease with increasing pressure. The addition of these elements on sound velocities would therefore have a similar effect as increasing temperature, but an opposite effect on density, as density decreases at high temperatures and increases with higher Fe contents (Li et al., 2005). The spin character of Fe was expected to have a negligible effect on the elasticity of bridgmanite in this study. The first experimental work looking at Al-bearing bridgmanite at higher pressures using Brillouin scattering, was performed by Jackson et al. (2005). They used a polycristalline sample containing 5.1±0.2 wt% Al_2O_3. When investigating a polycrystalline $MgSiO_3$+4 wt% Al_2O_3 sample, Murakami et al. (2012) observed slightly lower shear wave velocities compared to the pure endmember previously measured in Murakami et al. (2007), thereby also making the shear modulus G_0 somewhat reduced. The difference between the Al-barren and bearing samples becomes clearer at lower pressures through a distinctive trend of the slope, expressed in an increase of the first derivative of the shear modulus G_0'. The shear wave velocities in Jackson et al. (2005) seem a bit higher than those from Murakami et al. (2012), even though a clear comparison is difficult as their pressure ranges barely overlap. The data only overlaps at ∼45 GPa, where the shear wave velocity of Murakami et al. (2012) is ∼2% lower than that from Jackson et al. (2005).

The first study comparing the elasticity of $MgSiO_3$ bridgmanite to Fe-bearing bridgmanite, was done by Chantel et al. (2012) on a $Mg_{0.95}Fe^{2+}_{0.04}Fe^{3+}_{0.01}SiO_3$ polycrystalline sample. They concluded that the presence of iron has no significant influence on the shear wave velocities, but causes a decrease in the pressure wave velocities. Then, based on ab-initio calculations, Shukla et al. (2016) argued that the coupled substitution of Al and Fe into bridgmanite would not have a significant effect on either V_S or V_P. Kurnosov et al. (2017) was the next to experimentally investigate the effect of Fe, combined with Al, this time using a single crystal $(Mg_{0.9}Fe_{0.1})(Si_{0.9}Al_{0.1})O_3$ bridgmanite sample. They did observe a clear drop in velocities for both the shear and pressure waves due to the presence of Fe & Al. In both cases, the velocities were lower than those observed by Chantel et al. (2012), but the presence of both Al and Fe in this study makes it hard to discriminate what exactly the effect of Fe or Al would be by itself. Next, Fu et al. (2018) investigated the elasticity of polycrystalline $Mg_{0.96}Fe^{2+}_{0.036}Fe^{3+}_{0.014}Si_{0.99}O_3$ using a combination of Brillouin scattering and impulsive simulated light scattering. They observe a clear softening in pressure wave velocities at $\sim$50 GPa in this sample, corresponding to the Fe spin transition. The exact onset pressure of the spin transition is still under debate and is most likely strongly dependent on the exact composition of bridgmanite (Okuda et al., 2020). The shear wave velocity data however did not show this softening. The V_P data seems to be closest to the measurements from Kurnosov et al. (2017), while the V_S data lies in between the measurements by Chantel et al. (2012) and Kurnosov et al. (2017). The measurements extend to $\sim$70 GPa, and the trend is clearly steeper compared to the data from Murakami et al. (2007) and Murakami et al. (2012) at similar pressures. Fu et al. (2019b) confirmed this decrease of both V_S and V_P when using a single crystal instead of polycrystalline bridgmanite sample that also contained small amounts of Al. Only two pressures were investigated though, making a velocity trend

comparison with other studies difficult. By measuring two bridgmanite samples with the different amounts of iron, corresponding to the compositions $(Mg_{0.93}Fe^{2+}_{0.07})(Fe^{3+}_{0.02}Si_{0.98})O_3$ and $(Mg_{0.86}Fe^{2+}_{0.15})(Fe^{3+}_{0.03}Si_{0.97})O_3$, Mashino et al. (2020) was a able to observe a linear reduction in shear wave velocities with increasing Fe content. Only shear wave velocities were measured in this study, making it impossible to confirm the softening in V_P data observed by Fu et al. (2018). A recent study by Fu et al. (2023) investigated single crystal $Mg_{0.88}Fe_{0.1}Al_{0.14}Si_{0.90}O_3$ using the combination of Brillouin scattering and impulsive light simulated light scattering. They observed a decreases of ∼3% in V_S and ∼4% in V_P relative to the Mg endmember data from Criniti et al. (2021). The softening in pressure wave velocities due to the spin transition that was previously observed in Fu et al. (2018) was however not reproduced in this study, which was attributed to the presence of Al which preferentially goes into the Si site, forcing Fe into the Mg site. Irrespective of the slight discrepancies between the experimental datasets, it has become clear that the presence of Al and Fe in bridgmanite influences its elasticity due to a consistent observation of a lowering in the body wave velocities.

Methods

1.3 Sample preparation

The sample (1K3385) used in this study was prepared using a multianvil pressure with a 10/4 cell assembly and a Au70Pd30 capsule at conditions specified in Table 1. This sample was broken up into pieces of adequate size to load in a DAC. The Diamond Anvil Cell was prepared using 2 diamonds with 300 µm-sized culets and a Re gasket. The Re gasket was precompressed to a thickness of 70 µm, and a sample chamber hole with an initial diameter of 150 µm was drilled in its center with a 8–15 ps pulsed green laser (532 nm) to create the sample chamber. Two thin compressed layers of fine-grained KCl pressure medium were added below and above the bridgmanite sample in the sample chamber. A ruby was placed in the sample chamber to allow for pressure measurements (explained in Sec. 1.7), slightly off-centered to avoid any interference with Brillouin measurements. Figure 1 shows the sample after it was loaded into the DAC.

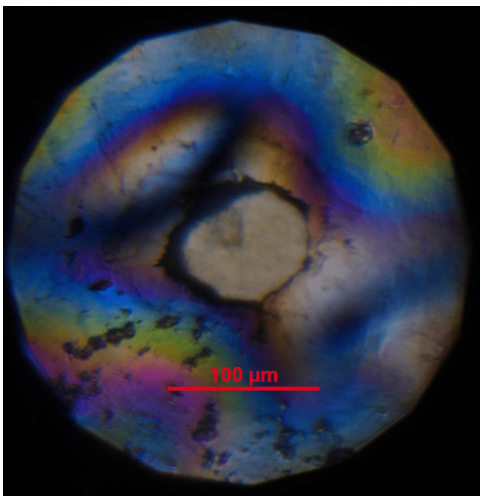

Figure 1: Reflected light image of the sample chamber after loading of the hydrous bridgmanite sample into the Diamond Anvil Cell.

The major element composition of the sample measured by Field emission Scanning Electron Microscopy (FESEM) is reported in Table 1. Based on the SEM imaging shown in Fig. 2, the grain size of the sample was determined to vary between ∼1–10 µm. To examine the distribution of the elements throughout the sample, major element maps were obtained by Energy Dispersive Spectroscopy (EDX) on the FESEM (Mg and Si shown in Fig. 3). Small spots with different Mg/Si ratio are detected in between grains, pointing to the possibility of a minor other phase present there. This phase is likely to be superhydrous phase B based on other observations highlighted in Sec. 1.5 and 1.8. We can conclude however that there are no major phases present other than bridgmanite.

Table 1: Multi-anvil synthesis conditions, and FESEM compositional results for hydrous bridgmanite sample 1K3385.

Synthesis conditions	
Pressure (GPa)	27
Temperature (°C)	1600
Run Time (min)	20
Major element composition	
MgO (wt%)	47.83
Al_2O_3 (wt%)	3.44
SiO_2 (wt%)	48.73

1.4 Fourier Transform Infrared Spectroscopy

The water content of the starting material was determined using Fourier Transform Infrared Spectroscopy (FTIR) measurements on a Bruker Tensor II spectrometer at the University of Bern. Unpolarized Transmission measurements through a 244 µm thick, double-polished slice of starting material were performed on ten random spots. Every spot had a size of 50 µm and consisted of 64 scans, with a spectral resolution of 4 cm^{-1}. The beam of polychromatic infrared (IR) radiation that is directed to travel through the prepared sample will generate excitations in the material, which will vibrate at char-

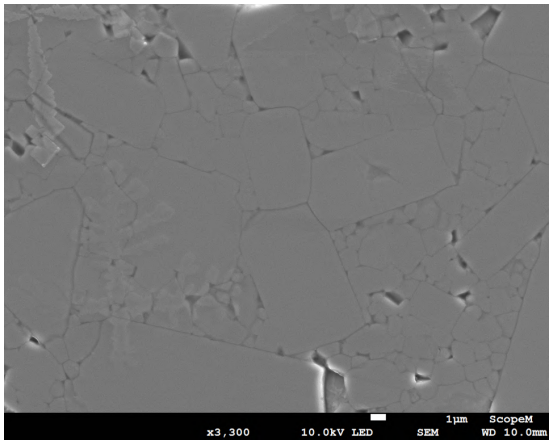

Figure 2: SEM image of 1K3385 showing the grain size distribution in the sample starting material. Larger grains with a diameter of ∼10 µm are distributed throughout the sample and surrounded by smaller µm-sized grains.

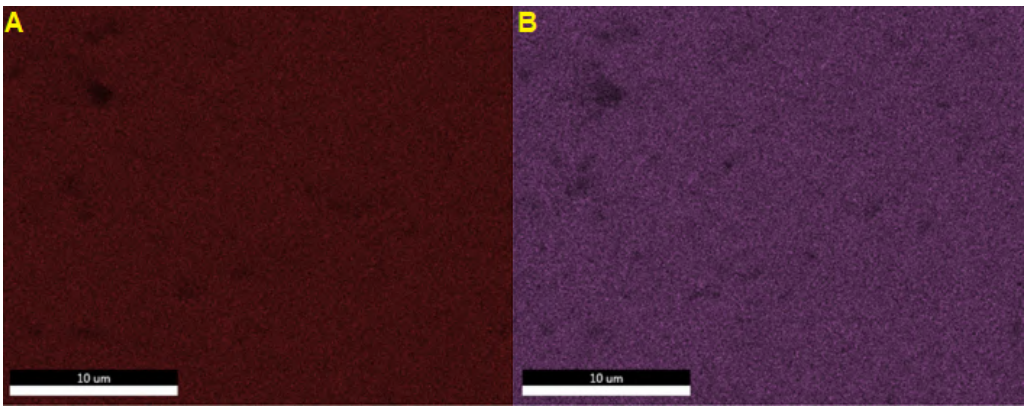

Figure 3: Energy dispersive X-ray maps taken in FESEM with the distribution of Mg (A) and Si (B) in the starting material. Small areas that appear darker or lighter relative to the surrounding material indicate a different Si/Mg ratio.

acteristic frequencies depending on the bonds present in its lattice. Depending on the frequency of these vibrations, the energy of light going through the sample will get absorbed at certain wavelengths, which can be detected by the IR detector. The detected interferogram is then Fourier-transformed into the IR spectrum (Libowitzky and Beran,

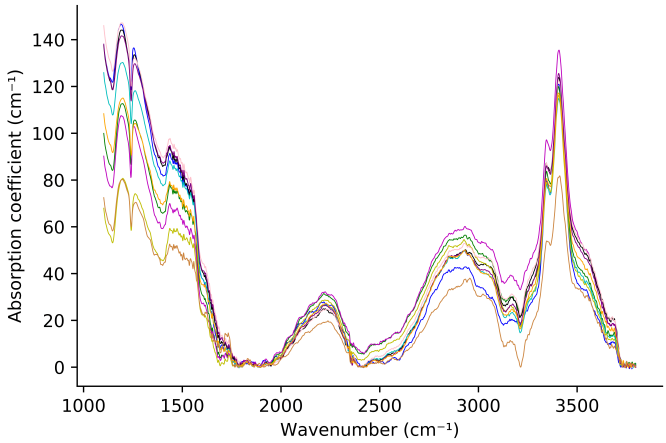

Figure 4: Measured FTIR spectrum of 1000–3600 cm^{-1}. The peaks below 1500 cm^{-1} result from absorption by the metal-oxygen bonds in bridgmanite. The absorption in the 3200–3600 cm^{-1} region is caused by structurally bound OH^--groups. The broad peaks between 1500 and 3200 cm^{-1} could be caused by more strongly bonded OH^--groups or structural defects.

2006).

All baseline corrected spectra over a wavelength range of 1000 to 4000 cm^{-1} are represented in Figure 4. OH^- stretching bands caused by the presence of structural water in silicate minerals are typically observed between 3000 and 3750 cm^{-1}, with their exact position depending on the length of the H bond in that particular crystal (Libowitzky and Beran, 2006). The region of interest identified to quantify the water content in this sample lies between ∼3200 and 3600 cm^{-1}. Two sharp peaks at 3347 and 3410 cm^{-1} can be observed in this region. To determine the water content, the adjusted Beer-Lambert law using the calibration represented in Eq. 1 was used (Paterson, 1982).

$$C_{OH} = \frac{D}{150\gamma} \int \frac{A(\nu)}{3780 - \nu} \mathrm{d}\nu, \tag{1}$$

with the water concentration C_{OH}, the density coefficient D,the absorption coefficient A, the extinction coefficient ϵ, and the orientation factor γ.

For every spectrum, an absorption coefficient at every wavelength is calculated by dividing the absorbance intensity by the thickness of the sample. Then, an integration of the absorption coefficient over the entire wavelength range of interest is performed (Eq. 1). The wavelength range of 3220–3600 cm^{-1} was selected for the calculations presented here. Based on a calculated sample density of 4.08 g/cm^3 and molar mass of 100.33 g/mol, a density factor D of 2244.26 ppm wt H_2O was calculated based on the relation $D = 10^6 \times (18/2\rho)$ (Bolfan-Casanova et al., 2000). The orientation factor was chosen to be $\gamma = 3$, which is valid under the assumption that the unpolarized measurements represent enough orientations to not be anisotropic (Kovács et al., 2008). An additional linear baseline correction in the wavelength range of interest was performed before integrating the area, to remain conservative with reported water content. Sambridge et al. (2008) determined that for unpolarized measurements, the total absorbance of a crystalline material can be calculated by taking the average of a representative set of randomly oriented crystals. The average of all acquired spectra shown in Figure 4 was therefore taken to calculate the final water concentration. Because these spectra are unlikely to represent a perfect Gaussian distribution, the error on the concentration is determined by calculating the median absolute deviation of all spectra. The resulting water concentration and error are 1054.34±45.25 ppm wt H_2O.

Based on other analytical methods described in Sections 1.5 and 1.8, the presence of a small amount of superhydrous phase B was confirmed. Both hydrous bridgmanite and superhydrous phase B are expected to show OH-stretching bands around 3400 cm^{-1}, and the calculated water content can therefore not be ascertained to be coming from one or the other based on the FTIR spectrum alone. Previous studies usually show sharper OH-bands for superhydrous phase B (e.g., Cynn et al., 1996), when compared to the bands found in bridgmanite around the same wavelength (Murakami et al., 2002;

Litasov and Ohtani, 2003; Schmandt et al., 2014). Bolfan-Casanova et al. (2003) for example reports very low water contents in bridgmanite despite finding OH-stretching bands around 3400 cm^{-1}, by arguing they are caused by superhydrous phase B that was confirmed to be present in their sample. The spectrum measured in this work shows comparatively sharp peaks, but it cannot be excluded that they are caused by bridgmanite since the sharpness of the peaks is rather a reflection of how strongly the H atom is bonded to oxygen in the crystal lattice (the bond length) and not necessarily typical for one mineral or another. Ca-perovskite ($CaSiO_3$) for example, which has a very similar structure to bridgmanite, commonly shows two sharp peaks at 3394 and 3326 cm^{-1} when hydrated (Libowitzky and Beran, 2006).

The broader bands between 2000 and 3200 cm^{-1} are interpreted to result from stronger H-O bonds (Libowitzky, 2016) than the ones previously discussed between 3200 and 3600 cm^{-1}. Bonds in this wavelength have also been previously described in enstatite (Mierdel and Keppler, 2004), wadsleyite (Jacobsen et al., 2005) and ringwoodite (Smyth et al., 2003). There is a chance however that these bands could be caused by structural disorder in the lattice (Libowitzky and Beran, 2006), and they were therefore not included in the water calculations.

FTIR spectra have been used in the past to get information about site occupancy in the measured mineral. In olivine and wadsleyite, the bands in OH-vibrational spectra have been reported to be caused by Mg^{2+} defects when around 3000–3300 cm^{-1} and caused by Si^{4+} vacancies when around 3500–3800 cm^{-1} (Matveev et al., 2001; Walker et al., 2006). Lemaire et al. (2004) also reports that OH bands in forsterite at 3612, 3580, 3566, 3555, and 3480 cm^{-1} can be assigned to Si vacancies, whereas bands at 3600, 3220 and 3160 cm^{-1} are only seen in samples with increased silica activity, meaning that they would be related to the Mg^{2+} sites. Based on this information, it is difficult to make a

conclusion about what type of vacancy the H in bridgmanite would be related to. The 3400 cm^{-1} wavelength falls right between previous limits of Mg^{2+} or Si^{4+} vacancy ranges discussed above, and a more in depth IR study on bridgmanite would be needed to be more conclusive on the matter.

1.5 X-ray diffraction

Two X-ray diffraction spectra were acquired during this work. The first was measured on the starting material at ambient conditions, using a Cu K–α source lab-scale instrument. The result of this measurement is shown in Fig. 5. Moreover, an in-situ X-ray diffraction (XRD) spectrum of the sample at ∼25 GPa was acquired at the ID27 high pressure beamline of the European Synchrotron facility (ESRF), which is equipped with a EIGER2 X CdTe 9M detector. This measurement is shown in Fig. 6. The data was refined and background corrected using the Dioptas software (Prescher and Prakapenka, 2015), and fitted using the PDIndexer software (Seto et al., 2010). The bridgmanite peaks were fitted to the equation of state by Horiuchi et al. (1987), and the resulting derived lattice parameters are reported in Table 2. The presence of the KCl pressure medium was also confirmed, with its most prominent peak being 110. Peaks of KCl were fitted according to the equation of state by Chidester et al. (2021). Both in Fig. 5 and Fig. 6, a few peaks could not be explained by bridgmanite or KCl, and were found to fit previous reports of superhydrous phase B X-ray diffraction bands (Pacalo and Parise, 2000). The presence of superhydrous phase B in the sample material can thus be confirmed based on these XRD measurements. The very low intensity of its peaks compared to bridgmanite means that superhydrous phase B would volumetrically only be a minor phase.

A high background was originally present, which could have been caused by partial amorphization. It is also possible that it was caused by an insufficiently high X-ray flux

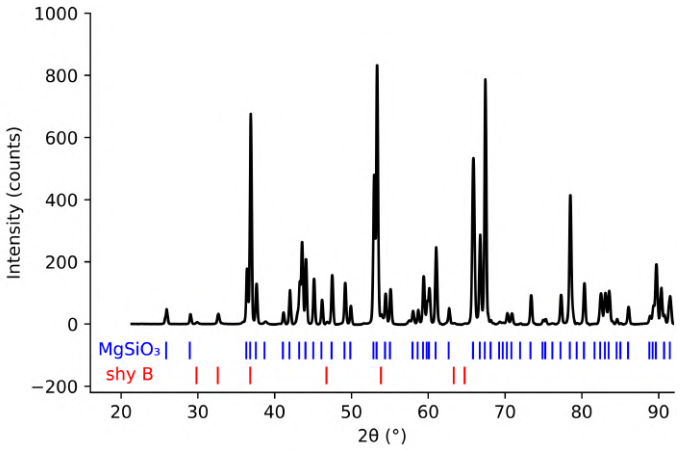

Figure 5: Background corrected X-ray diffraction spectrum of the sample material at ambient conditions.

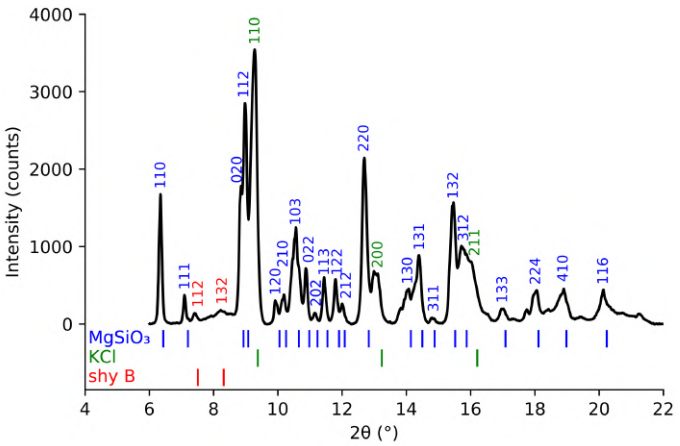

Figure 6: Background corrected X-ray diffraction spectrum of the sample material at ∼25 GPa.

Table 2: Fitted lattice parameters (a, b & c), unit cell volume, density and molar volume of the studied sample at ambient conditions and ∼25 GPa, based on the X-ray diffraction spectrum shown in Figs. 5 & 6.

	Ambient conditions	∼25 GPa
a	4.7810 ± 0.0036 Å	4.6822 ± 0.0036 Å
b	4.9368 ± 0.0040 Å	4.8618 ± 0.0040 Å
c	6.9173 ± 0.0063 Å	6.7570 ± 0.0063 Å
Unit Cell V	163.2710 ± 0.4272 $Å^3$	153.8159 ± 0.4272 $Å^3$
Density	4.0840 g/cm^{-3}	4.3410 g/cm^{-3}
Molar V	24.5811 cm^3/mol	23.1256 cm^3/mol

during measurement, considering the small sample size. A decrease in amount of peaks compared to an XRD spectrum of the starting material (not shown here) is not observed, indicating that the sample is unlikely to have significantly amorphized.

1.6 Atom Probe Tomography

In order to investigate the presence of H in the studied sample on an atomic level, Atom Probe Tomography (APT) measurements were performed on a 4000 X-HR Cameca Local Electrode Atom Probe (LEAP) at the ScopeM facilities of ETH. APT was first developed by Müller et al. (1968), that allows for three-dimensional mapping of atoms present in a sample at the nanoscale. For these measurements, a Focused Ion Beam had to firstly be used to prepare nm-scale tips out of the sample material (Fig. 7). For this, a TFS Helios 600i by Thermo Fisher Scientific with a Gallium source was utilized. APT is a destructive method, meaning that each atom gets evaporated from the tip illustrated in Fig. 7 due a strong electric field, in order to then arrive on the detector. The high electric field causes the surface atoms to become ionized and move away from the surface in order to achieve a lower energy state (Reddy et al., 2020). The identification of atoms being detected is based on time-of-flight mass spectrometry. After the entire material has evaporated and its atoms been detected, the result is a 3D atomic point cloud representing the sample

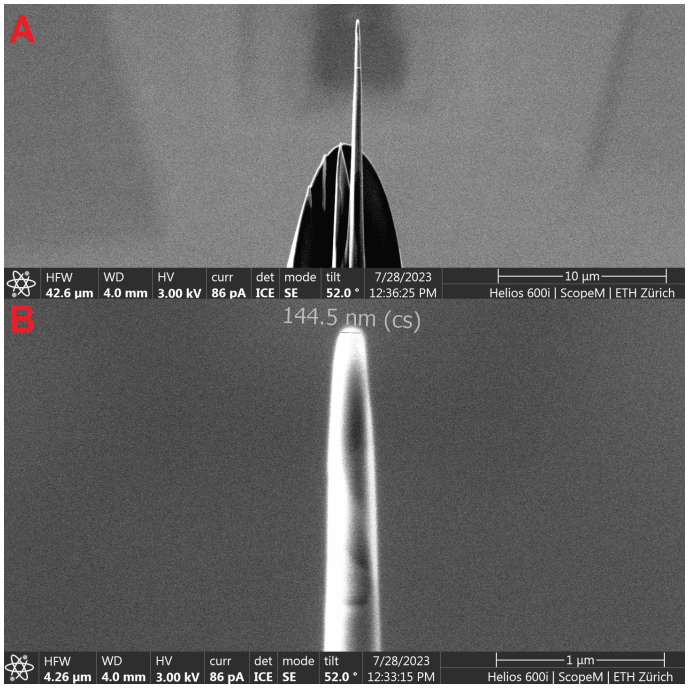

Figure 7: A. Scanning Electron Microscope images of a prepared sample tip for APT. B. Higher magnification image of the apex of the tip, showing that it was ultimately polished down to ∼145 nm in diameter before the APT measurement. This is however a rough estimate and usually an overestimation of its actual diameter.

tip.

The H atom point cloud distribution in hydrous bridgmanite is shown in Figure 8. The length of the entire tip is ∼120 nm. There are two surfaces with higher H concentrations going through the sample (Fig. 8). One goes through the sample laterally, creating what seems like a 'cap'. The second is slanting diagonally through the remaining part of the sample. The surfaces could be interpreted either as dislocations within a crystal or grain boundaries. The former would be more likely considering the previously observed µm-scale grain size of the sample using SEM imaging is much bigger than the scale of Fig. 8. A recent study looking at hydrous fayalite with APT observed similar nm-scale channels

Figure 8: 3D point cloud of hydrogen atoms in evaporated sample tip, which has a length of ∼120 nm and a diameter of ∼60 nm.

in their sample, which were more hydrated than the surrounding matrix (Liu et al., 2022). These were associated with Na that sample, and interpreted as 'hydrated defects', which is a broad description that could include dislocations.

Based on the illustrated sample volume in Figure 8, an ionic H concentration of 0.62 at.% was determined. This value was converted to wt% H_2O to compare it to the FTIR results with

$$wt\%\ H_2O = \frac{2 \times at\%_H \times M_H + at\%_H \times M_O}{\Sigma(at\%_i \times M_i)}, \tag{2}$$

where M is the atomic mass of a certain atom, and i represents every atom or molecule measured.

From 0.62 at% H, a H_2O concentration of 0.26 wt% or 2605 ppm wt H_2O is calculated. This is ∼2.5 times larger than the concentration measured by FTIR. A more detailed analysis of the 'enriched' surfaces revealed that they can contain anywhere between ∼0.9 at% and ∼2.0 at% H, corresponding to ∼0.38 wt% and ∼0.84 wt% H_2O respectively. The areas in between show concentrations in the range ∼0.3 at%-∼0.5 at% H, corresponding to

∼0.13–0.25 wt% (1261–2101 ppm) H_2O. With a spot size of 50 µm and sample thickness of 244 µm, FTIR samples a much larger region which is more representative of the bulk sample. It might thus be that the area measured here with APT is not representative of the whole sample.

The advantage of the APT method is that it is counting H atoms to determine the at% and is therefore not dependent on any calibration, unlike the FTIR water content calculation (Sec. 1.4). It is possible that the peaks in the range 1600–3200 cm^{-1} of the FTIR spectrum should also be considered for the water content calculations, and that the concentration is therefore underestimated. These results open up the discussion about the possibility that FTIR measurements could consistently be underestimating the water content in NAMs, which is an issue that should further be investigated.

1.7 Raman spectroscopy

Raman spectroscopy is used to determine the pressure in the sample chamber, and as a result, the depths in the mantle that the acquired data points correspond to. Two calibrations exist to characterize the pressure in the sample chamber of a DAC, (1) the ruby pressure calibration method (Shen et al., 2020) and (2) the high-frequency diamond edge calibration method (Akahama and Kawamura, 2004). A combination of both was used in this work. The ruby calibration is considered to be a more robust calibration compared to the diamond calibration at shallow lower mantle pressures, because it does not depend on previous knowledge of an equation of state (Shen et al., 2020). But, as mentioned in Section 1.3, the ruby was placed off-centered in the sample chamber to not affect the Brillouin measurements. In order to infer the 'ruby pressure' in the center of the sample, based on the measured off-centered value, the following equation was used:

$$P_{\text{ruby “at” center}} = P_{\text{diamond center}} - (P_{\text{diamond at ruby}} - P_{\text{ruby}}). \quad (3)$$

Thus, the difference between the diamond pressure at the ruby ($P_{\text{diamond at ruby}}$) and off-centered ruby pressure (P_{ruby}) was utilized to estimate what the equivalent ruby pressure would be at the center of the sample ($P_{\text{ruby "at" center}}$). The $P_{\text{diamond center}}$ is an average taken by making 3 to 4 measurements at slightly different locations in the center of the sample chamber, where the laser for Brillouin measurements would be focused. Diamond pressures were usually about 1–2 GPa higher than ruby pressures between 25 and 50 GPa. An exception on this method was made for the measurements at 65 and 80 GPa, because the ruby pressure showed unreasonable pressures ∼10 GPa higher than the diamond pressures. The ruby method is known to have higher uncertainties with increasing pressure, because of its fluorescence becoming weaker and it starting to become metastable around ∼80 GPa (Shen et al., 2020).

Raman spectroscopy can be sensitive to the presence of structurally bound OH-groups, usually through broad stretching bands in the 2900–3700 cm^{-1} range (Kleppe and Jephcoat, 2006). The starting material did not show any significant bands in this wavelength range though, most likely because ∼0.1 wt% H_2O does not suffice to form sufficient detectable OH bonds. Previous reports observing these bands usually used samples containing at least a few wt% H_2O.

Bolfan-Casanova et al. (2003) discarded the idea that water could be present in bridgmanite based on the interpretation that the FTIR peaks observed around 3400 cm^{-1} were caused by superhydrous phase B. This conclusion was made based on the observation of superhydrous phase B in measured Raman spectra. To investigate this issue, Raman spectra between 300 and 1000 cm^{-1} were measured at every pressure point. This corresponds to the wavelength range in which the most intense peaks should be present for both materials. Three Raman bands were consistently observed during these measurements, which are represented as a function of pressure in Fig 10. The comparison to previous

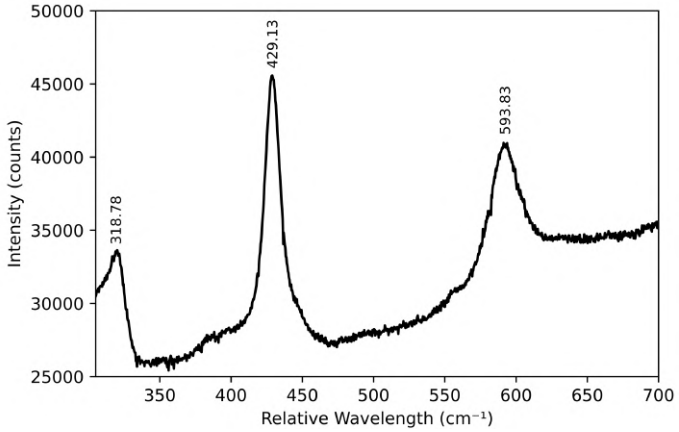

Figure 9: Raw Raman spectrum measured at ∼28 GPa, showing the three major bands of bridgmanite.

studies by Hemley et al. (1989) and Hofmeister et al. (1999), measuring the Raman bands of bridgmanite and superhydrous phase B respectively, clearly shows that the observed bands for the sample presented here are more in accordance with the former of those two works. All three bands correspond to A_g (symmetry maintaining) Raman active modes for bridgmanite. The slight deviation, especially at higher pressures, compared to Hemley et al. (1989) is most likely caused by the fact that the linear regression represented here is based on measurements below 25 GPa by Hemley et al. (1989). The presence of Al and H in bridgmanite can not be excluded to also have an influence on optic modes since they cause small changes to the lattice structure and bonding environment. No evidence was found in the literature supporting the idea that the presence of Al or H would influence the location of Raman bands in bridgmanite.

1.8 Brillouin spectroscopy

Brillouin scattering spectroscopy was used to determine the acoustic wave velocities of the sample, which are equivalent to seismic wave speeds, at every pressure point. A

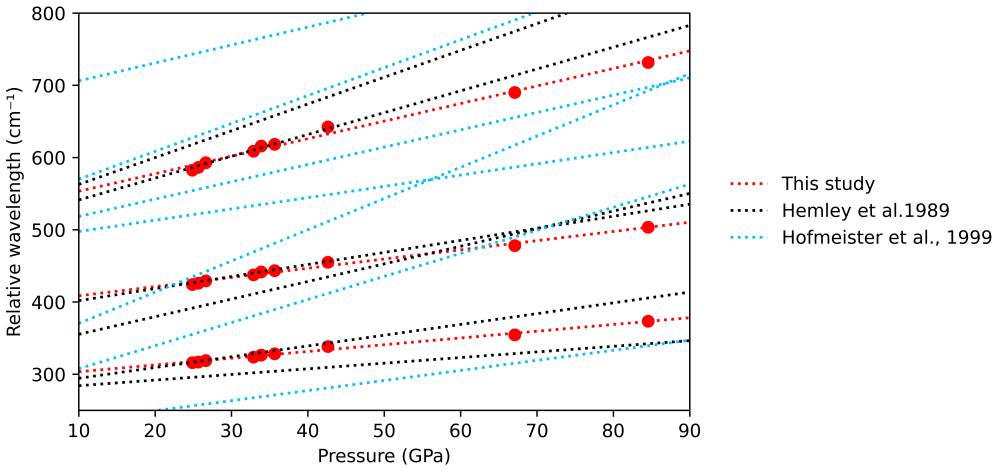

Figure 10: Raman bands measured at every pressure point compared to previous works by Hemley et al. (1989) on $MgSiO_3$ bridgmanite (blue) and Hofmeister et al. (1999) on superhydrous phase B (black). Dotted lines represent linear regressions on the data.

532 nm green laser which travels through the diamonds and sample material, was used to provoke elastic ('Rayleigh') and inelastic scattering by exciting the material on its way through. The frequency shift between the inelastically scattered wave and the laser itself getss detected by a Fabry-Pérot interferometer and is directly proportional to how fast the sample's atoms are vibrating, i.e. its acoustic velocity, according to Eq. 4.

$$V = \frac{\Delta\omega\lambda}{2sin(\frac{\theta}{2})}, \tag{4}$$

In Eq. 4, V stands for the acoustic velocity, $\Delta\omega$ for the frequency shift, λ for the laser wavelength, and θ for the scattering angle (fixed to 50° in the setup used for these measurements). Examples of raw data, and an overview of the Brillouin scattering results are given in section 2.1. The average measurement time for each measurement of this sample was two days. Due to the characterization of angular dispersion, multiple measurements were taken at every pressure point, making the average measurement time for

one pressure point about three weeks. Reason for this is also the relatively high number of measurements that were discarded due to the lack of detectable peaks.

2 Results

2.1 Brillouin scattering spectroscopy

Brillouin spectra were measured between 25 and 85 GPa. Example spectra of raw Brillouin scattering measurements are given in Figure 11. Depending on the exact location of the measurement on the sample and possibly the orientation of the DAC, one (Fig. 11A) or multiple peaks (Fig. 11B) were detected. The other peaks could be attributed to either KCl (the pressure medium), or superhydrous phase B. The extra peak at lower frequency in Figure 11B for example, corresponds to a velocity of 5.75 km/s at 33 GPa, which agrees quite well with the predicted shear wave velocity of superhydrous phase B at that pressure (Mookherjee and Tsuchiya, 2015; Rosa et al., 2015; Xu et al., 2022). The superhydrous phase B and bridgmanite peaks are clearly defined and distinguishable from each other, making it possible to fit their position separately in order to determine the corresponding frequency shift and acoustic velocity using Equation 4. Thus, even when other peaks are present in some spectra, the determination of the elasticity of hydrous bridgmanite sample is not affected. The compressional wave velocity of the sample overlaps with the more intense transverse acoustic modes of diamond and could therefore not be measured.

All the results from the Brillouin scattering measurements performed on the sample are shown in Figure 12. To make sure that the reported data is reproducible, several measurements were made at every pressure point to characterize the angular dispersion, by changing the orientation of the DAC by means of rotation. The errors on the the shear velocity (V_S) thus represent the standard deviation between these measurements and represent the angular dispersion of the polycrystalline sample. The errors in pressure represent the standard deviation of measured pressure before and after the Brillouin measurements.

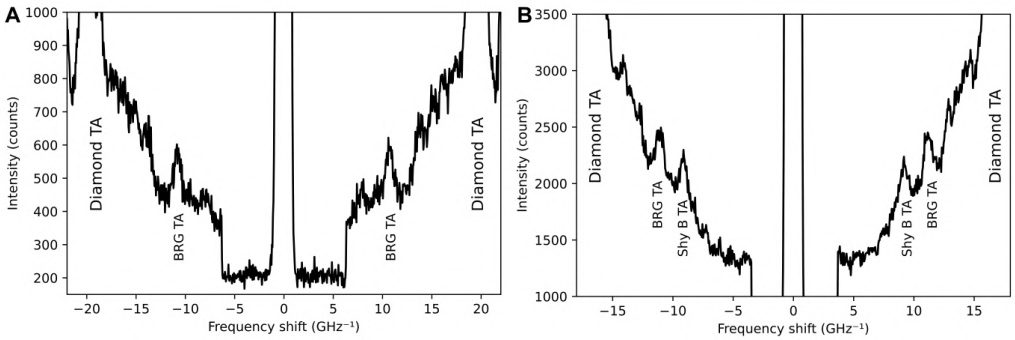

Figure 11: Raw, representative Brillouin scattering spectra of brigdmanite (BRG) and superhydrous phase B (Shy B) at pressures of ∼25 GPa (A) and ∼33 GPa (B). The Transverse Acoustic (TA) mode corresponds to the shear wave velocity of the material, and the Longitudinal Acoustic (LA) mode corresponds to its compressional wave velocity.

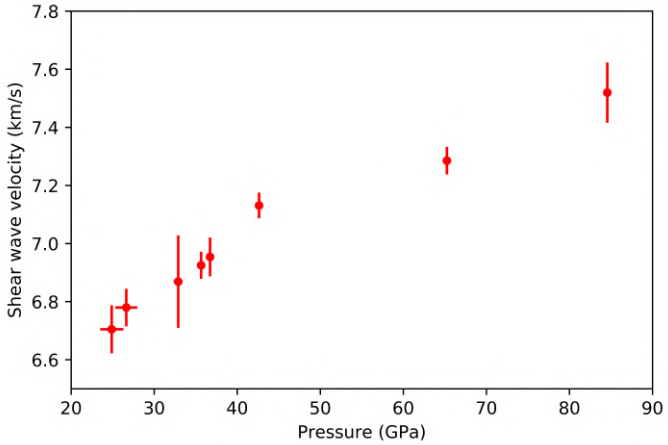

Figure 12: Shear wave velocities of the hydrous bridgmanite sample measured in this study as a function of pressure. All measurements were performed at ambient temperature. Multiple measurements were made at every pressure step, and averaged. The error bars are one standard deviation of these measurements.

3 Discussion

3.1 The effect of water on the elasticity of bridgmanite

To assess the effect of H on the elasticity of bridgmanite, the obtained shear wave velocity results for the measured bridgmanite sample in this study are compared to results by Murakami et al. (2007) and Murakami et al. (2012) in Figure 13. These studies were chosen because they also made measurements on polycrystalline bridgmanite samples and thus comparable to the sample studied here. Where Murakami et al. (2007) considered the pure Mg-endmember of bridgmanite, Murakami et al. (2012) investigated Al-bearing Mg-bridgmanite. From Fig. 13 it is seen that the measured H-bearing bridgmanite sample shows a somewhat different trend compared to the two other studies. At lower pressure, the measured S-wave velocities lie below the measurements of Murakami et al. (2007), while being similar to Murakami et al. (2012). With increasing pressure the S-wave velocity of the measured sample increases more rapidly than previously observed. An increase in S-wave velocity gradient, which indicates an increase in G_0', relative to pure $MgSiO_3$ (Murakami et al., 2007), was already observed in the Al-bearing bridgmanite sample of Murakami et al. (2012), with a cross-over in S-wave velocity occurring around 90–100 GPa. The sample measured here shows an increase in G_0' and thus an increase in S-wave velocity gradient, with a cross-over with pure $MgSiO_3$ at $\sim$55 GPa. Since this sample contains less Al than the sample measured by Murakami et al. (2012), this increase in S-wave velocity gradient cannot be explained simply by the presence of Al alone (although it likely contributes to some of it). The presence of hydrogen in the sample is the only feasible explanation for the increase in G_0'. The effect on the elasticity of bridgmanite (Fig. 13) due to the presence of H, is direct evidence that H is structurally incorporated into the crystal lattice. Intergranular or molecular water would not change

the elasticity of bridgmanite, and show up as separate peaks in the Brillouin spectra. The ubiquitous presence of H throughout the bridgmanite crystal observed in the APT images supports the presence of structurally incorporated water in the crystal.

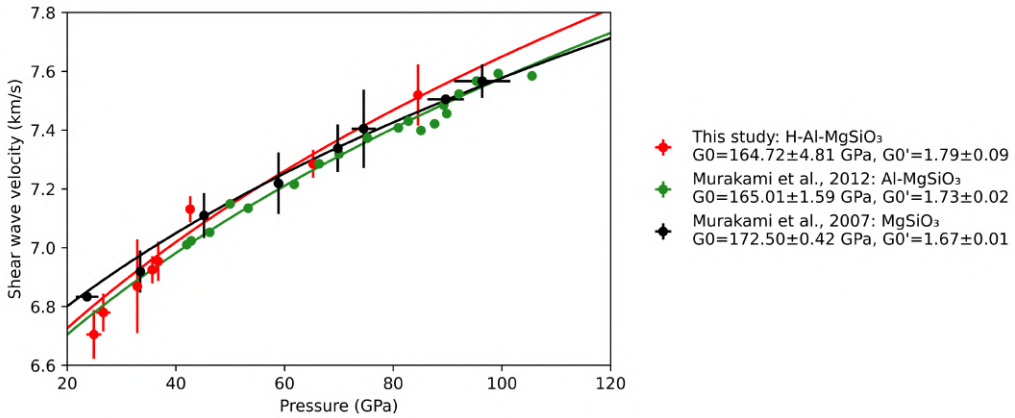

Figure 13: Brillouin scattering results from this study compared the data from Murakami et al. (2007) on pure $MgSiO_3$ and Murakami et al. (2012) on Al-$MgSiO_3$. Data points are fitted to a third-order Birch-Murnaghan Equation of State.

In order to quantify the steepness, the third-order Birch-Muranaghan equation of state represented was fit to all data in Figure 13.

$$G = (1+2f)^{5/2}[G_0 + (3K_0G_0' - 5G_0)f + (6K_0G_0' - 24K_0 - 14G_0 + \frac{9}{2}K_0K_0')f^2], \quad (5)$$

In Eq. 5, G is the shear modulus, G' the first pressure derivative of the shear modulus, K the bulk modulus, K' the first pressure derivative of the bulk modulus, and f the negative finite strain, which can further be expanded as a function of volume (V) as shown in Eq. 6.

$$f = \frac{1}{2}[(\frac{V}{V_0}^{-2/3}) - 1], \quad (6)$$

$$G' = \frac{\partial G}{\partial P} \quad (7)$$

The '0' subscript in Eq. 6 refers to the variable at ambient conditions. Equation 5 was chosen in order to make the effect of H or Al on its parameters comparable to previously reported third-order parameters (e.g. Stixrude and Lithgow-Bertelloni (2011)). For this, it is important that the same equation of state is used (Myhill et al., 2023).

Fitting the EoS to the measurements on hydrous bridgmanite allows to solve for G_0 and G'_0, which correspond to the y-axis intercept and slope of the fitted curve, respectively. As for the values of V_0, K_0, and K'_0, these are known for pure bridgmanite, but as in the case of the G_0, and G'_0, the presence of H and Al will affect V_0, K_0, and K'_0. Two X-ray diffraction spectra were measured for the sample studied here (see section 1.5), of which the first was taken at ambient conditions, resulting in a molar volume V_0=24.5811 cm^3/mol. Fu et al. (2023) experimentally investigated the effect of Al on the K_0 and K'_0 of bridgmanite, considering a sample containing 3.44% Al_2O_3. To quantify the effect of H on the bulk modulus, we employ values reported in the first-principles calculation of Jiang and Zhang (2019) because of lack of experimental data. Based on these calculations, a $K_0 = 247.395$ GPa and $K'_0 = 3.887$ is obtained for the sample measured in this study. A summary of the thermodynamic parameters calculated using the third-order Birch-Murnaghan EoS (Eq. 5) and the resulting G_0 and G'_0 are given in Table 3.

The results from finite strain fitting the measurements in Fig. 13 confirm the aforementioned increase in G'_0. Even though the presence of hydrogen does not seem to have a huge effect on G_0 of bridgmanite, a clear gradual increase in G'_0 from pure Mg-bridgmanite over Al-bearing bridgmanite to Al-H-bearing bridgmanite is observed, although it should be noted that the Al contents of the sample studied here and those of Murakami et al. (2012) are different. There is 0.5 wt% less Al_2O_3 in the sample studied here, meaning that its effect on G_0 and G'_0 should be less pronounced than in Murakami et al. (2012). As indicated in Fig. 13, the G_0 and G'_0 calculated for hydrous bridgmanite deviate more

Table 3: Summary of the thermodynamic parameters used in the finite strain fitting of experimental data, including G_0 and G_0' resulting from Equation 5. MUR2007 stands for Murakami et al. (2007) and MUR2012 stands for Murakami et al. (2012).

	Composition	G_0 (GPa)	G_0'
This study	$MgSiO_3$ + 3.44 wt.% Al_2O_3 + 0.11 wt.% H_2O	164.72±4.71	1.78±0.09
Murakami et al. (2012)	$MgSiO_3$ + 4.00 wt.% Al_2O_3	165.01±1.59	1.73±0.02
Murakami et al. (2007)	$MgSiO_3$	172.50±0.42	1.67±0.01

strongly from the pure bridgmanite values reported by Murakami et al. (2007) compared to those of Murakami et al. (2012), providing evidence in support for the strong effect of H on the elasticity of bridgmanite.

As mentioned in Section 1.2, Jackson et al. (2005) has also measured a polycrystalline Al-bearing bridgmanite sample using Brillouin scattering spectroscopy. The comparison of the studies depicted in Fig. 13 and the data measured by Jackson et al. (2005) is shown in Fig. 14. Jackson et al. (2005) reports a G_0 of 165 ± 2 GPa and a G_0' of 1.7 ± 0.2. These are similar values to the reported data by Murakami et al. (2012), but plotting and fitting all measurements in Fig. 14 shows that the measurements from Jackson et al. (2005) have generally higher velocities, with a G_0 closer to 168 GPa according to the fit shown here. The slope of the finite strain curve remains quite close to what was observed by Murakami et al. (2012) though (1.74 according to this fit), meaning that the effect of water on elasticity remains valid. The finite strain fit on water-bearing bridgmanite is steeper than any of the previously observed data on polycrystalline bridgmanite.

A clear decrease in shear wave velocities compared to the dry bridgmanite endmember is not clearly observed in Fig. 13. This is unlike olivine, wadsleyite and ringwoodite, where the addition of water was often reported to make the material softer (Holl et al., 2008; Yusa et al., 2000; Smyth et al., 2004; Inoue et al., 1998; Wang et al., 2003, 2006;

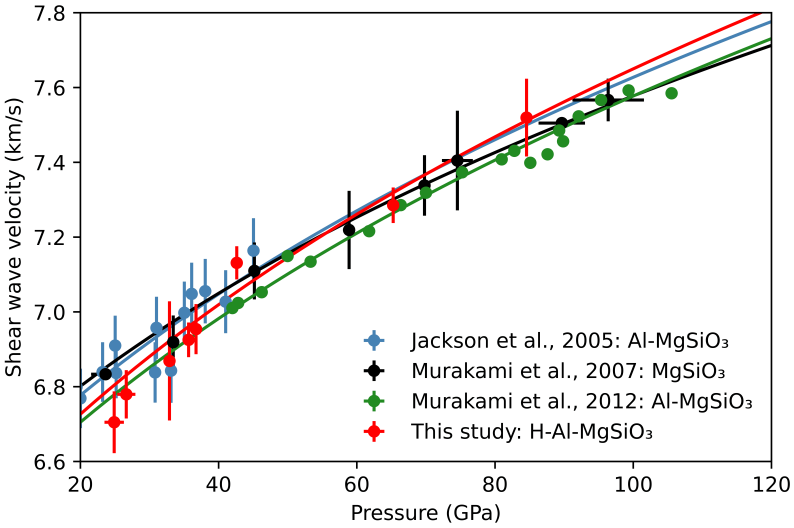

Figure 14: Brillouin scattering results from this study compared the data from Murakami et al. (2007), Murakami et al. (2012) and Jackson et al. (2005). Data points are fitted to a third-order Birch-Murnaghan Equation of State.

Jacobsen et al., 2004; Jacobsen, 2018; Ye et al., 2012). Most of these studies also report an increase in G_0' or K_0' with increasing H content, i.e. steeper compression slopes. This increase in steepness was also observed the measurements on hydrous bridgmanite, and thus seems to go hand in hand with the incorporation of water. Physically, a steeper trend means that the sample becomes less compressible or stiffer, compared to its anhydrous counterpart. Holl et al. (2008) propose that this could be a caused by strong repulsive O–O forces in the vicinity of vacancies, which would result in more rapid stiffening of the material. An alternative explanation could be that materials devoid of H would contain more empty vacancies in their crystal lattice and therefore be more compressible. Studies on metal structures have clearly shown that H tends to occupy otherwise vacant sites (Sakamaki et al., 2009; Abeykoon et al., 2023). The filling of these vacancies would reduce the mineral's compressibility. The observation of this phenomenon in metal structures

does not automatically mean it also happens in silicates. The introduction of Al into bridgmanite is likely to provoke the creation of defects in the crystal lattice though, which could allow for the presence of unoccupied sites.

Finally, based on peaks in some Brillouin spectra, and the XRD results, superhydrous phase B is concluded to likely present in between the grains. Its presence does however not affect the elasticity of bridgmanite. As discussed, whether the peaks around 3400 cm^{-1} in the FTIR spectrum are caused by superhydrous phase B or bridgmanite itself is difficult to determine, because OH stretching bands have been reported around this wavelength for both superhydrous phase B and bridgmanite. The absence of any superhydrous phase B bands in the measured Raman spectra (Fig. 10), combined with its very weak signal in the XRD spectrum, support that very little superhydrous phase B would be present volumetrically and it is therefore unlikely that the FTIR bands are caused by it alone. Moreover, Amulele et al. (2021) argue that the hydrous bridgmanite phase would be difficult to quench, with some of the water going into superhydrous phase B upon cooling. The water in superhydrous phase B would thus most likely actually be present in bridgmanite at lower mantle conditions. The calculated water content of ∼0.1 wt.% from FTIR is therefore likely to at least represent the water content of bridgmanite when it was synthesized, and its effect on the elasticity of bridgmanite measured here would therefore represent a lower limit if any water did indeed go into superhydrous phase B upon quenching.

3.2 Geophysical implications

To estimate the impact of H on lower mantle elasticity with a view to establishing bounds on the potential lower-mantle water content, lower-mantle shear-wave velocity (V_S) profiles were constructed and compared to the Preliminary Reference Earth Model (PREM)

by Dziewonski and Anderson (1981). For this, a lower mantle made up principally of bridgmanite and ferropericlase was assumed and the modelling package Burnman (Myhill et al., 2023) was used to construct S-wave velocity profiles for a range of bridgmanite/ferropericlase ratios with and without H, i.e., "wet" and "dry". In order to quantify the effect of H on the G_0 and G_0' of bridgmanite, the effect of Al and Fe alone had to be isolated first. For this, the equations reported in Murakami et al. (2024) were adopted as shown in Eqs. 8–9, where the coefficients for of Al_2O_3 and Fe/(Fe+Mg) are expressed in wt.% and mole respectively. The difference between the G_0 and G_0' of pure Mg-bridgmanite and the Al-corrected G_0 and G_0' from the sample studied here could then be quantified through linear interpolation in order to assess the effect of H, adding the last term in Eqs. 8–9. From these equations, the large coefficients for H_2O show that it has a bigger influence on the shear modulus and its first pressure derivative, compared to aluminum or iron. This is not surprising, as H is known to have disproportionately large effects on the physical properties of minerals even at low concentrations. In a lower mantle setting, very small amounts of H could thus have a comparably large effect on the elasticity of bridgmanite, comparable to much larger concentrations of Al and Fe.

$$G_0 = 172.83 - 1.71 \text{ GPa} \times Al_2O_3 - 27.83 \times \frac{\text{Fe}}{\text{Fe} + \text{Mg}} - 16.2373 \times H_2O \tag{8}$$

$$G_0' = 1.79 + 8.11 \times 10^{-5} \text{ GPa} \times Al_2O_3 - 0.33 \times \frac{\text{Fe}}{\text{Fe} + \text{Mg}} + 0.9973 \times H_2O \tag{9}$$

For the purpose of comparing the so-constructed lower-mantle seismic profiles with a radial seismic reference model, the laboratory-based peridotite geotherm of Katsura (2022) is used, in combination with the PREM. PREM satisfies a large set of normal-mode, body wave, stronomic-geodetic constraints and inversion of normal-mode centre frequencies, and therefore represents the most efficient means of determining the average

radial seismic structure of the Earth (Dziewonski and Anderson, 1981). For the "dry" mantle, a bridgmanite containing 4 mol% Al_2O_3 and 8 mol% FeO was considered, mixed with ferropericlase containing 21 mol% FeO after Wood (2000). For a "wet" mantle, 0.1 wt% H_2O is added to the bridgmanite component, according to the effect of H on G_0 and G_0' established in Eqs. 8 & 9. The choice of adding 0.1 wt% H_2O into bridgmanite is arbitrary, and was made because the sample used in this study had this concentration. This H_2O content has also been reported to be close to the saturation limit of bridgmanite (Amulele et al., 2021). In order to determine the seismic velocity of an assemblage consisting of more than one mineral, the correct averaging scheme has to be applied. This is quite straightforward for most thermodynamic parameters, except for the bulk and shear moduli, which are dependent on mineral orientation and distribution (Cottaar et al., 2014). To resolve this issue, several averaging schemes can be used to calculate the shear and bulk moduli of an assemblage, with the Voigt-Reuss-Hill and Hashin-Shtrikman averaging schemes deemed best practice (Cottaar et al., 2014).

Figure 15 shows the dry and wet mixtures of bridgmanite and ferropericlase compared to PREM. Mixtures of 100% bridgmanite-0% ferropericlase, and 90% bridgmanite-10% ferropericlase are depicted. The width of the profiles is the result of considering the errors on temperatures reported by Katsura (2022) and adding variation to the G_0, G_0', K_0 and K_0' parameters. As visible in this figure, the slope of these mixtures does not correspond exactly to PREM. PREM is faster (positive dV_S) than a certain mixture of brigmanite and ferropericlase at lower pressures, becoming slower (negative dV_S) or similar at higher pressures. Two main possibilities exist to explain this difference in slope. Either the ratio of bridgmanite and ferropericlase changes throughout the lower mantle, with the amount of ferropericlase increasing towards higher depths, or increased concentrations of certain elements at different depths affect the seismic velocities in either bridgmanite or

ferropericlase (Gaetani and Grove, 1998). The depth-dependent ferropericlase abundance would be somewhat difficult to explain, and would also have important geodynamical implications, since the viscosity of ferropericlase is lower than that of bridgmanite and the lower mantle would thus have to become more viscous with depth. How the abundance of Fe, Al & H affect the wave velocities of lower mantle minerals has to therefore thoroughly be investigated. Previously, the pyrolite model was thought to be representative of the lower mantle (Irifune et al., 2010). More recent studies have shown that this is unlikely the case, with a much larger percentage of bridgmanite needed to fit PREM due to the effect Fe and Al have on decreasing its body wave velocities (e.g., Murakami et al., 2012; Mashino et al., 2020).

The effect of water on the seismic velocity of bridgmanite explored in this work cannot help to explain the discrepancy though, as presented in Figure 15. At the top of the lower mantle, its seismic velocities are similar to dry bridgmanite, after which is starts to show a much steeper trend. After crossing over PREM, the gap between the two increases again as it becomes faster. Based on this observation, it seems unlikely that the lower mantle would contain a significant amount of water. The most important variable in a qualitative comparison like this one is the slope of the trends, and the slope for the dry assemblages is clearly closer to PREM compared to the dry assemblages.

It is important to note that PREM is a 1D model, representing an average for the entire mantle (Marquardt and Thomson, 2020). Seismic tomography studies have shown that the mantle shows important lateral variations in velocity profiles. Thus, even though the addition of H does not seem to fit the PREM profile for the lower mantle, it cannot be excluded that H does not play a role in certain regions of the lower mantle where positive sound velocity anomalies are observed.

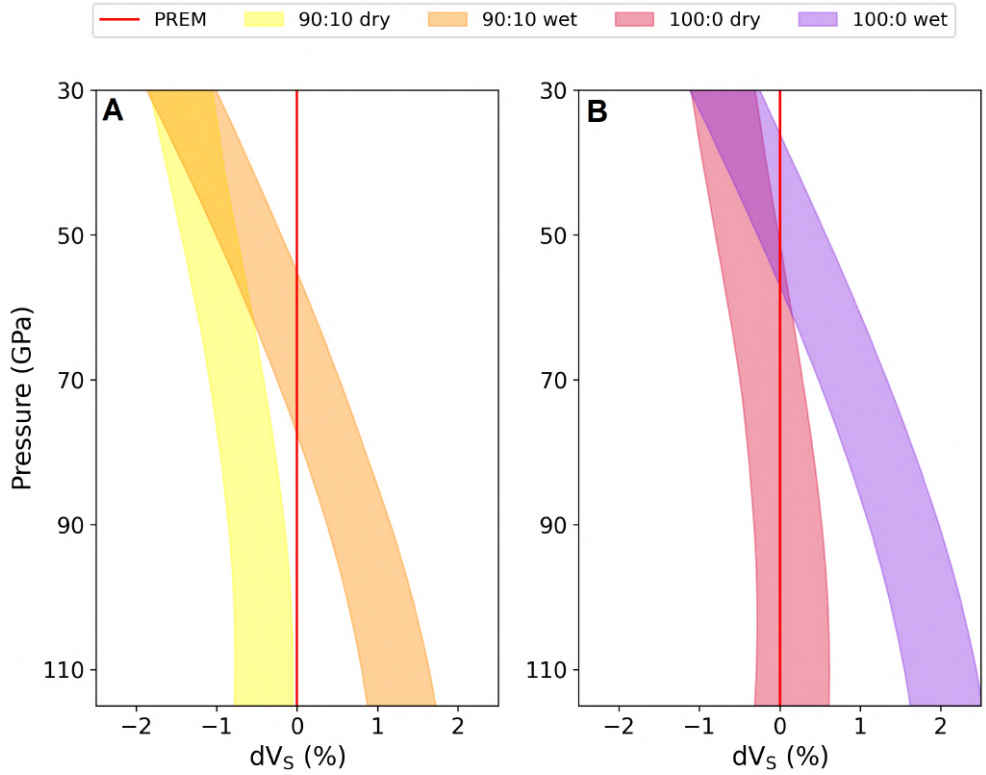

Figure 15: Dry and hydrous bridgmanite mixtures with ferropericlase, compared to PREM. (A) Velocity profiles of 90% BRG-10% FP dry and wet mixtures relative to PREM. (B) Velocity profiles of 100% BRG-0% FP dry and wet mixtures relative to PREM. All velocities are calculated along the geotherm by Katsura (2022). Vs = Shear wave velocity. BRG = bridgmanite containing 8 mol% FeO and 4 mol% Al_2O_3. HBRG = bridgmanite containing 8 mol% FeO, 4 mol% Al_2O_3 and 0.1 wt% H_2O. FP = ferropericlase containing 21 mol% FeO.

Conclusion

This study on bridgmanite showed that water can indeed be incorporated structurally into its crystal lattice, by observing its effect on elasticity. A clear decrease in G_0 and increase in G_0' (Eq. 5) caused by the presence of water was observed. The exact quantification of water by FTIR in the bridgmanite sample is difficult due to the presence of a small amount of superhydrous phase B alongside the sample. The use of Atom Probe Tomography to characterize the water distribution in the sample is promising, despite the small sample size, and the authors recommend its usage in future studies.

Based on the analysis of the shear wave velocity data in this study, the potential effect of water in the lower mantle was modeled and compared to PREM. This comparison showed that the Earth's lower mantle is unlikely to contain a significant amount of water. Unlike the transition zone, the lower mantle would thus not be a major water reservoir for the Earth.

Author Contribution Statement

T.d.S.-D. and M.M. designed research; T.d.S.-D. performed research with frequent input from M.M. T.d.S.-D. analyzed data; L.M. performed water quantification from atom probe measurements; T.Y. synthesized the starting material; T.d.S.-D. wrote the manuscript, with input from A.K. for the discussion; Y.Z. and S.K. performed the FTIR and XRD measurements at ambient conditions; F.M. and A.K. created the code that was built upon for the modeling of results compared to PREM.

Acknowledgments

The authors are grateful to Ning Ma for performing the XRD measurement at the ESRF facility; Pinku Saha for help with the Burnman modeling; Mona Lueder for help with the FTIR measurements; Stephan Gerstl for help with the APT measurements and FIB sample preparation. Funding for this project was provided by Prof. Dr. Motohiko Murakami, partly through the ETH+ grant.

References

Abeykoon, S., Howard, C., Dominijanni, S., Eberhard, L., Kurnosov, A., Frost, D. J., Ballaran, T. B., Terasaki, H., Sakamaki, T., Suzuki, A., Ohtani, E., Sano-Furukawa, A., and Abe, J. (2023). Deuterium Content and Site Occupancy in Iron Sulfide at High Pressure and Temperature Determined Using In Situ Neutron Diffraction Measurements. Journal of Geophysical Research: Solid Earth, 128(9).

Akahama, Y. and Kawamura, H. (2004). High-pressure Raman spectroscopy of diamond anvils to 250 GPa: Method for pressure determination in the multimegabar pressure range. Journal of Applied Physics, 96(7):3748–3751.

Amulele, G., Karato, S. I., and Girard, J. (2021). Melting of Bridgmanite Under Hydrous Shallow Lower Mantle Conditions. Journal of Geophysical Research: Solid Earth, 126.

Andrault, D., Bolfan-Casanova, N., Bouhifd, M. A., Guignot, N., and Kawamoto, T. (2007). The role of Al-defects on the equation of state of Al–$(Mg, Fe)SiO_3$ perovskite. Earth and Planetary Science Letters, 263:167–179.

Andrault, D., Neuville, D., Flank, A.-M., and Wang, Y. (1998). Cation sites in Al-rich $MgSiO_3$ perovskites. American Mineralogist, 83:1045–1053.

Ballaran, T. B., Frost, D. J., Miyajima, N., and Heidelblbach, F. (2010). The structure of a superaluminous version of the dense hydrous-magnesium silicate phase D. American Mineralogist, 95:1113–1116.

Ballaran, T. B., Kurnosov, A., Glazyrin, K., Frost, D. J., Merlini, M., Hanfland, M., and Caracas, R. (2012). Effect of chemistry on the compressibility of silicate perovskite in the lower mantle. Earth and Planetary Science Letters, 333-334:181–190.

Bolfan-Casanova, N. (2005). Water in the Earth's mantle. Mineralogical Magazine, 69:229–257.

Bolfan-Casanova, N., Keppler, H., and Rubie, D. C. (2000). Water partitioning between nominally anhydrous minerals in the MgO-SiO_2-H_2O system up to 24 GPa: Implications for the distribution of water in the Earth's mantle. Earth and Planetary Science Letters, 182:209–221.

Bolfan-Casanova, N., Keppler, H., and Rubie, D. C. (2003). Water partitioning at 660 km depth and evidence for very low water solubility in magnesium silicate perovskite. Geophysical Research Letters, 30:1–4.

Brodholt, J. P. (2000). Pressure-induced changes in the compression mechanism of aluminous perovskite in the Earth's mantle. Nature, 407:620–622.

Catalli, K., Shim, S. H., Dera, P., Prakapenka, V. B., Zhao, J., Sturhahn, W., Chow, P., Xiao, Y., Cynn, H., and Evans, W. J. (2011). Effects of the Fe^{3+} spin transition on the properties of aluminous perovskite-New insights for lower-mantle seismic heterogeneities. Earth and Planetary Science Letters, 310:293–302.

Catalli, K., Shim, S. H., Prakapenka, V. B., Zhao, J., Sturhahn, W., Chow, P., Xiao, Y., Liu, H., Cynn, H., and Evans, W. J. (2010). Spin state of ferric iron in $MgSiO_3$ perovskite and its effect on elastic properties. Earth and Planetary Science Letters, 289:68–75.

Chantel, J., Frost, D. J., McCammon, C. A., Jing, Z., and Wang, Y. (2012). Acoustic velocities of pure and iron-bearing magnesium silicate perovskite measured to 25 GPa and 1200 K. Geophysical Research Letters, 39:L19307.

Chidester, B. A., Thompson, E. C., Fischer, R. A., Heinz, D. L., Prakapenka, V. B., Meng, Y., and Campbell, A. J. (2021). Experimental thermal equation of state of B2-KCl. Physical Review B, 104:94107.

Cottaar, S., Heister, T., Rose, I., and Unterborn, C. (2014). Burnman: A lower mantle minerals physics toolkit. Geochemistry, Geophysics, Geosystems, 15:1164–1179.

Criniti, G., Kurnosov, A., Boffa Ballaran, T., and Frost, D. J. (2021). Single-Crystal Elasticity of $MgSiO_3$ Bridgmanite to Mid-Lower Mantle Pressure. Journal of Geophysical Research: Solid Earth, 126.

Cynn, H., Hofmeister, A. M., Burnley, P. C., and Navrotsky, A. (1996). Thermodynamic properties and hydrogen speciation from vibrational spectra of dense hydrous magnesium silicates. Physics and Chemistry of Minerals, 23:361–376.

Daniel, I., Bass, J. D., Fiquet, G., Cardon, H., Zhang, J., and Hanfland, M. (2004). Effect of aluminium on the compressibility of silicate perovskite. Geophysical Research Letters, 31:L15608.

Davies, R. M., Griffin, W. L., O'Reilly, S. Y., and Doyle, B. J. (2004). Mineral inclusions and geochemical characteristics of microdiamonds from the DO27, A154, A21, A418, DO18, DD17 and Ranch Lake kimberlites at Lac de Gras, Slave Craton, Canada. Lithos, 77:39–55.

Dziewonski, A. M. and Anderson, D. L. (1981). Preliminary reference Earth model. Physics of the Earth and Planetary Interiors, 25:297–356.

Fiquet, G., Dewaele, A., Andrault, D., Kunz, M., and Le Bihan, T. (2000). Thermoelastic properties and crystal structure of $MgSiO_3$ perovskite at lower mantle pressure and temperature conditions. Geophysical Research Letters, 27(1):21–24.

Frost, D. J. and Langenhorst, F. (2002). The effect of Al_2O_3 on Fe–Mg partitioning between magnesiowüstite and magnesium silicate perovskite. Earth and Planetary Science Letters, 199:227–241.

Fu, S., Yang, J., Karato, S., and Vasiliev, A. (2019a). Water Concentration in Single-Crystal (Al,Fe)-Bearing Bridgmanite Grown From the Hydrous Melt: Implications for Dehydration Melting at the Topmost Lower Mantle. Geophysical Research Letters, pages 346–357.

Fu, S., Yang, J., Tsujino, N., Okuchi, T., Purevjav, N., and Lin, J. F. (2019b). Single-crystal elasticity of (Al,Fe)-bearing bridgmanite and seismic shear wave radial anisotropy at the topmost lower mantle. Earth and Planetary Science Letters, 518:116–126.

Fu, S., Yang, J., Zhang, Y., Okuchi, T., McCammon, C., Kim, H. I., Lee, S. K., and Lin, J. F. (2018). Abnormal Elasticity of Fe-Bearing Bridgmanite in the Earth's Lower Mantle. Geophysical Research Letters, 45:4725–4732.

Fu, S., Zhang, Y., Okuchi, T., and Lin, J. F. (2023). Single-crystal elasticity of (Al,Fe)-bearing bridgmanite up to 82 GPa. American Mineralogist, 108:719–730.

Gaetani, G. A. and Grove, T. L. (1998). The influence of water on melting of mantle peridotite. Contributions to Mineralogy and Petrology, 131:323–346.

Glazyrin, K., Boffa Ballaran, T., Frost, D. J., McCammon, C., Kantor, A., Merlini, M., Hanfland, M., and Dubrovinsky, L. (2014). Magnesium silicate perovskite and effect of iron oxidation state on its bulk sound velocity at the conditions of the lower mantle. Earth and Planetary Science Letters, 393:182–186.

Hemley, R. J., Cohen, R. E., Yeganeh-Haeri, A., Mao, H. K., Weidner, D. J., and Ito, E. (1989). Raman spectroscopy and lattice dynamics of $MgSiO_3$-perovskite at high pressure. Geophysical Monograph Series, 45:35–44.

Higo, Y., Inoue, T., and Irifune, T. (2001). Effect of water on the spinel-postspinel transformation in Mg_2SiO_4. Geophysical Research Letters, 28(18):3505–3508.

Hirose, K. (2006). Postperovskite phase transition and its geophysical implications. Reviews of Geophysics, (RG3001).

Hofmeister, A. M., Cynn, H., Burnley, P. C., and Meade, C. (1999). Vibrational spectra of dense, hydrous magnesium silicates at high pressure: Importance of the hydrogen bond angle. American Mineralogist, 84:454–464.

Holl, C. M., Smyth, J. R., Jacobsen, S. D., and Frost, D. J. (2008). Effects of hydration on the structure and compressibility of wadsleyite, β-(Mg_2SiO_4). American Mineralogist, 93:598–607.

Holzapfel, C., Rubie, D. C., Frost, D. J., and Langenhorst, F. (2005). Geophysics: Fe-Mg interdiffusion in $(Mg, Fe)SiO_3$ perovskite and lower mantle reequilibration. Science, 309:1707–1710.

Horiuchi, H., Ito, E., and Weidner, D. J. (1987). Perovskite-type $MgSiO_3$: Single-crystal X-ray diffraction study. American Mineralogist, 72:357–360.

Huang, R., Boffa Ballaran, T., McCammon, C. A., Miyajima, N., and Frost, D. J. (2021). The Effect of Fe-Al Substitution on the Crystal Structure of $MgSiO_3$ Bridgmanite. Journal of Geophysical Research: Solid Earth, 126.

Inoue, T., Wada, T., Sasaki, R., and Yurimoto, H. (2010). Water partitioning in the Earth's mantle. Physics of the Earth and Planetary Interiors, 183(1-2):245–251.

Inoue, T., Weidner, D. J., Northrup, P. A., and Parise, J. B. (1998). Elastic properties of hydrous ringwoodite (γ-phase) in Mg_2SiO_4. Earth and Planetary Science Letters, 160:107–113.

Irifune, T., Koizumi, T., and Ando, J. I. (1996). An experimental study of the garnet-perovskite transformation in the system $MgSiO_3$-$Mg_3Al_2Si_3O_{12}$. Physics of the Earth and Planetary Interiors, 96:147–157.

Irifune, T., Shinmei, T., McCammon, C. A., Miyajima, N., Rubie, D. C., and Frost, D. J. (2010). Iron partitioning and density changes of pyrolite in Earth's lower mantle. Science, 327:193–195.

Ishii, T., Ohtani, E., and Shatskiy, A. (2022). Aluminum and hydrogen partitioning between bridgmanite and high-pressure hydrous phases: Implications for water storage in the lower mantle. Earth and Planetary Science Letters, 583:117441.

Jackson, J. M., Zhang, J., Shu, J., Sinogeikin, S. V., and Bass, J. D. (2005). High-pressure sound velocities and elasticity of aluminous $MgSiO_3$ perovskite to 45 GPa: Implications for lateral heterogeneity in Earth's lower mantle. Geophysical Research Letters, 32:L21305.

Jacobsen, S. D. (2018). Effect of Water on the Equation of State of Nominally Anhydrous Minerals. Water in Nominally Anhydrous Minerals, 62:321–342.

Jacobsen, S. D., Demouchy, S., Frost, D. J., Ballaran, T. B., and Kung, J. (2005). A systematic study of OH in hydrous wadsleyite from polarized FTIR spectroscopy and single-crystal X-ray diffraction: Oxygen sites for hydrogen storage in Earth's interior. American Mineralogist, 90:61–70.

Jacobsen, S. D., Smyth, J. R., Spetzler, H., Holl, C. M., and Frost, D. J. (2004). Sound velocities and elastic constants of iron-bearing hydrous ringwoodite. Physics of the Earth and Planetary Interiors, 143:47–56.

Jiang, J. and Zhang, F. (2019). Theoretical studies on the hydrous lower mantle and D″ layer minerals. Earth and Planetary Science Letters, 525:115753.

Kaminsky, F. V. (2018). The Earth 's Lower Mantle. Springer Geology.

Karato, S. (2008). Effects of pressure and water. In Deformation of Earth Materials: An Introduction to the Rheology of Solid Earth, chapter 10, pages 168–198. Cambridge Universtiy Press.

Katsura, T. (2022). A Revised Adiabatic Temperature Profile for the Mantle. Journal of Geophysical Research: Solid Earth, 127:1–11.

Kleppe, A. K. and Jephcoat, A. P. (2006). Raman spectroscopic studies of hydrous and nominally anhydrous deep mantle phases. Geophysical Monograph Series, 168:69–93.

Kojitani, H., Katsura, T., and Akaogi, M. (2007). Aluminum substitution mechanisms in perovskite-type $MgSiO_3$: An investigation by Rietveld analysis. Physics and Chemistry of Minerals, 34:257–267.

Kovács, I., Hermann, J., O'Neill, H. S. C., Gerald, J. F., Sambridge, M., and Horváth, G. (2008). Quantitative absorbance spectroscopy with unpolarized light: Part II. Experimental evaluation and development of a protocol for quantitative analysis of mineral IR spectra. American Mineralogist, 93:765–778.

Kudoh, Y., Prewitt, C. T., and Finger, L. W. (1990). Effect of Iron on the Crystal Structure of $(Mg, Fe)SiO_3$ Perovskite. Structure, 17(10):1481–1484.

Kurnosov, A., Marquardt, H., Frost, D. J., Boffa Ballaran, T., and Ziberna, L. (2017). Evidence for a Fe^{3+}-rich pyrolitic lower mantle from (Al,Fe)-bearing bridgmanite elasticity data. Nature, 543:543–546.

Lemaire, C., Kohn, S. C., and Brooker, R. A. (2004). The effect of silica activity on the incorporation mechanisms of water in synthetic forsterite: A polarised infrared spectroscopic study. Contributions to Mineralogy and Petrology, 147:48–57.

Li, B. and Zhang, J. (2005). Pressure and temperature dependence of elastic wave velocity of $MgSiO_3$ perovskite and the composition of the lower mantle. Physics of the Earth and Planetary Interiors, 151(1-2).

Li, L., Brodholt, J. P., Stackhouse, S., Weidner, D. J., Alfredsson, M., and Price, G. D. (2005). Elasticity of $(Mg\,Fe)(Si, Al)O_3$-perovskite at high pressure. Earth and Planetary Science Letters, 240:529–536.

Libowitzky, E. (2016). Correlation of O-H Stretching Frequencies and O-H—O Hydrogen Bond Lengths in Minerals. In Schuster, P. and Mikenda, W., editors, Hydrogen Bond Research, pages 1–23. Springer-Verlag Wien.

Libowitzky, E. and Beran, A. (2006). The structure of hydrous species in nominally anhydrous minerals: Information from Polarized IR spectroscopy. In Keppler, H. and Smyth, J. R., editors, Reviews in Mineralogy & Geochemistry: Water in Nominally Anhydrous Minerals, volume 62, pages 29–52. Mineralogical Society of America.

Litasov, K. and Ohtani, E. (2003). Hydrous lower mantle: the water source for wet plumes? In 8th International Kimberlite Conference, number FLA030, Victoria, BC. Elsevier.

Liu, J., Taylor, S. D., Qafoku, O., Arey, B. W., Colby, R., Eaton, A., Bartrand, J., Shutthanandan, V., Manandhar, S., and Perea, D. E. (2022). Visualizing the Distribution of Water in Nominally Anhydrous Minerals at the Atomic Scale: Insights From Atom Probe Tomography on Fayalite. Geophysical Research Letters, 49.

Liu, L.-G. (1974). Silicate perovskite from phase transformations of pyrope-garnet at high pressure and temperature. Geophysical Research Letters, 1:277–280.

Liu, Z., Fei, H., Chen, L., Mccammon, C., Wang, L., Liu, R., Wang, F., Liu, B., and Katsura, T. (2021). Bridgmanite is nearly dry at the top of the lower mantle. Earth and Planetary Science Letters, 570:117088.

Liu, Z., Irifune, T., Nishi, M., Tange, Y., Arimoto, T., and Shinmei, T. (2016). Phase relations in the system $MgSiO_3$-Al_2O_3 up to 52 GPa and 2000 K. Physics of the Earth and Planetary Interiors, 257:18–27.

Lundin, S., Catalli, K., Santillán, J., Shim, S. H., Prakapenka, V. B., Kunz, M., and Meng, Y. (2008). Effect of Fe on the equation of state of mantle silicate perovskite over 1 Mbar. Physics of the Earth and Planetary Interiors, 168:97–102.

Mao, Z., Wang, F., Lin, J.-F., Fu, S., Yang, J., Wu, X., Okuchi, T., Tomioka, N., Prakapenka, V. B., Xiao, Y., and Chow, P. (2017). Equation of state and hyperfine parameters of high-spin bridgmanite in the Earth's lower mantle by synchrotron X-ray diffraction and Mössbauer spectroscopy. American Mineralogist, 102:357–368.

Marquardt, H. and Thomson, A. R. (2020). Experimental elasticity of Earth's deep mantle. Nature Reviews Earth and Environment, 1:455–469.

Mashino, I., Murakami, M., Miyajima, N., and Petitgirard, S. (2020). Experimental evidence for silica-enriched Earth's lower mantle with ferrous iron dominant bridgmanite. Proceedings of the National Academy of Sciences of the United States of America, 117:27899–27905.

Matveev, S., O'Neill, H. S. C., Ballhaus, C., Taylor, W. R., and Green, D. H. (2001). Effect of silica activity on OH^- IR spectra of Olivine: Implications for low-aSiO_2 mantle metasomatism. Journal of Petrology, 42(4):721–729.

Meade, C., Reffner, J. A., and Ito, E. (1994). Synchrotron infrared absorbance measurements of hydrogen in $MgSiO_3$ perovskite. Science, 264:1558–1560.

Mierdel, K. and Keppler, H. (2004). The temperature dependence of water solubility in enstatite. Contributions to Mineralogy and Petrology, 148:305–311.

Mookherjee, M. and Tsuchiya, J. (2015). Elasticity of superhydrous phase, B, $Mg_{10}Si_3O_{14}(OH)_4$. Physics of the Earth and Planetary Interiors, 238:42–50.

Müller, E. W., Panitz, J. A., and Mclane, S. B. (1968). The Atom-Probe Field Ion Microscopes. The Review of Scientific Instruments, 39(1):83–86.

Murakami, M., Hirose, K., Yurimoto, H., Nakashima, S., and Takafuji, N. (2002). Water in Earth's Lower Mantle. Science, 295:1885–1887.

Murakami, M., Khan, A., Sossi, P., Ballmer, M., and Saha, P. (2024). Composition of Earth's Lower Mantle. (in press.).

Murakami, M., Ohishi, Y., Hirao, N., and Hirose, K. (2012). A perovskitic lower mantle inferred from high-pressure, high-temperature sound velocity data. Nature, 485:90–94.

Murakami, M., Sinogeikin, S. V., Hellwig, H., Bass, J. D., and Li, J. (2007). Sound velocity of $MgSiO_3$ perovskite to Mbar pressure. Earth and Planetary Science Letters, 256:47–54.

Myhill, R., Cottaar, S., Heister, T., Rose, I., Unterborn, C., Dannberg, J., and Gassmoeller, R. (2023). BurnMan – a Python toolkit for planetary geophysics, geochemistry and thermodynamics. Journal of Open Source Software, 8(87):5389.

Nakajima, Y., Frost, D. J., and Rubie, D. C. (2012). Ferrous iron partitioning between magnesium silicate perovskite and ferropericlase and the composition of perovskite in the Earth's lower mantle. Journal of Geophysical Research: Solid Earth, 117:B08201.

Navrotsky, A. (1999). A lesson from Ceramics. Science, 284(5421):1788–1789.

Nishio-Hamane, D., Seto, Y., Fujino, K., and Nagai, T. (2008). Effect of $FeAlO_3$ incorporation into $MgSiO_3$ on the bulk modulus of perovskite. Physics of the Earth and Planetary Interiors, 166:219–225.

Oganov, A. R., Brodholt, J. P., and Price, G. D. (2001). Ab initio elasticity and thermal equation of state of $MgSiO_3$ perovskite. Earth and Planetary Science Letters, 184:555–560.

Okuda, Y., Ohta, K., Sinmyo, R., Hirose, K., and Ohishi, Y. (2020). Anomalous compressibility in (Fe,Al)-bearing bridgmanite: implications for the spin state of iron. Physics and Chemistry of Minerals, 47:40:1–14.

Ono, S., Kikegawa, T., and Iizuka, T. (2004). The equation of state of orthorhombic perovskite in a peridotitic mantle composition to 80 GPa: Implications for chemical composition of the lower mantle. Physics of the Earth and Planetary Interiors, 145:9–17.

Pacalo, R. and Parise, J. (2000). Crystal structure of superhydrous B, a hydrous magnesium at silicate synthesized 1400°C and 20 GPa. American Mineralogist, 77:681–684.

Panero, W., Pigott, J. S., Reaman, D. M., Kabbes, J., and Liu, Z. (2014). Journal of Geophysical Research : Solid Earth. Journal of Geophysical Research, Solid Earth, 120:984–908.

Panero, W. R., Benedetti, L. R., and Jeanloz, R. (2003). Transport of water into the lower mantle: Role of stishovite. Journal of Geophysical Research: Solid Earth, 108(B1):2039.

Paterson, M. S. (1982). The determination of hydroxyl by infrared adsorption in quartz, silicate glasses and similar materials. Bulletin de Mineralogie, 105:20–29.

Prescher, C. and Prakapenka, V. B. (2015). DIOPTAS: A program for reduction of two-dimensional X-ray diffraction data and data exploration. High Pressure Research, 35(3):223–230.

Reddy, S. M., Saxey, D. W., Rickard, W. D., Fougerouse, D., Montalvo, S. D., Verberne, R., and van Riessen, A. (2020). Atom Probe Tomography: Development and Application to the Geosciences. Geostandards and Geoanalytical Research, 44(1):5–50.

Rosa, A. D., Sanchez-Valle, C., Wang, J., and Saikia, A. (2015). Elasticity of superhydrous phase B, seismic anomalies in cold slabs and implications for deep water transport. Physics of the Earth and Planetary Interiors, 243:30–43.

Saikia, A., Ballaran, T. B., and Frost, D. J. (2009). The effect of Fe and Al substitution on the compressibility of $MgSiO_3$-perovskite determined through single-crystal X-ray diffraction. Physics of the Earth and Planetary Interiors, 173:153–161.

Sakamaki, K., Takahashi, E., Nakajima, Y., Nishihara, Y., Funakoshi, K., Suzuki, T., and Fukai, Y. (2009). Melting phase relation of FeH_x up to 20 GPa: Implication for the temperature of the Earth's core. Physics of the Earth and Planetary Interiors, 174:192–201.

Sambridge, M., Gerald, J. F., Kovács, I., O'Neill, H. S. C., and Hermann, J. (2008). Quantitative absorbance spectroscopy with unpolarized light: Part I. Physical and mathematical development. American Mineralogist, 93:751–764.

Schmandt, B., Jacobsen, S. D., Becker, T. W., Liu, Z., and Dueker, K. G. (2014). Dehydration melting at the top of the lower mantle. Science, 344(6189):12265–1268.

Scott Smith, B. H., Danchin, R. V., Harris, J. W., and Stracke, K. J. (1984). Kimberlites near Orroroo, South Australia. In Kornprobst, J., editor, Kimberlites I: Kimberlites and related rocks, pages 121–142. Elsevier Science Publishers B.V.

Seto, Y., Nishio-Hamane, D., Nagai, T., and Sata, N. (2010). Development of a Software Suite on X-ray Diffraction Experiments. The Review of High Pressure Science and Technology, 20(3):269–276.

Shannon, R. D. and Prewitt, C. T. (1969). Effective ionic radii in oxides and fluorides. Acta Crystallographica Section B Structural Crystallography and Crystal Chemistry, B25:925–946.

Shen, G., Wang, Y., Dewaele, A., Wu, C., Fratanduono, D. E., Eggert, J., Klotz, S., Dziubek, K. F., Loubeyre, P., Fat'yanov, O. V., Asimow, P. D., Mashimo, T., and Wentzcovitch, R. M. (2020). Toward an international practical pressure scale: A proposal for an IPPS ruby gauge (IPPS-Ruby2020). High Pressure Research, 40(3):299–314.

Shukla, G., Cococcioni, M., and Wentzcovitch, R. M. (2016). Thermoelasticity of Fe^{3+}- and Al-bearing bridgmanite: Effects of iron spin crossover. Geophysical Research Letters, 43:5661–5670.

Sinelnikov, Y. D., Chen, G., Neuville, D. R., Vaughan, M. T., and Liebermann, R. C. (1998). Ultrasonic Shear Wave Velocities of $MgSiO_3$ Perovskite at 8 GPa and 800 K and Lower Mantle Composition. Science, 281:677–679.

Sinogeikin, S. V., Zhang, J., and Bass, J. D. (2004). Elasticity of single crystal and polycrystalline $MgSiO_3$ perovskite by Brillouin spectroscopy. Geophysical Research Letters, 31:1–5.

Smyth, J. R., Holl, C. M., Frost, D. J., and Jacobsen, S. D. (2004). High pressure crystal chemistry of hydrous ringwoodite and water in the Earth's interior. Physics of the Earth and Planetary Interiors, 143-144:271–278.

Smyth, J. R., Holl, C. M., Frost, D. J., Jacobsen, S. D., Langenhorst, F., and Mccammon, C. A. (2003). Structural systematics of hydrous ringwoodite and water in Earth's interior. American Mineralogist, 88:1402–1407.

Stachel, T., Harris, J. W., Brey, G. P., and Joswig, W. (2000). Kankan diamonds (Guinea) II: Lower mantle inclusion parageneses. Contributions to Mineralogy and Petrology, 140:16–27.

Stebbins, J. F. and Kroeker, S. (2001). The mechanism of solution of aluminum in $MgSiO_3$ perovskite. Geophysical Research Letters, 28(4):615–618.

Stixrude, L. and Lithgow-Bertelloni, C. (2011). Thermodynamics of mantle minerals - II. Phase equilibria. Geophysical Journal International, 184(3):1180–1213.

Tange, Y., Takahashi, E., Nishihara, Y., Funakoshi, K. I., and Sata, N. (2009). Phase relations in the system MgO-FeO-SiO_2 to 50 GPa and 2000°C: An application of experimental techniques using multianvil apparatus with sintered diamond anvils. Journal of Geophysical Research: Solid Earth, 114:B02214.

Tappert, R., Foden, J., Stachel, T., Muehlenbachs, K., Tappert, M., and Wills, K. (2009). Deep mantle diamonds from South Australia: A record of Pacific subduction at the Gondwanan margin. Geology, 37(1):43–46.

Tschauner, O., Chi, M., Beckett, J. R., Prescher, C., Prakapenka, V. B., and Rossman, G. R. (2014). Discovery of bridgmanite, the most abundant mineral in Earth, in a shocked meteorite. Science, 346(6213):1100–1102.

Vanpeteghem, C. B., Angel, R. J., Ross, N. L., Jacobsen, S. D., Dobson, D. P., Litasov, K. D., and Ohtani, E. (2006). Al, Fe substitution in the $MgSiO_3$ perovskite structure: A single-crystal X-ray diffraction study. Physics of the Earth and Planetary Interiors, 155:96–103.

Walker, A. M., Demouchy, S., and Wright, K. (2006). Computer modelling of the energies and vibrational properties of hydroxyl groups in α- and β-Mg_2SiO_4. European Journal of Mineralogy, 18:529–543.

Walter, M. J., Kubo, A., Yoshino, T., Brodholt, J., Koga, K. T., and Ohishi, Y. (2004). Phase relations and equation-of-state of aluminous Mg-silicate perovskite and implications for Earth's lower mantle. Earth and Planetary Science Letters, 222(2):501–516.

Walter, M. J., Trønnes, R. G., Armstrong, L. S., Lord, O. T., Caldwell, W. A., and Clark, S. M. (2006). Subsolidus phase relations and perovskite compressibility in the system $MgO-AlO_{1.5}-SiO_2$ with implications for Earth's lower mantle. Earth and Planetary Science Letters, 248:77–89.

Wang, D., Mookherjee, M., Xu, Y., and Karato, S.-i. (2006). The effect of water on the electrical conductivity of olivine. Nature, 443:977–980.

Wang, J., Sinogeikin, S. V., Inoue, T., and Bass, J. D. (2003). Elastic properties of hydrous ringwoodite at high-pressure conditions. American Mineralogist, 88:1608–1611.

Wentzcovitch, R. M., Karki, B. B., Cococcioni, M., and de Gironcoli, S. (2004). Thermoelastic Properties of $MgSiO_3$-Perovskite: Insights on the Nature of the Earth's Lower Mantle. Physical Review Letters, 92(1):018501.

Wilding, M., Harte, B., and Harris, J. (1991). Evidence for a Deep Origin for Sao Luiz Diamonds. In Fifth International Kimberlite Conference Extended Abstracts, pages 456–458. Araxa.

Wood, B. J. (2000). Phase transformations and partitioning relations in peridotite under lower mantle conditions. Earth and Planetary Science Letters, 174:341–354.

Wood, B. J. and Rubie, D. C. (1996). The effect of alumina on phase transformations at the 660-kilometer discontinuity from Fe-Mg partitioning experiments. Science, 273:1522–1524.

Xu, C., Gréaux, S., Inoue, T., Noda, M., Gao, J., and Li, Y. (2022). Sound Velocities of Superhydrous Phase B up to 21 GPa and 900 K. Geophysical Research Letters, 49.

Xu, Y., McCammon, C., and Poe, B. T. (1998). The effect of alumina on the electrical conductivity of silicate perovskite. Science, 282:922–924.

Yang, Y. N., Du, Z., Lu, W., Qi, Y., Zhang, Y. Q., Zhang, W. F., and Zhang, P. F. (2023). NanoSIMS analysis of water content in bridgmanite at the micron scale: An experimental approach to probe water in Earth's deep mantle. Frontiers in Chemistry, 11.

Ye, Y., Brown, D. A., Smyth, J. R., Panero, W. R., Jacobsen, S. D., Chang, Y. Y., Townsend, J. P., Thomas, S. M., Hauri, E. H., Dera, P., and Frost, D. J. (2012). Compressibility and thermal expansion of hydrous ringwoodite with 2.5(3) wt% H_2O. American Mineralogist, 97:573–582.

Yeganeh-Haeri, A. (1994). Synthesis and re-investigation of the elastic properties of single-crystal magnesium silicate perovskite. Physics of the Earth and Planetary Interiors, 87:111–121.

Yoshino, T. and Jaseem, V. (2018). Fluorine solubility in bridgmanite: A potential fluorine reservoir in the Earth's mantle. Earth and Planetary Science Letters, 504:106–114.

Yusa, H., Inoue, T., and Ohishi, Y. (2000). Isothermal compressibility of hydrous ringwoodite and its relation to the mantle discontinuities. Geophysical Research Letters, 27(3):413–416.

Zedgenizov, D. A., Shatsky, V. S., Panin, A. V., Evtushenko, O. V., Ragozin, A. L., and Kagi, H. (2015). Evidence for phase transitions in mineral inclusions in superdeep diamonds of the Sao Luiz deposit (Brazil). Russian Geology and Geophysics, 56:296–305.

Chapter 3

The Stishovite to $CaCl_2$-type SiO_2 Phase Transition Revisited by *in-situ* High-Pressure Brillouin Scattering Spectroscopy

This chapter represents work that was started during my master thesis at ETH Zürich, and was continued as a side project throughout the doctorate. During the master thesis, a first sample was prepared and measured using Brillouin spectroscopy. This sample was measured over a much wider range of pressures than what is shown in this chapter. However, at the end of the master thesis, it became clear that the observed elastic softening at the phase transition from stishovite to $CaCl_2$-type SiO_2 was the most interesting observation from these measurements.

When trying to write a manuscript about these observations at the beginning of this doctorate, the evidence to support the idea that differential stresses in the sample chamber were low seemed insufficient. It was therefore decided that a new cell with a similar sample would be loaded with a different pressure medium to confirm the reproducibility of the measurements and the method used for differential stress calculations. The sample preparation for this included learning how to use a Focused Ion Beam to meticulously cut the sample into pieces, and learning to use a gas loading system in

order to load the Ne pressure medium. Gas loading a DAC is challenging and several attempts had to be made before being successful. A manual about the procedure was written to help future users of this system. Thereafter, Brillouin spectroscopy was performed on the sample, but due to the high sensitivity of the BX90 DAC used for gas loading, it was not possible to increase the pressure in small enough steps to observe and constrain the softening at the phase transition. Despite this, a good XRD spectrum of the gas-loaded sample was measured in February 2023 and the stress calculation method could thereby be verified.

Preliminary stress calculations were already attempted in the master thesis, but these results were revised and recalculated during the doctorate. The presented manuscript and the figures within it were prepared within the last four years and due to the significant amount of work performed during the doctorate on this manuscript, it was included as a chapter in this thesis. This work was also presented at the AGU 2023 Fall Meeting in the form of a poster.

The Stishovite to $CaCl_2$-type SiO_2 Phase Transition revisitited by in-situ high-pressure Brillouin Scattering Spectroscopy

Thomas de Selva-Dewint[1], Motohiko Murakami[1]
[1]Department of Earth Sciences, ETH Zürich, Sonneggstrasse 5, 8092 Zurich, Switzerland

SiO_2 is an important phase in the Earth's subduction slabs, and its phase transitions therefore play a significant role when trying to understand seismic anomalies in Earth's mantle. Acoustic velocities of SiO_2 were measured using Brillouin scattering spectroscopy between 20 and 55 GPa at ambient temperature to investigate the stishovite to $CaCl_2$-type SiO_2 phase transition. A significant drop in shear wave velocities caused by the phase transition was observed at 30 GPa, suggesting a transition depth of 1000–1200 km. Additionally, different pressure media, and synchrotron X-ray diffraction measurements were used to discuss the possible influence of differential stress on the phase transition.

1 Introduction

Seismic stations have been measuring numerous unexplained seismic scatterers in the lower mantle, especially around subduction zones. The identification of these scatterers is generally based on the detection of short-period ($\sim$1 s) seismic waves, mostly S-to-P-wave conversions, which provide the best depth resolution due to the sharp velocity contrast between the S and P waves (Kaneshima, 2016). These body waves generally

have a wavelength of 10 km or less, which allows for small-scale scatterers of a similar size to be resolved. An overview of scatterers observed around subduction zones in the lower mantle by seismological studies can be found in Fig. 1. The scatterers represented in Fig. 1 were observed around known subduction zones below western South America (Kaneshima and Helffrich, 2009; Kaneshima et al., 2010; Korenaga, 2014; Kaneshima, 2019), Alaska (Kaneshima, 2019), Japan (Kawakatsu and Niu, 1994; Bagley et al., 2013; A. Deuss, J. Andrews, 2013; Li and Yuen, 2014; Kaneshima, 2019), the Solomon islands (Kaneshima, 2019; Yang and He, 2015), Indonesia (Kawakatsu and Niu, 1994; Vinnik et al., 1998, 2001; Vanacore et al., 2006; Yang and He, 2015; Kaneshima, 2019), the Philippines (Yang and Wu, 2014), Izu-Bonin-Mariana (Kaneshima and Helffrich, 1998, 1999, 2003; Kaneshima et al., 2010; Kaneshima, 2019; Castle and Creager, 1999; Vinnik et al., 1998; Niu et al., 2003; Bentham and Rost, 2014), Kuril-Ochotsk (Peterson et al., 1993; Kaneshima et al., 2010; Kaneshima, 2019), Tonga-Fiji (Kawakatsu and Niu, 1994; Courtier and Revenaugh, 2008; Kaneshima et al., 2010; Kaneshima, 2013; A. Deuss, J. Andrews, 2013; Yang and He, 2015; Kaneshima, 2018; Yuan et al., 2023) and the Himalaya—Southeast Asia (where the Thetys ocean closed Rochira et al., 2022)). As visible from Fig. 1, the abundance of scatterers lowers towards higher depths. About half of the scatterers in the lower mantle are observed at depths shallower than 1000 km. Many scatterers are still found in the depth range 1000–1200 km, but their abundance considerably drops after that, with the exception of a slight increase in abundance around 1500 km.

It is important to try to find an explanation for the scatterers observed at varying depths in the lower mantle and represented in Fig. 1. Fluctuations in temperature in the mantle are known to affect seismic wave velocities, but the scatterers represented in here are too small-scale and sharp to be caused by temperature changes. Tomography, which can map $\geq$1000–km scale heterogeneities through the combined detection of long-period

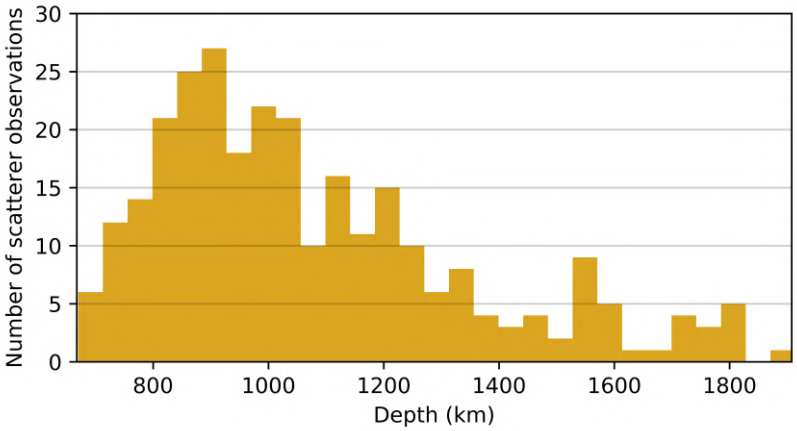

Figure 1: Cumulative histogram showing the depth distribution of seismic scatterers found in the lower mantle around subduction zones.

normal modes, surface waves and short-period body waves, is a more suited method for detecting temperature changes (Kaminsky, 2017). Thus, other explanations have to be investigated. One likely candidate to explain some of these scatterers is a phase transition known to take place in SiO_2, from stishovite to $CaCl_2$-type SiO_2, which has been shown to cause a drastic drop in sound wave velocity. SiO_2 is also thought be make up 10–25 wt% of subducting slabs and has the biggest density contrast relative to the rest of the mantle, therefore playing an important role. However, varying accounts of the pressure at which the transition takes place have made it difficult to agree on the exact phase transition depth. This study aims to further resolve this problem.

The stishovite to $CaCl_2$-type SiO_2 phase transition is a pseudo-proper ferroelastic or second order phase transition (Malcherek, 2015). Such transitions generally occur at a critical point of hysteresis by increasing the temperature or pressure in a system. The phase transition discussed here is pressure-induced. At the point of hysteresis, the crystal changes its orientation mechanically due to the external stress applied (Salje, 2012). For the stishovite to $CaCl_2$-type SiO_2 phase transition, the atoms rearrange themselves from

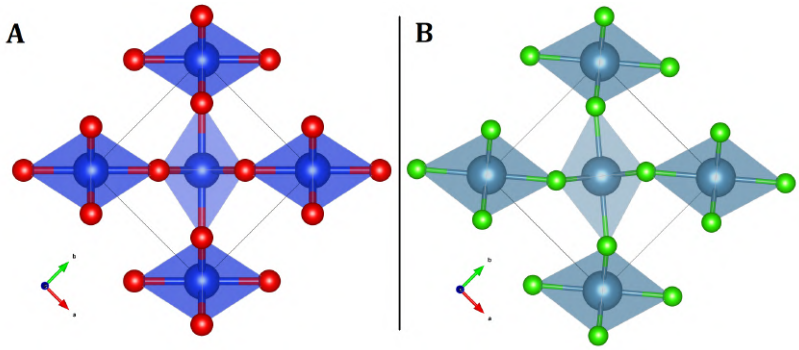

Figure 2: A: The tetragonal rutile-type stishovite crystal structure (Yamanaka et al., 2002). B: The orthorhombic $CaCl_2$-type SiO_2 crystal structure (Howard et al., 2005). The individual Si-octahedra are oriented along the c-axis, in order to show how the there is slight difference in orientation between the two structures, corresponding to a rotation around the c-axis that happens at the phase transition. Structures are represented using the VESTA software (?)

tetragonal ($P4_2/mnm$ space group) to orthorhombic ($Pnnm$ space group) symmetry by rotating slightly around the crystallographic c-axis (Togo et al., 2008), as visible in Fig. 2. Leading up to the point of hysteresis, the phonon frequency (indicating how fast the atoms in the crystal lattice vibrate) decreases, until it ultimately reaches zero at the transition, as if the atoms momentarily freeze for the lattice orientation to be changed (Dove, 1993). After the phase transition, the phonon frequency will increase again. The phonon frequency of a material is directly proportional to its phonon velocity or acoustic velocity, which is equivalent to the seismic wave velocity obtained from seismometers. This means that the acoustic velocities will also go to zero at the phase transition. This phenomenon is called "elastic softening" and is expressed as a drop in seismic velocities, which could explain observed scatterers in the lower mantle mentioned earlier.

The stishovite to $CaCl_2$-type SiO_2 phase transition was first discovered in 1989, using X-ray diffraction (XRD) measurements (Tsuchida and Yagi, 1989). X-ray diffraction has since remained the most common method to measure the phase transition, and reported

transition pressures vary between 40–60 GPa when using this method, as shown in Fig. 3. (Kingma et al., 1996; Dubrovinsky et al., 1997; Andrault et al., 1998; Hemley et al., 2000; Ono et al., 2002; Andrault et al., 2003; Nomura et al., 2010; Yamazaki et al., 2014; Fischer et al., 2018; Buchen et al., 2018; Wang et al., 2023). Studies measuring XRD on Al- or H-bearing SiO_2 however, have reported lower phase transition pressures. Bolfan-Casanova et al. (2009) measured a sample containing ∼4 wt.% Al_2O_3 and reported a transition pressure of 23 GPa and ambient temperature. Nisr et al. (2017a) investigated an Al-free sample with 2.3 wt.% H_2O and determined that the transition takes place at ∼28 GPa. The identification of the phase transition with XRD relies on the splitting of both the 101 and 211 peaks into two 011 and 101, and 121 and 211 peaks respectively (Buchen et al., 2018).

Three theoretical ab-intitio studies (Karki et al., 1997; Carpenter et al., 2000; Yang and Wu, 2014) predicted an acoustic velocity drop due to this phase transition somewhere between 40 and 50 GPa. An ab-initio study by Umemoto et al. (2016) suggested that Al alone could not be responsible for a decrease in the phase transition pressure, and that the presence of H is needed. This however, seems to go somewhat against the experimental results of Bolfan-Casanova et al. (2009).

Vibrational spectroscopy methods, i.e. Raman and Brillouin scattering spectroscopy, can also be used to determine the phase transition pressure, due to its ability to measure the change in elasticity that happens at the transition. Kingma et al. (1995) was the first to use the shift in the optic modes measured with Raman spectroscopy and caused by the phase transition to determine the pressure at which it takes place. A transition pressure of 50 GPa was reported. A few more studies have used Raman spectroscopy to detect the phase transition since. Lakshtanov et al. (2007) used a SiO_2 sample with 6 wt% Al_2O_3 and 0.24 wt% H_2O and observed the phase transition at ∼24 GPa. Nisr et al. (2017b)

measured an Al-free sample containing 3.2 wt.% H_2O and found the phase transition at ∼23 GPa. Zhang et al. (2022) reported to a phase transition at 21.1 GPa in a sample containing 1.34 mol% Al and 0.55 mol% H, and at 16.1 GPa in a sample containing 2.1 mol% Al and 0.59 mol% H. Criniti et al. (2023) recently reported the phase transition at 16 GPa in a sample containing 1.73 mol% Al and 0.60 mol% H.

Four studies have used Brillouin scattering spectroscopy to measure the phase transition between stishovite and $CaCl_2$-type SiO_2. The phase transition is expressed as a drop in experimentally measured body wave velocities. Lakshtanov et al. (2007) measured the same sample as for their Raman measurements with Brillouin, and reports much lower absolute velocity values compared to the theoretical predictions (Karki et al., 1997; Carpenter et al., 2000). This observation led to the idea that adding Al_2O_3 or H_2O causes an overall velocity decrease. A velocity drop of ∼13% at the phase transition was measured, at ∼23 GPa. Asahara et al. (2013) used a pure SiO_2 sample and observed a shear wave velocity drop of ∼3% slightly above 20 GPa. The drop at lower pressures compared to the previous theoretical studies was attributed to non-hydrostatic stress conditions in the sample chamber. Jiang et al. (2009) performed Brillouin measurements from 1 bar to 22 GPa along the approximate direction of the [1 1 0] plane of a single-crystal stishovite sample. The phase transition itself was not observed in that pressure range, but a gradual decrease of 11% in the shear wave velocity from 1 bar to 22 GPa is reported. Lastly, a single-crystal study by Zhang et al. (2021) observed the phase transition at 55 GPa by using a combination of Brillouin spectroscopy and Impulsive Stimulated Light Spectroscopy.

Despite the slight discrepancies between the results from measurements on Al- or H-bearing SiO_2, it becomes clear when looking at Fig. 3 that the presence of H_2O and Al_2O_3 lowers the transition pressure between stishovite and $CaCl_2$-type SiO_2 (Lakshtanov

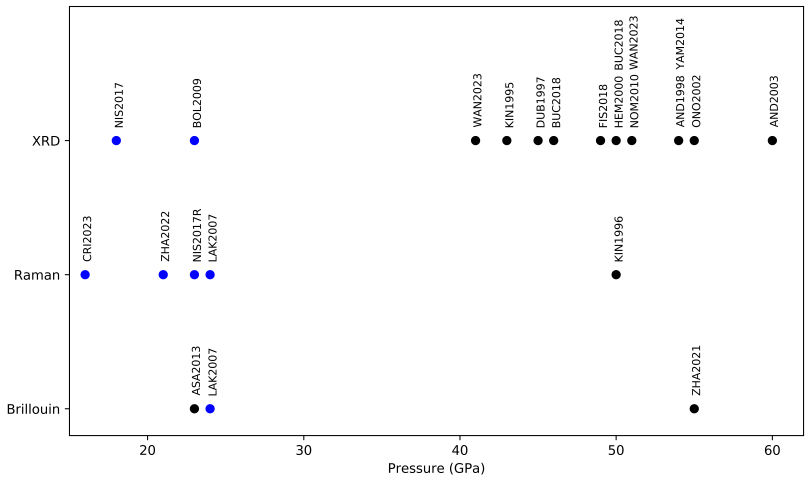

Figure 3: Representation of the pressure reported by previous studies for the stishovite to $CaCl_2$–type SiO_2 phase transition at ambient temperature. Studies are categorized by method. Short forms are the following: KIN1995 for Kingma et al. (1995), KIN1996 for Kingma et al. (1996), DUB1997 for Dubrovinsky et al. (1997), AND1998 for Andrault et al. (1998), HEM2000 for Hemley et al. (2000), ONO2002 for Ono et al. (2002), AND2003 for Andrault et al. (2003), LAK2007 for Lakshtanov et al. (2007), BOL2009 for Bolfan-Casanova et al. (2009), NOM2010 for Nomura et al. (2010), ASA213 for Asahara et al. (2013), YAM2014 for Yamazaki et al. (2014), NIS for Nisr et al. (2017a), NIS2017R for Nisr et al. (2017b), FIS2018 for Fischer et al. (2018), BUC2018 for Buchen et al. (2018), ZHA2021 for Zhang et al. (2021), ZHA2022 for Zhang et al. (2022), WAN2023 for Wang et al. (2023) and CRI2023 for Criniti et al. (2023).

et al., 2007; Bolfan-Casanova et al., 2009; Nisr et al., 2017a,b; Zhang et al., 2022; Criniti et al., 2023). However, the large discrepancy in Brillouin spectroscopy results on pure SiO_2, between the results from Asahara et al. (2013) and Zhang et al. (2021), motivated the undertaking of this study, in which SiO_2 was measured using Brillouin spectroscopy between 20 GPa and 55 GPa.

2 Methods

In order to experimentally achieve the pressure conditions necessary for the phase transition, a Diamond Anvil Cell experimental setup (henceforth DAC) was used, in which two oppositely positioned diamonds are screwed closer to each other to pressurize the sample uniaxially. Two cells were loaded for the purpose of this study. The first one contained a stishovite powder, synthesized using a large volume press at 11 GPa and 1200℃, together with a KCl pressure medium. The second was loaded with a polycrystalline SiO_2 sample, along with a Ne pressure medium. Both samples were surrounded by a rhenium gasket, making up the sample chamber.

The aim of this study is to measure the acoustic velocities in SiO_2 as pressure gets slowly increases at ambient temperature, using Brillouin scattering spectroscopy. The transparency of diamonds and very small thickness of the sample ($\sim$30 μm) makes it possible to shoot a monochromatic green laser beam (532 nm) through the sample material and determine how the two interfere by measuring the laser beam with interferometer after exit (Calas and Hawthorne, 1988). When the laser light passes through the sample, they will thermally excite its atoms, making them vibrate at a certain frequency as 'phonons', meaning that they can be described as waves (Speziale et al., 2014). Some of this laser light gets scattered inelastically when it interacts with the sample material, entailing either a loss or gain of energy, forming two sets of 'inelastically' scattered laser light beams called Stokes and anti-Stokes scattering. These two have a frequency of $(\omega + \omega_0)$ and $(\omega - \omega_0)$ respectively, where ω is the frequency of the incoming laser light and ω_0 the eigenfrequency of the the sample's phonons. These eigenfrequencies are detected by the interferometer and represented as a shift compared to the laser frequency, ranging between 10^6 and 10^{10} Hz.

These observed frequency shifts can be directly related to the phonon velocity of the sample at the conditions of the experiment through equation 1. Here, V stands for the phonon velocity, $\Delta\omega$ for the frequency shift, λ for the laser wavelength, and θ for the scattering angle. The scattering angle is fixed to $\sim 50°$ in the spectroscopic setup used for this study. The phonon velocity corresponds to the acoustic velocity of the material measured at the same pressure and temperature in the mantle.

$$V = \frac{\Delta\omega\lambda}{2sin(\frac{\theta}{2})} \tag{1}$$

In order to estimate the pressure of the sample while doing experiments, another vibrational spectroscopic method was used, Raman spectroscopy. In Raman spectroscopy, the observed Stokes and anti-Stokes frequency shift are characteristic for the measured material at specific conditions, and range between 10^{12} to 10^{14} Hz (Calas and Hawthorne, 1988). For pressure determination, the method developed by Akahama and Kawamura (2006, 2010), in which the high frequency edge of the first-order Raman mode of diamond has been calibrated with pressure, was used.

3 Results

Two examples of the raw Brillouin scattering data can be found in Fig. 4. Brillouin measurements on the DAC loaded wiith Ne failed, which is why only the measurements on the cell containing KCl are shown here. As visible in Fig. 4 B, peaks representing the KCl pressure medium were also sometimes observed in the spectrum. This is most likely due to the pressure medium being slightly thicker in some places of the sample chamber. The results of measuring acoustic velocities in this cell are illustrated in Fig. 6. The data shows a clear drop of $\sim 6\%$ in shear velocity at ~ 30 GPa, which corresponds to the elastic softening expected for this phase transition. Previous Brillouin scattering

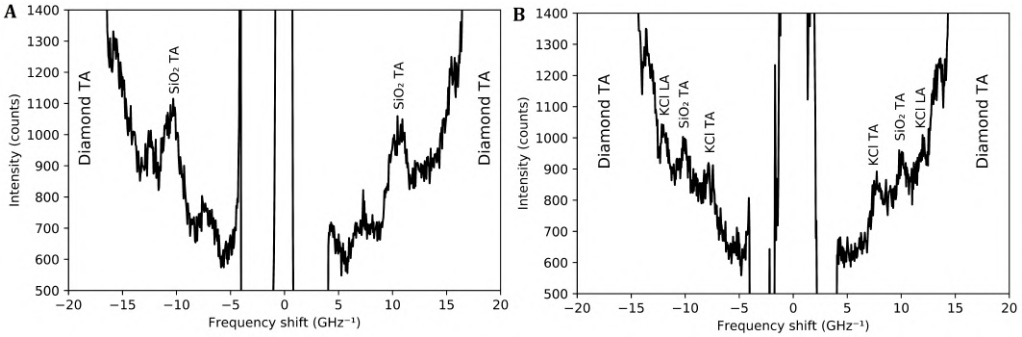

Figure 4: Examples of the raw Brillouin spectra, at 26.88 GPa (A) and 30.32 GPa (B). TA stands for transverse acoustic modes (V_S), and LA for longitudinal acoustic wave (V_P).

measurements on pure SiO_2 are also represented in Fig. 6. All measurements are at ambient temperature. As the main purpose of this study was to investigate the trend of the acoustic wave velocities in SiO_2, and not their precise absolute values, angular dispersion measurements at every pressure were not performed. The angular dispersion was only investigated at ∼35 GPa and determined to be ∼5,5%, as visible in Fig. 5. Based on Fig. 5, in which the average shear velocity is 3% higher than the velocity at 90° used throughout this study, it can be assumed that the entire trend of measurements at 90° represented in Fig. 6 is lower than what the average would be. This does not affect the phase transition pressure or magnitude though.

Besides Brillouin scattering, two X-ray diffraction spectra were measured. The first was collected at the Swiss Light Source of the Paul Scherrer Insitute, at the ADDAMS beamline equipped with a solid-state silicon microstrip detector (Willmott et al., 2013), at ∼30 GPa in the DAC loaded with KCl and is represented in Fig. 7. The second was measured on the DAC loaded with a Ne pressure medium at ∼39 GPa, at the ID27 high pressure beamline of the European Synchrotron facility (ESRF), equipped with a EIGER2 X CdTe 9M detector. A CeO_2 standard was used to calibrate the detector

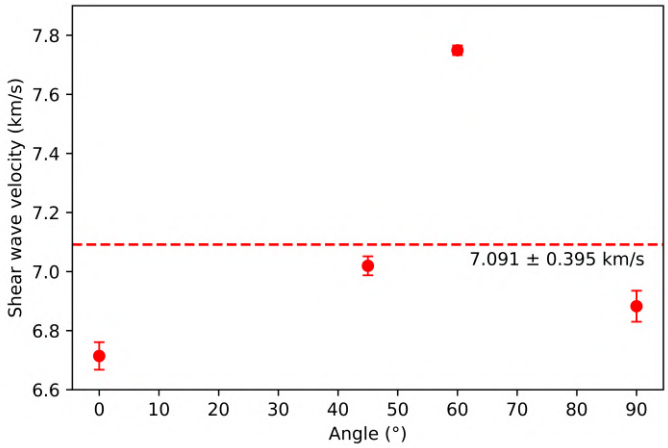

Figure 5: Angular dispersion of the measured sample at ∼35 GPa. The average V_s based on these measurements is 7.09 ± 0.40 km/s, which is ∼3% higher than the velocity at the 90° angle used throughout this study.

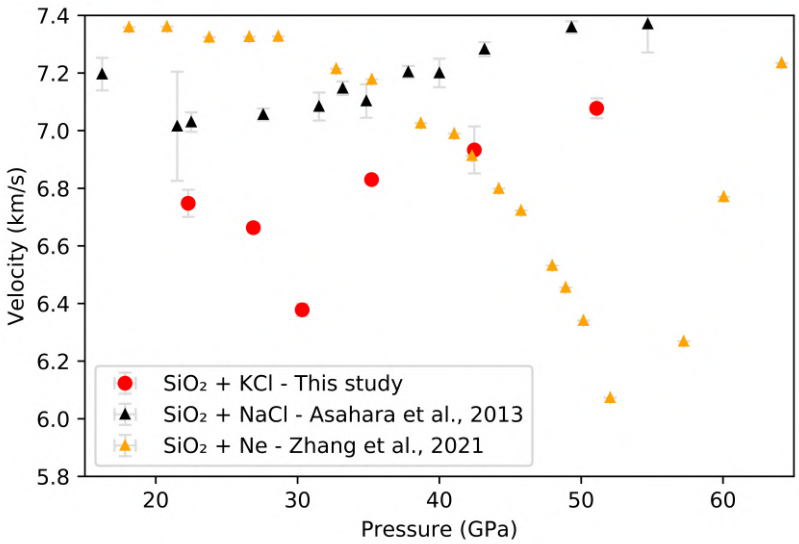

Figure 6: Brillouin spectroscopy results at ambient temperatures of SiO_2 loaded with a KCl pressure medium. Previous Brillouin spectroscopy measurements on pure SiO_2 by Asahara et al. (2013) and Zhang et al. (2021) are also represented.

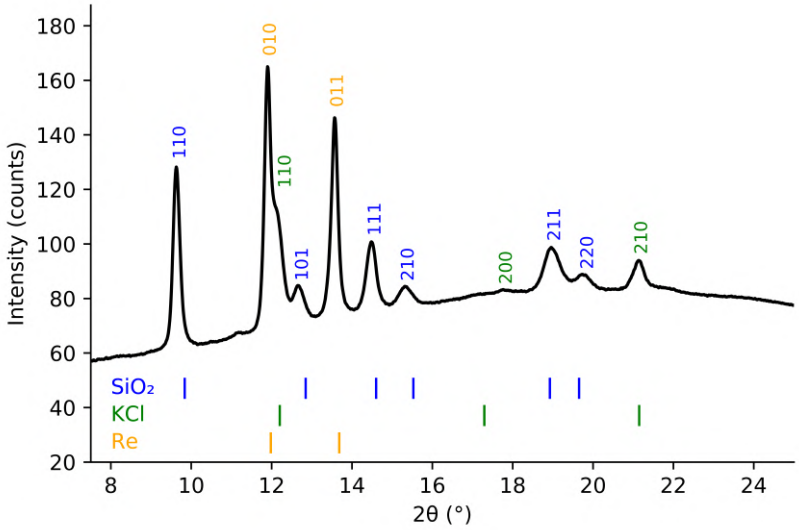

Figure 7: XRD spectrum at 30GPa of SiO_2, loaded with a KCl pressure medium.

distance, centering and tilting. The X-ray source at the Swiss Light Source had a larger beam size (130.0 x 40.0 µm, versus 2.0 x 2.0 µm for the ID27 beamline), which explains why some rhenium peaks are observed in this spectrum from the surrounding gasket. The 2D diffraction pattern was converted to a 1D profile, refined and background corrected using the Dioptas software (Prescher and Prakapenka, 2015). For peak fitting and indexing, the PDIndexer software was used (Seto et al., 2010).

4 Discussion

4.1 The phase transition pressure

The Brillouin scattering measurements clearly show a drop in the shear wave velocity at ∼30 GPa, as shown in Fig. 6. This pressure is lower than the 40–60 GPa range usually reported in previous studies on pure SiO_2, in which the phase transition is observed using peak splitting in the XRD spectra (see Fig. 3. When looking at the XRD spectra in

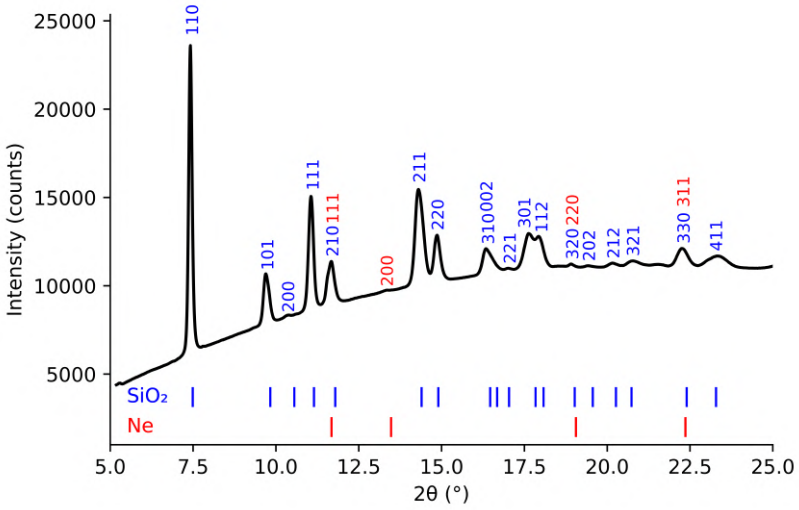

Figure 8: XRD spectrum at 39GPa of SiO_2, loaded with a Ne pressure medium.

Figs. 7 & 8, no peak splitting of the 101 and 211 peaks is discernible. This can be explained by the fact that the ability observe the peak splitting with XRD is actually delayed with respect to the pressure at which the phase transition takes place. This is most likely due to the fact that the atomic displacements and volume change in crystal lattice at the phase transition are so small. The transition pressure therefore has to be extrapolated back when using XRD measurements. This problem is not present with Brillouin measurements, where the minimum in the observed velocity drop corresponds exactly to the transition pressure and can thus be determined directly, thereby making it a more suitable to detect the transition.

Compared to the previous Brillouin studies on SiO_2, the phase transition pressure measured here s higher than the one measured by Lakshtanov et al. (2007) and Asahara et al. (2013), and lower than the one measured by Zhang et al. (2021). The lower phase transition pressures measured in Lakshtanov et al. (2007) and Asahara et al. (2013) can be attributed to the difference in composition and strong differential stresses in the sample

chamber respectively. The most recent Brillouin study by Zhang et al. (2021), in which a single crystal sample was measured with a Ne pressure medium, observed the transition at 55 GPa. The stress conditions in the sample chamber were not determined in this study. The discrepancy between the results presented here and the study by Zhang et al. (2021) is difficult to explain, but could possibly be caused by a difference in mechanical behavior between single crystal and polycrystalline materials. It also has to be noted that the bulk shear wave velocities reported by Zhang et al. (2021) are calculated by combining measurements at different orientations on V_S with Brillouin spectroscopy and V_P with Impulsive Stimulated Light Scattering. The combination of these factors could possibly lead to the observed difference.

4.2 Calculating the differential stress

Previous authors studying this phase transition have suggested that the pressure at which it takes place might decrease with increasing differential stress in the sample chamber (Asahara et al., 2013; Wang et al., 2023). The differential stress in a DAC can be calculated by estimating how much the sample peak locations in the XRD spectrum deviate from what their theoretically calculated positions should be at hydrostatic conditions at the same pressure and temperature. This method is based on lattice strain theory (Singh et al., 1998), in which all independent elastic constants of the material and their pressure derivatives need to be known in order to calculate the stress. Usually the peaks caused by the pressure medium are utilized, i.e. KCl or Ne in this study, because these materials are cubic and therefore only have three independent elastic constants: C_{11}, C_{12} and C_{44}. Once the elastic constants are calculated at the right pressure, they can by converted to elastic stiffnesses S_{11}, S_{12} and S_{44} (Nye, 1957). These can then be used to calculate a bulk elastic stiffness by using the formula $S = S_{11} - S_{12} - S_{44}/2$. This parameter can

then be related to the differential stress in the sample chamber through the linear Eq. 2 from Singh and Kenichi (2001). In this equation, $a_m(hkl)$ represents the actual measured peak position for every hkl plane, a is the peak position after fitting the entire spectrum to the theoretically predicted positions, θ half of the angle between the incident and the diffracted beam, and t the differential stress. M_0 and M_1 are the intercept and slope of the equation respectively. According to Singh and Kenichi (2001), $M_0 \approx a$ and weight factor $\alpha \approx 1$, meaning that $St \approx -3M_1/M_0$. Thus, in order to calculate the differential stress t, M_0 and M_1 have to be calculated. For this, the equation is plotted in a so-called gamma plot, illustrated in Fig. 9 for the two cells measured in this study.

$$a_m(hkl) = M_0 + M_1[3(1 - 3cos^2\theta)\Gamma(hkl)] \tag{2}$$

$$\begin{aligned}
\text{with } M_0 &= a\{1 + (\frac{\alpha t}{3})(1 - 3cos^2\theta)[(S_{11} - S_{12}) - (1 - \alpha^{-1})(2G_v)^{-1}]\} \\
M_1 &= -a(\frac{\alpha t S}{3}) \\
\Gamma(hkl) &= (h^2k^2 + k^2l^2 + l^2h^2)/(h^2 + k^2 + l^2)^2 \\
(2G_V)^{-1} &= 5(S_{11} - S_{12})S_{44}/2[3(S_{11} - S_{12}) + S_{44}]
\end{aligned}$$

The XRD peaks of KCl and Ne were fitted in PDIndexer to determine their positions (Seto et al., 2010). The 2θ position of each peak, corresponding to an hkl plane, was converted to a d-spacing by using Bragg's equation $d = \lambda/2sin\theta$, in which λ is the wavelength of the X-ray source used for the measurement in ångström (Å). The d-spacings were then converted to the lattice parameter a for every respective hkl plane, by using the relation $a^2 = d_{hkl}^2(h^2 + k^2 + l^2)$. The a lattice parameter is calculated for both the observed peak position in the spectrum, a_m, and the fitted position, a. With these values, the y-axis of the gamma plot in Fig. 9 can be created, where the x-axis corresponds to $3(1 - sin^2\theta)\Gamma(hkl)$. Once all hkl planes have been plotted in Fig. 9, a linear trendline can

be drawn through them. From the slope M_1 and the intercept M_0 of this trendline, the St-value for the sample can be calculated. Lastly, the differential stress t can be calculated by dividing St with the elastic stiffness S of the material. The resulting differential stresses calculated fromm this method are 0.455 GPa for the stishovite cell loaded with KCl, and 5.327 GPa for the stishovite cell loaded with Ne, as visible in Fig. 9.

In order to determine the elastic stiffness S of both pressure media, the elastic constants for KCl and Ne at ambient conditions were taken from Every and McCurdy (1992). To extrapolate those values to the pressures at which the XRD spectra were measured, pressure derivatives of the elastic constants from Sirdeshmukh et al. (2001) and Shimizu et al. (2005) were used for KCl and Ne respectively. The elastic constants for KCl are not entirely accurate, as these were measured at ambient conditions where the B1–phase of KCl is stable. At a pressure of ∼30 GPa, KCl would be present in the form of the B2–phase, for which no data on the elastic constants exists. Based on NaCl data however, where the same phase transition takes place and elastic constants are known for both, using the B1 elastic constants can be assumed to overestimate the differential stress. According to Liu et al. (2010), C_{11} of B2 NaCl decreases compared to B1 NaCl, whereas both C_{12} and C_{44} increase across the phase transition. This would mean that S_{11} increases, while S_{12} and S_{44} decrease, so S has to increase. Since St remains a constant, t would therefore have to decrease.

A differential stress of 0.455 GPa in the cell loaded with KCl are low enough to consider the condition in the DAC to be near-hydrostatic. The St slopes in Fig 9 also appear to be similar to the ones reported by Tateno et al. (2019), where the same calculations were performed on KCl. Using the same method on the cell loaded with Ne returns a higher differential stress, even though this pressure medium is generally thought to cause more hydrostatic conditions within the sample chamber. It is important to remark that

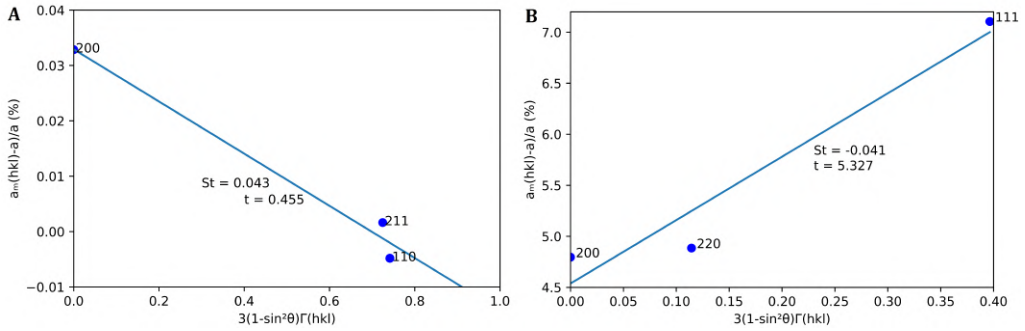

Figure 9: Gamma plots of the measured DACs with a KCl pressure medium (A), and Ne pressure medium (B).

the outcome of these gamma plot slopes strongly depends on the 200 peak being more affected by uniaxial stress compared to the other hkl peaks. This seems to be a common observation in cubic crystals (Tateno et al., 2019), even though it was not observed for Ne here, where the 111 peak was the most affected by differential stress. The conclusions from Wang et al. (2023), where the phase transition pressure is argued to be greatly affected by the differential stress in the sample chamber cannot be confirmed, based on the very low differential stress measured at the phase transition at 30 GPa, which is therefore considered to be valid.

Another possibility to calculate the differential stress in the sample chamber, is to use the SiO_2 peaks directly. This has been done in the past by Singh et al. (2012). When this method is applied to the spectra represented in Figs. 7 & 8, differential stresses of 25.65 GPa and 37.81 GPa are obtained for the KCl-loaded and Ne-loaded cells respectively. This is much higher than the stresses calculated based on the pressure media, most likely because SiO_2 is a much stiffer material that cannot accommodate differential stress as well as the softer KCl or Ne. Again, the stress conditions are lower in the KCl-loaded cell though, when compared to the Ne-loaded cell. Singh et al. (2012) observed that the differential stress in the sample chamber should reach a minimum at the phase transition

pressure, because the elastic softening relaxes the stress conditions. Not enough data points were measured with XRD in this study to confirm this result, but if it is true, it would make the entire discussion of differences in stress conditions leading to a shifting transition pressure void.

4.3 Geophysical implications

The phase transition in pure SiO_2 occurring at 30 GPa has important consequences on geophysical interpretations of the lower mantle. In order to extrapolate results to mantle temperatures, a Clapeyron slope for the phase transition has to be assumed. Clapeyron slopes reported for this phase transition vary between 0.004 GPa/K (Kingma et al., 1995) and 0.015 GPa/K (Bolfan-Casanova et al., 2009). Most of these estimates come from laser-heated DAC experiments, in which temperature measurements come with huge uncertainties. Yamazaki et al. (2014) used a multi-anvil press to determine a Clapeyron slope 0.008 GPa/K for this transition, where temperature determination is much more precise, which is why this is the slope that will also be adopted here. The representation of this extrapolation in P-T-space can be found in Fig. 10. The same Clapeyron slope was also applied to extrapolate previous Brillouin results from Lakshtanov et al. (2007), Asahara et al. (2013) and Zhang et al. (2021) to lower mantle conditions, the result of which is also shown in Fig. 10. Corresponding depths for the transition along the geotherm from Katsura (2022), cold and hot slabs Hirose (2006) can be inferred. As visible in Fig. 10, extrapolating the phase transition pressure of 30 GPa using the Clapeyron slope, brings it to ∼40 GPa at cold slab temperatures, or ∼48 GPa at mantle geotherm temperature. This corresponds to a depth range of ∼1000–1200 km, which is much lower than the previously reported depth range of ∼1400-1700 km based on previous results (e.g. Kaneshima, 2019)). As visible from the seismic cumulative scatterer histogram in Fig. 1, which is also

represented on the right side of Fig. 10, many more scatterers have been found in the range ∼1000–1200 km, compared to ∼1400-1700 km. The few scatterers that do exist in the ∼1400-1700 km depth range have been argued to be too strong to be caused by the stishovite to $CaCl_2$–type SiO_2 phase transition alone (Wang et al., 2020). The phase transition pressure found in this study thus seems to fit geophysical observations better.

All previous studies on SiO_2 containing Al or H are also represented in Fig. 10 through extrapolation with the Clapeyron slope from Yamazaki et al. (2014). As mentioned earlier, the presence of Al and H in SiO_2 has been shown to decrease the transition pressure between stishovite and $CaCl_2$–type SiO_2 significantly (Lakshtanov et al., 2007; Bolfan-Casanova et al., 2009; Nisr et al., 2017a,b; Zhang et al., 2022; Criniti et al., 2023). This causes the results from these studies to plot within the depth range ∼700–1000 km, i.e. right below the results on pure SiO_2 presented here. It is thus possible that the many scatterers observed around ∼700–1000 km depth could also be explained by the phase transition in Al–H–bearing SiO_2. Variation in the exact scatterer depths might be caused by regional differences in the exact subduction slab composition.

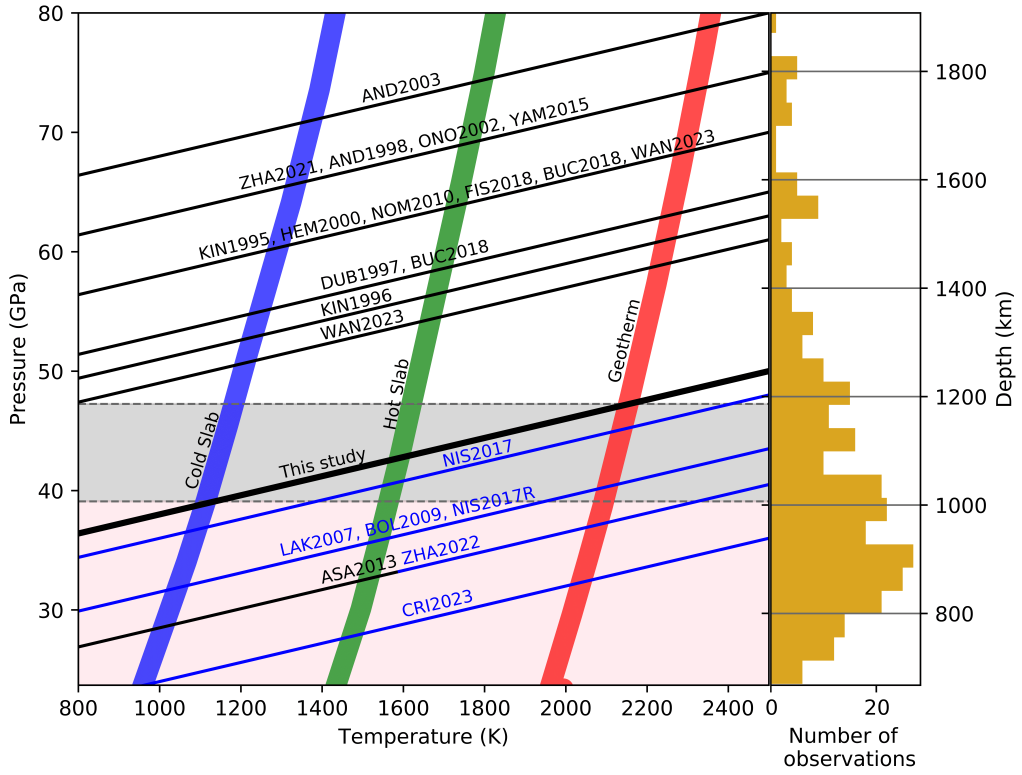

Figure 10: Representation of the stishovite to $CaCl_2$–type SiO_2 phase transition pressures and corresponding depths, based on the measurements performed in this work and previous studies. All phase transition pressures measured at ambient conditions were extrapolated using a Clapeyron slope of 0.008 GPa/K determined by Yamazaki et al. (2014). The mantle geotherm was taken from Katsura (2022), and the cold and hot slab profiles from Hirose (2006). The depth range at which the phase transition could take place based on the measurements presented in this work, combined with temperatures varying between a cold stab and mantle geotherm, are represented as a gray shaded area. The pink shaded area shows the depth range at which the transition could take place if the presence of Al and H is also considered. References corresponding to the short forms are the same as in Fig. 3.

5 Conclusion

A clear drop in shear wave velocity of ∼6% was observed at 30 GPa and ambient temperature in a pure SiO_2 sample, corresponding to the phase transition from stishovite to $CaCl_2$-type SiO_2. The differential stress in the sample chamber calculated based on the positions of the pressure medium in an X-ray diffraction spectrum at the phase transition is very low, and the observed transition pressure should therefore not be affected by it. Brillouin spectroscopy has been shown to be a very robust method to observe a ferroelastic phase transition, as it can be directly detected through a drop in shear wave velocities. This result has important geophysical implications, as it suggests that the phase transition can explain scatterers at shallower pressures than previously thought, anywhere between 1000 and 1200 km, or possibly even lower if the sample would contain Al_2O_3 or H_2O.

Acknowledgements

The authors would like to thank Dr. Sylvain Petitgirard, who was a great help with sample preparation, experiments and discussions during this work. Dr. Tomoaki Kimura was also a great help when it came to learning how to do Brillouin experiments. Ning Ma should also be thanked for doing the XRD measurement at the ESRF, used for this work. The authors gratefully acknowledge ScopeM for their support and assistance in the sample preparation for this work.

References

A. Deuss, J. Andrews, E. D. (2013). Seismic Observations of Mantle Discontinuities and Their Mineralogical and Dyncamical Interpretation. In Karato, S. I., editor, Physics and Chemistry of the Deep Earth, pages 287–323. Wiley.

Akahama, Y. and Kawamura, H. (2006). Pressure calibration of diamond anvil Raman gauge to 310 GPa. Journal of Applied Physics, 100.

Akahama, Y. and Kawamura, H. (2010). Pressure calibration of diamond anvil Raman gauge to 410 GPa. Journal of Physics: Conference Series, 215.

Andrault, D., Angel, R. J., Mosenfelder, J. L., and Le Bihan, T. (2003). Equation of state of stishovite to lower mantle pressures. American Mineralogist, 88(2-3):301–307.

Andrault, D., Fiquet, G., Guyot, F., and Hanfland, M. (1998). Pressure-Induced Landau-Type Transition in Stishovite. American Association for the Advancement of Science, 282:720–724.

Asahara, Y., Hirose, K., Ohishi, Y., Hirao, N., Ozawa, H., and Murakamami, M. (2013). Acoustic velocity measurements for stishovite across the post-stishovite phase transition under deviatoric stress: Implications for the seismic features of subducting slabs in the mid-mantle. American Mineralogist, 98:2053–2062.

Bagley, B., Courtier, A. M., and Revenaugh, J. (2013). Seismic shear wave reflectivity structure of the mantle beneath northeast China and the northwest Pacific. Journal of Geophysical Research: Solid Earth, 118:5417–5427.

Bentham, H. L. and Rost, S. (2014). Scattering beneath Western Pacific subduction zones: Evidence for oceanic crust in the mid-mantle. Geophysical Journal International, 197:1627–1641.

Bolfan-Casanova, N., Andrault, D., Amiguet, E., and Guignot, N. (2009). Equation of state and post-stishovite transformation of Al-bearing silica up to 100 GPa and 3000 K. Physics of the Earth and Planetary Interiors, 174:70–77.

Buchen, J., Marquardt, H., Schulze, K., Speziale, S., Ballaran, T. B., Nishiyama, N., and Hanfland, M. (2018). Equation of State of Polycrystalline Stishovite Across the Tetragonal-Orthorhombic Phase Transition. Journal of Geophysical Research, 123:7347–7360.

Calas, G. and Hawthorne, F. C. (1988). Introduction to Spectroscopic Methods. In Hawthorne, F. C. and Brown, G. E., editors, Spectroscopic methods in mineralogy and geology, volume vol. 18 of Reviews in mineralogy, pages 1–9. Washington, D.C. : Mineralogical Society of America.

Carpenter, M. A., Hemley, R. J., and Mao, H.-k. (2000). High-pressure elasticity of stishovite and the P42/mnm - Pnnm phase transition. Journal of Geophysical Research, 105:807–816.

Castle, J. C. and Creager, K. C. (1999). A steeply dipping discontinuity in the lower mantle beneath Izu-Bonin. Journal of Geophysical Research: Solid Earth, 104(B4):7279–7292.

Courtier, A. M. and Revenaugh, J. (2008). Slabs and shear wave reflectors in the midmantle. Journal of Geophysical Research: Solid Earth, 113(8):1–9.

Criniti, G., Ishii, T., Kurnosov, A., Glazyrin, K., and Boffa Ballaran, T. (2023). High-pressure phase transition and equation of state of hydrous Al-bearing silica. American Mineralogist, 108:1558–1568.

Dove, M. T. (1993). Introduction to lattice dynamics. Cambridge Universtiy Press.

Dubrovinsky, L. S., Saxena, S. K., Lazor, P., and Ahuja, R. (1997). Experimental and theoretical identification of a new high-pressure phase of silica. Nature, 388:1–4.

Every, A. G. and McCurdy, A. K. (1992). Second and Higher Order Elastic Constants. In Nelson, D. F., editor, Low Frequency Properties of Dielectric Crystals, volume Subvolume. Springer-Verlag.

Fischer, R. A., Campbell, A. J., Chidester, B. A., Reaman, D. M., Thompson, E. C., Pigott, J. S., Prakapenka, V. B., and Smith, J. S. (2018). Equations of state and phase boundary for stishovite and $CaCl_2$- type SiO_2. American Mineralogist, 103:792–802.

Hemley, R. J., Shu, J., Carpenter, M. A., Hu, J., Mao, H. K., and Kingma, K. J. (2000). Strain/order parameter coupling in the ferroelastic transition in dense SiO_2. Solid State Communications, 114:527–532.

Hirose, K. (2006). Postperovskite phase transition and its geophysical implications. Reviews of Geophysics, (RG3001).

Howard, C. J., Kennedy, B. J., and Curfs, C. (2005). Temperature-induced structural changes in $CaCl_2$, $CaBr_2$, and $CrCl_2$: A synchrotron x-ray powder diffraction study. Physical Review B - Condensed Matter and Materials Physics, 72(214114).

Jiang, F., Gwanmesia, G. D., Dyuzheva, T. I., and Duffy, T. S. (2009). Elasticity of stishovite and acoustic mode softening under high pressure by Brillouin scattering. Physics of the Earth and Planetary Interiors, 172(3-4):235–240.

Kaminsky, F. V. (2017). Seismic Heterogeneities and Their Nature in the Lower Mantle. In The Earth's Lower Mantle, chapter 10, pages 305–323. Springer.

Kaneshima, S. (2013). Lower mantle seismic scatterers below the subducting Tonga slab: Evidence for slab entrainment of transition zone materials. Physics of the Earth and Planetary Interiors, 222:35–46.

Kaneshima, S. (2016). Seismic scatterers in the mid-lower mantle. Physics of the Earth and Planetary Interiors, 257:105–114.

Kaneshima, S. (2018). Seismic scatterers in the mid-lower mantle beneath Tonga-Fiji. Physics of the Earth and Planetary Interiors, 274:1–13.

Kaneshima, S. (2019). Seismic scatterers in the lower mantle near subduction zones. Geophysical Journal International, 219:S2–S20.

Kaneshima, S. and Helffrich, G. (1998). Detection of lower mantle scatters northeast of the Marianna subduction sone using short-peruid array data. Journal of Geophysical Research, 103:4825–4838.

Kaneshima, S. and Helffrich, G. (1999). Dipping Low-Velocity Layer in the Mid-Lower Mantle : Evidence for Geochemical Heterogeneity. Science, 283(5409):1888–1891.

Kaneshima, S. and Helffrich, G. (2003). Subparallel dipping heterogeneities in the mid-lower mantle. Journal of Geophysical Research, 108:2272.

Kaneshima, S. and Helffrich, G. (2009). Lower mantle scattering profiles and fabric below Pacific subduction zones. Earth and Planetary Science Letters, 282:234–239.

Kaneshima, S., Helffrich, G., Suetsugu, D., Bina, C., Inoue, T., Wiens, D., and Jellinek, M. (2010). Small scale heterogeneity in the mid-lower mantle beneath the circum-Pacific area. Physics of the Earth and Planetary Interiors, 183:91–103.

Karki, B., Warren, M., and Stixrude, L. (1997). Ab initio studies of high-pressure structural transformations in silica. Physical Review B - Condensed Matter and Materials Physics, 55(6):3465–3471.

Katsura, T. (2022). A Revised Adiabatic Temperature Profile for the Mantle. Journal of Geophysical Research: Solid Earth, 127:1–11.

Kawakatsu, H. and Niu, F. (1994). Seismic evidence for a 920-km discontinuity in the mantle. Nature, 371(6495):301–305.

Kingma, K. J., Cohen, R. E., Hemley, R. J., and Mao, H. K. (1995). Transformation of stishovite to a denser phase at lower-mantle pressures. Nature, 374(6519):243–245.

Kingma, K. J., Mao, H.-k., and Hemley, R. J. (1996). Synchrotron X-ray diffraction of SiO_2 to multimegabar pressures. High Pressure Research, 14:363–374.

Korenaga, J. (2014). Teleseismic migration with dual bootstrap stack. Geophysical Journal International, 196:1706–1723.

Lakshtanov, D. L., Sinogeikin, S. V., and Bass, J. D. (2007). High-temperature phase transitions and elasticity of silica polymorphs. Physics and Chemistry of Minerals, 34(1):11–22.

Li, J. and Yuen, D. A. (2014). Mid-mantle heterogeneities associated with Izanagi plate: Implications for regional mantle viscosity. Earth and Planetary Science Letters, 385:137–144.

Liu, L., Bi, Y., Xu, J., and Chen, X. (2010). Ab initio study of the elastic properties of sodium chloride at high pressure. Physica B: Condensed Matter, 405:2175–2180.

Malcherek, T. (2015). Displacive phase transitions. Mineral behaviour at extreme conditions, 7:139–171.

Nisr, C., Leinenweber, K., Prakapenka, V., Prescher, C., Tkachev, S., and Shim, S. H. (2017a). Phase transition and equation of state of dense hydrous silica up to 63 GPa. Journal of Geophysical Research: Solid Earth, 122:6972–6983.

Nisr, C., Shim, S. H., Leinenweber, K., and Chizmeshya, A. (2017b). Raman spectroscopy of water-rich stishovite and dense high-pressure silica up to 55 GPa. American Mineralogist, 102:2180–2189.

Niu, F., Kawakatsu, H., and Fukao, Y. (2003). Seismic evidence for a chemical heterogeneity in the midmantle: A strong and slightly dipping seismic reflector beneath the Mariana subduction zone. Journal of Geophysical Research: Solid Earth, 108(B9):1–12.

Nomura, R., Hirose, K., Sata, N., Ohishi, Y., Suetsugu, D., Bina, C., Inoue, T., Wiens, D., and Jellinek, M. (2010). Precise determination of post-stishovite phase transition boundary and implications for seismic heterogeneities in the mid-lower mantle. Physics of the Earth and Planetary Interiors, 183(1-2):104–109.

Nye, J. F. (1957). Physical Properties of Crystal. Oxford University Press.

Ono, S., Hirose, K., Murakami, M., and Isshiki, M. (2002). Post-stishovite phase boundary in SiO_2 determined by in situ X-ray observations. Earth and Planetary Science Letters, 197(3-4):187–192.

Peterson, N., Gossler, J., Kind, R., Stammler, K., and Vinnik, L. (1993). Precursors to SS and Structure of Transition Zone of the North-Western Pacific. Geophysical Research Letter, 20(4):281–284.

Prescher, C. and Prakapenka, V. B. (2015). DIOPTAS: A program for reduction of two-dimensional X-ray diffraction data and data exploration. High Pressure Research, 35(3):223–230.

Rochira, F., Schumacher, L., and Thomas, C. (2022). Mapping the edge of subducted slabs in the lower mantle beneath southern Asia. Geophysical Journal International, 230:1239–1252.

Salje, E. K. (2012). Ferroelastic Materials. Annual Review of Materials Research, 42(1):265–283.

Seto, Y., Nishio-Hamane, D., Nagai, T., and Sata, N. (2010). Development of a Software Suite on X-ray Diffraction Experiments. The Review of High Pressure Science and Technology, 20(3):269–276.

Shimizu, H., Imaeda, H., Kume, T., and Sasaki, S. (2005). High-pressure elastic properties of liquid and solid neon to 7 GPa. Physical Review B - Condensed Matter and Materials Physics, 71(014108):1–5.

Singh, A. K., Andrault, D., and Bouvier, P. (2012). X-ray diffraction from stishovite under nonhydrostatic compression to 70GPa: Strength and elasticity across the tetragonal → orthorhombic transition. Physics of the Earth and Planetary Interiors, 208-209:1–10.

Singh, A. K., Balasingh, C., Mao, H. K., Hemley, R. J., and Shu, J. (1998). Analysis of lattice strains measured under nonhydrostatic pressure. Journal of Applied Physics, 83(12):7567–7575.

Singh, A. K. and Kenichi, T. (2001). Measurement and analysis of nonhydrostatic lattice strain component in niobium to 145 GPa under various fluid pressure-transmitting media. Journal of Applied Physics, 90(7):3269–3275.

Sirdeshmukh, D. B., Sirdeshmukh, L., and Subhadra, K. G. (2001). Alkali Halides, A Handbook of Physical Properties. Springer-Verlag Berlin Heidelberg.

Speziale, S., Marquardt, H., and Duffy, T. S. (2014). Brillouin Scattering and its Application in Geosciences. In Henderson, G. S., Neuville, D., and Downs, R. T., editors, Reviews in Mineralogy and Geochemistry, volume 78, pages 543–603. The Mineralogical Society of America.

Tateno, S., Komabayashi, T., Hirose, K., Hirao, N., and Ohishi, Y. (2019). Static compression of B2 KCl to 230 GPa and its P-V-T equation of state. American Mineralogist, 104:718–723.

Togo, A., Oba, F., and Tanaka, I. (2008). First-principles calculations of the ferroelastic transition between rutile-type and $CaCl_2$- type SiO_2 at high pressures. Physical Review B - Condensed Matter and Materials Physics, 78(13):1–9.

Tsuchida, Y. and Yagi, T. (1989). A new, post-stishovite high-pressure polymorph of silica. Nature, 342:340 –342.

Umemoto, K., Kawamura, K., Hirose, K., and Wentzcovitch, R. M. (2016). Post-stishovite transition in hydrous aluminous SiO_2. Physics of the Earth and Planetary Interiors, 255:18–26.

Vanacore, E., Niu, F., and Kawakatsu, H. (2006). Observations of the mid-mantle discontinuity beneath Indonesia from S to P converted waveforms. Geophysical Research Letters, 33(4):2–5.

Vinnik, L., Kato, M., and Kawakatsu, H. (2001). Search for seismic discontinuities in the lower mantle. Geophys. J. Int., 147:41–56.

Vinnik, L., Niu, F., and Kawakatsu, H. (1998). Broadband converted phases from midmantle discontinuities. Earth, Planets and Space, 50:987–997.

Wang, B., Buchen, J., San, A., Méndez, J., Kurnosov, A., Criniti, G., Liermann, H.-p., and Marquardt, H. (2023). Strong Effect of Stress on the Seismic Signature of the Post- Stishovite Phase Transition in the Earth ' s Lower Mantle. Geophysical Res, pages 1–9.

Wang, W., Xu, Y., Sun, D., Ni, S., Wentzcovitch, R., and Wu, Z. (2020). Velocity and density characteristics of subducted oceanic crust and the origin of lower-mantle heterogeneities. Nature Communications, 11(1):1–8.

Willmott, P. R., Meister, D., Leake, S. J., Lange, M., Bergamaschi, A., Bo, M., Flechsig, U., Gozzo, F., Henrich, B., Ja, S., and Lu, R. (2013). The Materials Science beamline upgrade at the Swiss Light Source. Journal of Synchrotron Radiation, 20:667–682.

Yamanaka, T., Fukuda, T., and Tsuchiya, J. (2002). Bonding character of SiO_2 stishovite under high pressures up to 30 GPa. Physics and Chemistry of Minerals, 29:633–641.

Yamazaki, D., Ito, E., Yoshino, T., Tsujino, N., Yoneda, A., Guo, X., Xu, F., Higo, Y., and Funakoshi, K. (2014). Over 1 Mbar generation in the Kawai-type multianvil apparatus and application to compression of $(Mg_{0.92}Fe_{0.08})SiO_3$ perovskite and stishovite. Physics of the Earth and Planetary Interiors, 228:262–267.

Yang, R. and Wu, Z. (2014). Elastic properties of stishovite and the $CaCl_2$- type silica at the mantle temperature and pressure: An ab initio investigation. Earth and Planetary Science Letters, 404:14–21.

Yang, Z. and He, X. (2015). Oceanic crust in the mid-mantle beneath west-central Pacific subduction zones: Evidence from S to P converted waveforms. Geophysical Journal International, 203:541–547.

Yuan, Y., Sun, D., and Thomas, C. (2023). A New Seismic Phase to Detect Mid-Mantle Scatterers. Geophysical Research Letters, 50:1–10.

Zhang, Y., Fu, S., ichiro Karato, S., Okuchi, T., Chariton, S., Prakapenka, V. B., and Lin, J. F. (2022). Elasticity of Hydrated Al-Bearing Stishovite and Post-Stishovite: Implications for Understanding Regional Seismic VS Anomalies Along Subducting Slabs in the Lower Mantle. Journal of Geophysical Research: Solid Earth, 127:e2021JB023170.

Zhang, Y., Fu, S., Wang, B., and Lin, J.-F. (2021). Elasticity of a Pseudoproper Ferroelastic Transition from Stishovite to Post-Stishovite at High Pressure. Physical Review Letters, 126:025701.

Chapter 4

Optimizing Hydrous Mantle Endmembers for Gibbs Free Energy Minimizations

This chapter represents a side-project that was worked on during the two last years of this doctorate. Unfortunately, due to the many challenges faced in the work shown in Chapter 2 and preparation of Chapter 3, very little time was left to work on this project over the last year. Most of the time spent on this project involved figuring out how to make the optimizations work that are detailed in this Chapter. The code that was used for this was relatively recently developed by Dean Khan, and understanding how it works and how it could be adjusted for my needs took a lot of time. Only a few weeks ago was a final version of the code achieved that seems to be doing all the optimizations correctly. For this reason it is still a work in progress.

Creating Hydrous Endmembers for Gibbs Free Energy Minimizations

Thomas de Selva-Dewint[1*], Dean Khan[2],
James Connolly[1], Amir Khan[1], Motohiko Murakami[1]
[1]Department of Earth Sciences, ETH Zürich, Sonneggstrasse 5, 8092 Zurich, Switzerland
[2]Earth, Environmental, and Planetary Sciences, Brown University,
Providence, RI 02912, United States

[*]E-mail: thomas.deselva@erdw.ethz.ch.

The presence of water in mantle phases is a topic that has thoroughly been investigated experimentally. Geophysical inversion models using Gibbs Free Energy Minimizations to calculate phase assemblages do not include the effect of water on phase stability fields and their physical properties however. Enough experimental results on the solubility of water in mantle phases and its effect on the elasticity of these phases is available to make an attempt at including this data in future geophysical models. In order to achieve that, this work suggests to establish hydrous endmembers in the Stixrude and Lithgow-Bertelloni (2011) database that could be used in future models making use of the PerpleX program (Connolly, 2005). Thermodynamic parameters for hydrous endmembers of olivine (H_4SiO_4), pyroxene (H_2SiO_3), garnet ($H_{12}Si_3O_{12}$), wadsleyite (H_4SiO_4) and ringwoodite (H_4SiO_4) are calculated by using an optimization algorithm developed by Khan et al. (2021), by using results from previous experimental studies.

1 Introduction

The rocky planets of our solar system are all thought to have incorporated a certain amount of water into their interior during planet formation (Peslier et al., 2017). The exact quantity present in planetary interiors has been the topic of many studies. In order to determine it, two types of experiments are necessary. On the one hand, solubility experiments have to be made on minerals thought to be present in planetary interiors at relevant temperature and pressure conditions. On the other hand, experiments have to be conducted that quantify the effect of water on the physical properties of these minerals. Properties like the elasticity, anelasticity, and electrical conductivity of a mineral can be measured and compared to direct geophysical observations of the planetary body of interest.

The comparison of experimental and geophysical data is typically done through setting up a geophysical model. Experimental results can be modeled forward in order to include them in a more general model, and geophysical results have to be inverted in order to come up with a planetary model (Khan, 2016). During such geophysical modeling procedures, a Gibbs Free Energy Optimization program like PerpleX (Connolly, 2005) is often utilized to determine a stable mineral assemblage and its corresponding thermodynamic parameters at a given pressure, temperature and composition. The current thermodynamic databases used within PerpleX (Stixrude and Lithgow-Bertelloni, 2011, 2022) do not consider hydrogen and thus neglect the effect of hydrogen on mineral phases. It is possible to model the effect of water on certain geophysical properties while using these databases, but comes with the erroneous assumption that hydrogen would have no effect on the stability fields of these minerals. To solve this problem, we propose to add hydrous endmembers to the relevant mantle phases for Mars based on literature data.

The presence of the InSight lander on Mars (Banerdt et al., 2013), which was equipped with a seismometer, has allowed for the detection of numerous marsquakes (Clinton et al., 2021). The investigation of body waves traveling through the Martian interior has opened up the possibility to constrain its internal structure and composition (Durán et al., 2022). For example, based on S-wave reflections, the core-mantle boundary was found to be located at a depth of 1520–1600 km (with the core having a radius of 1770–1890 km, Stähler et al., 2021). As a consequence, phases present in the Martian mantle essentially represent the ones present in the Earth's upper mantle and transition zone. These phases are crystallographically equivalent to the ones present in the Earth's mantle, but can have a different composition. For example, a more iron-rich composition has to be considered for Mars (McSween and Huss, 2010), due to the slightly higher iron content of the Martian mantle (∼13.7 wt% according to Khan et al., 2022). Also, the overall volatile content of the Martian interior is thought to be higher than that of the Earth, although it might not all be present in the mantle, with the core having been proposed to contain a relatively large amount of volatiles due to its low density (Khan et al., 2022). Recently, the existence of a ∼150 km thick liquid silicate layer at the bottom of the Martian mantle has also been proposed to exist (Khan et al., 2023), changing the core radius to ∼1675 km.

Comparison of the measured seismic velocities in the Martian mantle with previous experimental results on hydrous upper mantle and transition zone minerals would allow for an estimation of the water content of the Martian mantle, which motivated the undertaking of this work. Previous work by Dong et al. (2022) has also tried to calculate Mars' water content. They found that the Martian mantle's water storage capacity is quite high, but concluded that the lack of an efficient recycling mechanism of deep-water most likely means that its actual water content would be much lower. This work instead intends to make use of geophysical data to estimate the current water content of Mars'

mantle.

Methodology

Every endmember phase in the Stixrude and Lithgow-Bertelloni (2011) (hereafter STX11) database is described by the thermodynamic parameters given in Table 1. These are the parameters that are required to be optimized for hydrous phases. Further details on the parameters can be found in Stixrude and Lithgow-Bertelloni (2005, 2010, 2011).

Table 1: Thermodynamic parameters for each endmember in the database by Stixrude and Lithgow-Bertelloni (2011).

Parameter	Unit	Meaning
G0	J/mol	Helmholtz free energy
S0	unitless	Number of cations
V0	cm^3/mol	Volume at ambient conditions
c1	bar	Isothermal bulk modulus
c2	unitless	First derivative of isothermal bulk modulus
c3	K	Debye temperature at ambient conditions.
c4	unitless	γ_0 or $V(\partial P/\partial U)_V$.
c5	unitless	q_0 or $\partial ln\gamma/\partial lnV$ with γ = c4
c6	unitless	Shear strain derivative of γ or c4
m0	bar	Shear modulus at ambient conditions, G_0
m1	unitless	First pressure derivative of G_0, G_0'

Short forms: V–volume, P–pressure, and U–internal energy.

1.1 Initial guess for hydrous endmembers

In order to make an initial guess as to what the parameters in Table 1 could be for hydrous mantle phases, the database by Holland and Powell (2011) (hereafter HP11) was used. That database is generally used for Gibbs Free Energy minimizations in the Earth's crust, and therefore contains some hydrous phases. These were used to make an initial guess of what the thermodynamic parameters for hydrous clinoenstatite (hycen), hydrous garnet (hgrt), hydrous olivine (hfo), hydrous wadsleyite (hwd) and hydrous ringwoodite (hrw)

would be. This was done through the following chemical reactions:

$$\mathrm{H_4SiO_4}(hfo) = \mathrm{Mg_2SiO_4}(fo) + 2\mathrm{Mg(OH)_2}(br) - 4\mathrm{MgO}(per)$$

$$\mathrm{H_4SiO_4}(hwd) = \mathrm{Mg_2SiO_4}(wd) + 2\mathrm{Mg(OH)_2}(br) - 4\mathrm{MgO}(per)$$

$$\mathrm{H_4SiO_4}(hrw) = \mathrm{Mg_2SiO_4}(rw) + 2\mathrm{Mg(OH)_2}(br) - 4\mathrm{MgO}(per)$$

$$\mathrm{H_4Si_2O_6}(hycen) = \mathrm{Mg_2Si_2O_6}(cen) + 2\mathrm{Mg(OH)_2}(br) - 4\mathrm{MgO}(per)$$

$$\mathrm{H_{12}Si_3O_{12}}(hgrt) = \mathrm{Mg_3(Mg,Si)Si_3O_12}(mj) + \mathrm{Mg(OH)_2}(br) - 10\mathrm{MgO}(per) - \mathrm{SiO_2}(st)$$

Thermodynamic parameters for clinoenstatite (cen), majorite (mj), forsterite (fo), Mg-wadsleyite (wd), ringwoodite (rw), brucite (br, $\mathrm{Mg(OH)_2}$), periclase (per, MgO), and stishovite (st, $\mathrm{SiO_2}$) endmembers are all available in Holland and Powell (2011). Parameters defined for the same endmembers in the Holland and Powell (2011) database are distinct from the ones used in the STX11 database represented in Table 1. To translate parameters between databases, the optimization algorithm by Khan et al. (2021) was applied.

The Khan et al. (2021) algorithm was made to optimize thermodynamic parameters based on experimental data through Bayesian inference. A Maximum Likelihood Estimate is calculated for every parameter by performing Least Squares Minimizations on the experimental data and its uncertainties. Firstly, Simulated Annealing is performed to find a global minimum in the dataset. Then, a Nelder-Mead Algorithm is applied to further explore local minima around that global minimum and come up with the best solutions. The algorithm could therefore be used to optimize the thermodynamic parameters for the relevant endmembers in the STX11 database, according to how much the according dry and newly created hydrous endmembers in the HP11 database differ. The result of this first optimization represents the 'first guess' of the thermodynamic parameters of hydrous olivine, wadsleyite, ringwoodite, enstatite and garnet in the adjusted STX11 database.

Without having to go too much into detail, a practical example to better understand the optimization process would be the following: An algorithm asks PerpleX to calculate the heat capacity of dry and hydrous wadsleyite at 13 GPa and 1200 K, based on the already existing dry endmember and newly created hydrous endmember parameters in HP11. The difference between these two is then used in the algorithm to 'optimize' the dry thermodynamic parameters of wadsleyite in the STX11 database and thereby transform them to create a hydrous endmember.

1.2 Optimizing the hydrous endmembers according to experimental data

Now that an initial guess for the thermodynamic parameters in Table 1 exists for all relevant hydrous endmembers in the STX11 database, these can further be optimized based on experimental data of these phases. This is done by optimizing all the thermodynamic parameters based on equilibrium experiments on the water solubility in mantle phases. Then, c1, c2, m0 & m1 are further optimized based on previous work studying the effect of water on the elasticity of these phases.

1.2.1 Optimizations based on equilibrium experiments

A thorough investigation of the literature was made to find all possible studies reporting measured water contents in mantle phases. This study focuses on the mantle of Mars, so only minerals that occur in the Earth's upper mantle and transition zone are considered. These are: olivine, pyroxene, garnet, wadsleyite and ringwoodite. A summary of the literature studies utilized for this purpose is given in Table 2. Most of the studies summarized in the table performed multiple experiments within the given pressure and temperature ranges, resulting in a range of water contents.

After all the literature data had been compiled, the algorithm from Khan et al. (2021) optimizes all thermodynamic parameters by comparing the water content calculated in

PerpleX at the same pressure and temperature conditions based on the already existing hydrous endmember, to the reported experimental result. Initially the existing hydrous endmember corresponds to the 'first guess' calculated in Section 1.1, but this changes as optimizations proceed.

A big assumption about all the experiments listed in Table 2, is that their measured water contents are representative of equilibrium conditions. A sample is in equilibrium when it has the time to chemically and thermally equilibrate with the coexisting mineral phases or melt during the experiment. Researchers aim to achieve such conditions, but it is impossible to verify whether or not equilibrium was always reached. It is therefore important to combine data from as many sources as possible to even out any outliers that could be caused by non-equilibrium conditions.

Table 2: Equilibrium studies examining the solubility of water in mantle minerals

Reference	Pressure(GPa)	Temperature (K)	H_2O wt.%
Experiments on hydrous olivine			
Kohlstedt et al. (1996)	2.13	1273–1373	0.01 - 0.15
Chen et al. (2002)	13–15	1473	0.20–3.5
Litasov and Ohtani (2003)	10–24	1173–1673	0.29–0.80
Zhao et al. (2004)	0.3	1273–1573	0.01–0.16
Mosenfelder et al. (2006)	2–12	1273–1573	0.03–0.64
Smyth et al. (2006)	12	1523–1873	0.10–0.89
Withers and Hirschmann (2007)	7–13	1373–1573	0.07–0.43
Litasov et al. (2007)	12.5 –14	1373–2273	0.02–0.62
Withers and Hirschmann (2008)	8	1673–1873	0.03–0.15
Bali et al. (2008)	2.5–9	1273–1673	0.01–0.20
Litasov et al. (2009)	8–14	1573–2273	0.10–0.54
Tenner et al. (2009)	3–5	1623–1713	0.09–0.11
Withers et al. (2011)	3	1473–1773	0.01–0.08
Tenner et al. (2012)	10–12	1623–1723	0.03–0.09
Ardia et al. (2012)	5–8	1673–1773	0.01–0.02

continued

Table 2: Equilibrium studies examining the solubility of water in mantle minerals

Reference	Pressure(GPa)	Temperature (K)	H_2O wt.%
Fei and Katsura (2020)	8	1523	0.05–0.30
Partitioning experiments between olivine and pyroxene			
Withers and Hirschmann (2007)	7 - 13	1473 - 1673	0.08 - 1.87 (ol) 0.09 - 0.67 (px)
Withers and Hirschmann (2008)	8	1673	0.07 - 0.08 (ol) 0.09 - 0.12 (px)
Withers et al. (2011)	5 - 9	1473	0.05 - 0.13 (ol) 0.04 - 0.08 (px)
Férot and Bolfan-Casanova (2012)	2.5 - 9	1448 - 1673	0.01 - 0.47 (ol) 0.01 - 0.79 (px)
Tenner et al. (2012)	10 - 13	1623 - 1723	0.00 - 0.12 (ol) 0.01 - 0.79 (px)
Sakurai et al. (2014)	1.5–6	1573–-1723	<0.01 (ol) <0.01–0.03 (px)
Kang and Karato (2023)	3–5	1373–1573	0.03–0.09 (ol) 0.04–0.13 (px)
Experiments on hydrous pyroxene			
Rauch and Keppler (2002)	7.5	1373	0.09
Mierdel et al. (2007)	1.5–3.5	1073–1373	0.1–0.7
Liu and Yang (2020)	0.2–3	1073–1473	<0.01–0.03
Partitioning experiments between olivine and wadsleyite			
Kohlstedt et al. (1996)	14 - 15	1373	2.13 - 2.41
Chen et al. (2002)	13 - 14.4	1473	0.37 - 0.64 (ol) 1.90 - 3.40 (wd)
Litasov et al. (2006)	12.5 - 14	1473 - 1773	0.14 - 0.18 (ol) 0.67 - 1.77 (wd)
Experiments on hydrous wadsleyite			
Kohlstedt et al. (1996)	19.5	1373	0.20 - 2.62
Kawamoto et al. (1996)	13.5 - 16.5	1573 - 1773	1.52 - 2.89
Smyth et al. (1997)	17.5	1673	2.24
Bolfan-Casanova et al. (2000)	15	1573	0.22
Demouchy et al. (2005)	15	1173 - 1673	0.93 - 2.6

continued

Table 2: Equilibrium studies examining the solubility of water in mantle minerals

Reference	Pressure(GPa)	Temperature (K)	H_2O wt.%
Jacobsen et al. (2005)	16 - 18	1673 - 2373	0.01 - 1.06
Litasov and Ohtani (2008)	12 - 20	1473 - 2273	0.07 - 2.12
Litasov et al. (2011)	14 - 20	1473 - 2173	0.22 - 2.07
Sun et al. (2018)	16	1923	0.95
Bolfan-Casanova et al. (2018)	15 - 19	1473 - 1923	0.16 - 3.11
Druzhbin et al. (2021)	17	1673	0.61 - 1.25
Fei and Katsura (2021)	17.5 - 20	1500 - 2100	0.58 - 2.42
Partitioning experiments between wadsleyite and ringwoodite			
Kawamoto et al. (1996)	15.5	1573	1.83 (wd) 0.1 (rw)
Inoue et al. (2010)	16.5 - 17	1673	1.79 - 3.72 (wd) 1.00 - 1.69 (rw)
Experiments on hydrous ringwoodite			
Inoue et al. (1995)	15.5	1473 - 1573	1.10 - 3.10[†]
Bolfan-Casanova et al. (2000)	19	1200 - 1300	0.06 - 0.78
Ohtani et al. (2000)	20 - 23	1573 - 1723	0.20 - 2.60
Smyth et al. (2003)	18 - 22	1673 - 1773	0.20 - 1.07
Bolfan-Casanova et al. (2003)	24	1673	0.14[*]
Bolfan-Casanova et al. (2018)	19 - 22	1573 - 1973	0.02 - 1.83
Fei and Katsura (2020)	23	1600 - 2000	0.25 - 2.03
Experiments on hydrous garnet			
Geiger et al. (1991)	2–5	1073–1273	0.02–0.07
Lu and Keppler (1997)	1.5–10	1073– 1273	<0.01–0.02
Withers et al. (1998)	2–8	1273	0.01–0.10
Bolfan-Casanova et al. (2000)	17.5	1773	0.07
Tenner et al. (2009)	5	1713	0.01–0.03
Mookherjee and Karato (2010)	5–9	1373– 1473	<0.01–0.06
Zhang et al. (2022)	1–3	1073– 1273	<0.01

[*] coexisting with dry bridgmanite and ferropericlase.
[†] coexisting with hydrous enstatite.

Table 3: Experimental works on the elasticity of hydrous mantle minerals

Reference	Pressure(GPa)	Temperature (K)
hydrous olivine		
Abramson et al. (1997)	8–12	298
Jacobsen et al. (2008)	12	1323
Mao et al. (2010)	0–14	298
Faccincani et al. (2023)	1.5–10	298
hydrous wadsleyite		
Mao et al. (2008)	1–12	298
Mao et al. (2011)	0–24	298–1773
Buchen et al. (2018)	1–24	298–1773
Zhou et al. (2021)	0–19	298
hydrous ringwoodite		
Inoue et al. (1998)	19	1573
Wang et al. (2003)	0	298
Jacobsen et al. (2004)	0	298
Wang et al. (2006)	2–23	298
Jacobsen and Smyth (2006)	0–9	300
Mao et al. (2012)	0–16	300–673
Schulze et al. (2018)	1–22	298–500

1.2.2 Optimizations based on elasticity experiments

Another examination of the literature was undertaken to find all possible studies reporting an effect of water on the elasticity of the relevant mantle phases. The elasticity experiments used for the optimization of hydrous olivine, wadsleyite and ringwoodite is given in Table 3. The c1, c2, m0 & m1 parameters of the hydrous phases were further optimized based on the tabulated data, since they affect the elasticity of the material. Due to the lack of elasticity data on hydrous pyroxenes and hydrous garnets, this extra optimization of c1, c2, m0 & m1 was not performed for those two phases.

The elasticity experiments from the studies listed in Table 3 are often performed on single mineral, measuring shear (V_S) or pressure (V_P) wave velocities over pressure and temperature ranges in which the mineral in question might be partly metastable. They

thus often do not represent equilibrium experiments. This is why they could not be included in Table 2. This is also the reason that optimizations of c1, c1, m0 & m1 based on these results had to be run for every phase individually. The optimizations are done by asking PerpleX to calculate V_S or V_P based on the already existing parameters of the hydrous phase. These parameters are then optimized based on the difference between the calculated and the experimental acoustic velocities.

Preliminary results

An overview of the currently optimized thermodynamic parameters for the hydrous end-members is given in Table 4. These results are preliminary and their validity still has to be evaluated. Some optimizations also have to be rerun since some changes to the Khan et al. (2021) algorithm were made. No conclusion regarding Mars' mantle water content can yet be drawn based on the available results.

Issues encountered so far with the method presented here are the following. Firstly, there is often a very large variation in the results of relatively few experimental studies, that sometimes even contradict each other, making the initial Simulated Annealing step in the modeling procedure difficult. A global minimum can be hard to find, and the algorithm has to sometimes be run several times before a consistent result can be achieved. It might be that eventually, due to poor quality of the data, the Bayesian approach will be replaced by a simple Least-Squares regression. Secondly, many equilibrium experiments contain some amount of melt in the resulting mineral phases. This might be a source of error, as it is hard to determine what the thermodynamic parameters of such a phase would be, and because it might contain a significant amount of water (which is often not reported). Its presence could therefore skew water contents to lower values in the mineral phases. Some of the patterns observed in Table 4 reflect the issues highlighted above.

For example, it is quite well-agreed upon that upon hydration a mineral's bulk and shear modulus decrease, while their first derivatives increase. Even though, the bulk modulus seems to behave accordingly after the equilibrium optimizations, the shear modulus of wadsleyite, ringwoodite and garnet displays opposite behavior. Performing the elasticity optimizations subsequently fixes some of that behavior, but not entirely.

Most error seems to arise from the equilibrium optimizations, which is why future optimizations will be performed excluding all results containing melts to try to determine its effect on them, even if very few equilibrium studies remain that do not contain any melt fraction. The optimization based on elasticity measurements of hydrous minerals will done before the equilibrium optimizations in the future, as they seem to behave more accordingly to what is expected.

The paucity of previous studies of a similar nature makes the comparison of these preliminary results difficult. Thio et al. (2016) developed a method to estimate the effect of water in a mantle assemblage on observed geophysical signals. For this, they also compiled results from experimental studies on olivine, wadsleyite and ringwoodite, to constrain the effect of a certain amount of water on their thermodynamic parameters. Then, they performed numerical experiments on a CFMAS composition using Perple_X and adjusted the resulting parameters by extrapolating the previously determined effect of water at ambient conditions. Based on these, conclusions are drawn regarding the effect of water on phase boundaries and seismic properties of mantle phases. Unlike the method presented here, H_2O is not actually added to the thermodynamic database from Stixrude and Lithgow-Bertelloni (2011), and the thermodynamic parameters for hydrous endmembers used are not reported, making a direct comparison between both methods difficult. Moreover, the effect of water in pyroxene and garnet is deemed insignificant in Thio et al. (2016), even though many experimental studies have demonstrated that

pyroxene would be a more important water carrier than olivine in the Earth's upper mantle, with partition coefficients generally in favor of pyroxene (see Table 2).

Table 4: Preliminary results of thermodynamic parameters for hydrous mantle endmembers.

Phase	G0 (J/mol)	S0	V0 (cm^3/mol)	c1 (bar)	c2	c3 (K)	c4	c5	c6	m0 (bar)	m1
Dry endmembers from Stixrude and Lithgow-Bertelloni (2011)											
fo	-2055403	-7	-4.36	1279555	4.22	809.17	0.99	2.11	2.30	816000	1.46
wd	-2027837	-7	-4.05	1686948	4.32	843.50	1.21	2.02	2.64	1120000	1.44
rw	-2017557	-7	-3.95	1849009	4.22	877.71	1.11	2.39	2.30	1230000	1.35
cen	-2905918	-10	-6.25	1122413	5.24	805.05	0.96	1.53	1.69	794969	1.63
mj	-5691614	-20	-11.43	1651183	4.21	822.46	0.98	1.54	1.02	850000	1.43
Hydrous endmembers based on the optimizations using Equilibrium experiments from Table 2											
hfo	-1650297	-9	-5.61	543950	5.63	637.81	0.90	2.01	2.15	787106	1.45
hwd	-1608934	-9	-7.06	409158	5.41	671.10	0.99	1.74	2.18	1121399	1.68
hrw	-1602801	-9	-5.19	545919	6.45	647.30	1.04	2.02	2.72	1301359	1.60
hycen	-2571168	-12	-5.44	441996	5.81	615.30	0.66	2.05	5.56	672784	1.09
hgrt	-297599	-23	-15.10	432958	5.30	444.25	0.40	2.10	0.65	890274	1.60
Hydrous endmembers based on the optimizations using Elasticity experiments from Table 3											
hfo			-4.66	1215012	3.83					799835	1.15
hwd			-4.35	1058744	2.05					1269999	2.04
hrw			-3.88	2191980	1.93					1140834	1.42

Short forms: Forsterite (fo), Mg-wadsleyite (wd), Mg-ringwoodite (rw), clinoenstatite (cen), majorite (mj), hydrous olivine (hfo), hydrous wadsleyite (hwd), hydrous ringwoodite (hrw), hydrous enstatite (hycen) and hydrous garnet (hgrt).

References

Abramson, E. H., Brown, J. M., Slutsky, L. J., and Zaug, J. (1997). The elastic constants of San Carlos olivine to 17 GPa. Journal of Geophysical Research: Solid Earth, 102(B6):12253–12263.

Ardia, P., Hirschmann, M. M., Withers, A. C., and Tenner, T. J. (2012). H_2O storage capacity of olivine at 5-8 GPa and consequences for dehydration partial melting of the upper mantle. Earth and Planetary Science Letters, 345-348:104–116.

Bali, E., Bolfan-Casanova, N., and Koga, K. T. (2008). Pressure and temperature dependence of H solubility in forsterite: An implication to water activity in the Earth interior. Earth and Planetary Science Letters, 268:354–363.

Banerdt, Boschi, L., Christensen, U., Dehant, V., Giardini, D., Goetz, W., Golombek, M., Grott, M., Hudson, T., Johnson, C., Kargl, G., Kobayashi, N., Maki, J., Mimoun, D., Mocquet, A., Morgan, P., Panning, M., Pike, W. T., Tromp, J., Zoest, T. V., and Wieczorek, M. (2013). InSight: A Discovery Mission to Explore the Interior of Mars. 44th Lunar and Planetary Science Conference, (June 2015):1915.

Bolfan-Casanova, N., Keppler, H., and Rubie, D. C. (2000). Water partitioning between nominally anhydrous minerals in the MgO-SiO_2-H_2O system up to 24 GPa: Implications for the distribution of water in the Earth's mantle. Earth and Planetary Science Letters, 182:209–221.

Bolfan-Casanova, N., Keppler, H., and Rubie, D. C. (2003). Water partitioning at 660 km depth and evidence for very low water solubility in magnesium silicate perovskite. Geophysical Research Letters, 30:1–4.

Bolfan-Casanova, N., Schiavi, F., Novella, D., Bureau, H., Raepsaet, C., Khodja, H., and Demouchy, S. (2018). Examination of water quantification and incorporation in transition zone minerals: Wadsleyite, ringwoodite and phase D using ERDA (elastic recoil detection analysis). Frontiers in Earth Science, 6(76).

Buchen, J., Marquardt, H., Speziale, S., Kawazoe, T., Boffa Ballaran, T., and Kurnosov, A. (2018). High-pressure single-crystal elasticity of wadsleyite and the seismic signature of water in the shallow transition zone. Earth and Planetary Science Letters, 498:77–87.

Chen, J., Inoue, T., Yurimoto, H., and Weidner, D. J. (2002). Effect of water on olivine-wadsleyite phase boundary in the $(Mg, Fe)_2SiO_4$ system. Geophysical Research Letters, 29(18):1875.

Clinton, J. F., Ceylan, S., van Driel, M., Giardini, D., Stähler, S. C., Böse, M., Charalambous, C., Dahmen, N. L., Horleston, A., Kawamura, T., Khan, A., Orhand-Mainsant, G., Scholz, J. R., Euchner, F., Banerdt, W. B., Lognonné, P., Banfield, D., Beucler, E., Garcia, R. F., Kedar, S., Panning, M. P., Perrin, C., Pike, W. T., Smrekar, S. E., Spiga, A., and Stott, A. E. (2021). The Marsquake catalogue from InSight, sols 0–478. Physics of the Earth and Planetary Interiors, 310:106595.

Connolly, J. A. (2005). Computation of phase equilibria by linear programming: A tool for geodynamic modeling and its application to subduction zone decarbonation. Earth and Planetary Science Letters, 236:524–541.

Demouchy, S., Deloule, E., Frost, D. J., and Keppler, H. (2005). Pressure and temperature-dependence of water solubility in Fe-free wadsleyite. American Mineralogist, 90:1084–1091.

Dong, J., Fischer, R. A., Stixrude, L. P., Lithgow-Bertelloni, C. R., Eriksen, Z. T., and Brennan, M. C. (2022). Water storiage capacity of the Martian mantle through time. Icarus.

Druzhbin, D., Fei, H., and Katsura, T. (2021). Independent hydrogen incorporation in wadsleyite from oxygen fugacity and non-dissociation of H_2O in the reducing mantle transition zone. Earth and Planetary Science Letters, 557:116755.

Durán, C., Khan, A., Ceylan, S., Zenhäusern, G., Stähler, S., Clinton, J., and Giardini, D. (2022). Seismology on Mars: An analysis of direct, reflected, and converted seismic body waves with implications for interior structure. Physics of the Earth and Planetary Interiors, 325:106851.

Faccincani, L., Criniti, G., Kurnosov, A., Ballaran, T. B., Withers, A. C., Mazzucchelli, M., Nestola, F., and Coltorti, M. (2023). Sound velocities and single-crystal elasticity of hydrous Fo90 olivine to 12 GPa. Physics of the Earth and Planetary Interiors, 337:107011.

Fei, H. and Katsura, T. (2020). Pressure Dependence of Proton Incorporation and Water Solubility in Olivine. Journal of Geophysical Research: Solid Earth, 125.

Fei, H. and Katsura, T. (2021). Water Solubility in Fe-Bearing Wadsleyite at Mantle Transition Zone Temperatures. Geophysical Research Letters, 48.

Férot, A. and Bolfan-Casanova, N. (2012). Water storage capacity in olivine and pyroxene to 14 GPa: Implications for the water content of the Earth's upper mantle and nature of seismic discontinuities. Earth and Planetary Science Letters, 349-350:218–230.

Geiger, C. A., Langer, K., Bell, D. R., Rossman, G. R., and Winkler, B. (1991). The hydroxide component in synthetic pyrope. American Mineralogist, 76:49–59.

Holland, T. J. and Powell, R. (2011). An improved and extended internally consistent thermodynamic dataset for phases of petrological interest, involving a new equation of state for solids. Journal of Metamorphic Geology, 29:333–383.

Inoue, T., Wada, T., Sasaki, R., and Yurimoto, H. (2010). Water partitioning in the Earth's mantle. Physics of the Earth and Planetary Interiors, 183(1-2):245–251.

Inoue, T., Weidner, D. J., Northrup, P. A., and Parise, J. B. (1998). Elastic properties of hydrous ringwoodite (γ-phase) in Mg_2SiO_4. Earth and Planetary Science Letters, 160:107–113.

Inoue, T., Yurimoto, H., and Kudoh, Y. (1995). Hydrous modified spinel, $Mg_{1.75}SiH_{0.5}O4$: A new water reservoir in the mantle transition region. Geophysical Research Letters, 22(2):117–120.

Jacobsen, S. D., Demouchy, S., Frost, D. J., Ballaran, T. B., and Kung, J. (2005). A systematic study of OH in hydrous wadsleyite from polarized FTIR spectroscopy and single-crystal X-ray diffraction: Oxygen sites for hydrogen storage in Earth's interior. American Mineralogist, 90:61–70.

Jacobsen, S. D., Jiang, F., Mao, Z., Duffy, T. S., Smyth, J. R., Holl, C. M., and Frost, D. J. (2008). Effects of hydration on the elastic properties of olivine. Geophysical Research Letters, 35:L14303.

Jacobsen, S. D. and Smyth, J. R. (2006). Effect of water on the sound velocities of ringwoodite in the transition zone. Geophysical Monograph Series, 168:131–145.

Jacobsen, S. D., Smyth, J. R., Spetzler, H., Holl, C. M., and Frost, D. J. (2004). Sound velocities and elastic constants of iron-bearing hydrous ringwoodite. Physics of the Earth and Planetary Interiors, 143:47–56.

Kang, L. and Karato, S.-I. (2023). Hydrogen Partitioning Between Olivine and Orthopyroxene: Implications for the Lithosphere-Asthenosphere Structure. Journal of Geophysical Research: Solid Earth, 128.

Kawamoto, T., Hervig, R. L., and Holloway, J. R. (1996). Experimental evidence for a hydrous transition zone in the early Earth's mantle. Earth and Planetary Science Letters, 142:587–592.

Khan, A. (2016). On Earth's Mantle Constitution and Structure from Joint Analysis of Geophysical and Laboratory-Based Data: An Example. Surveys in Geophysics, 37:149–189.

Khan, A., Huang, D., Durán, C., Sossi, P. A., Giardini, D., and Murakami, M. (2023). Evidence for a liquid silicate layer atop the Martian core. Nature, 622:718–723.

Khan, A., Sossi, P. A., Liebske, C., Rivoldini, A., and Giardini, D. (2022). Geophysical and cosmochemical evidence for a volatile-rich Mars. Earth and Planetary Science Letters, 578:117330.

Khan, D., Liebske, C., and Connolly, J. A. D. (2021). An Algorithm for Thermodynamic Parameter Optimization: Application to the Martian Mantle. Geochemistry, Geophysics, Geosystems, 22:1–12.

Kohlstedt, D. L., Keppler, H., and Rubie, D. C. (1996). Solubility of water in the α, β and γ phases of $(\mathrm{Mg,Fe})_2\mathrm{SiO}_4$. Contributions to Mineralogy and Petrology, 123:345–357.

Litasov, K. and Ohtani, E. (2003). Stability of various hydrous phases in CMAS pyrolite-$\mathrm{H_2O}$ system up to 25 GPa. Physics and Chemistry of Minerals, 30:147–156.

Litasov, K. and Ohtani, E. (2008). Systematic study of hydrogen incorporation into Fe-bearing wadsleyite and water storage capacity of the transition zone. AIP Conference Proceedings, 987:113–118.

Litasov, K. D., Ohtani, E., Kagi, H., and Ghosh, S. (2006). Influence of water on olivine-wadsleyite phase transformation and water partitioning near 410-km seismic discontinuity. AIP Conference Proceedings, 833(150).

Litasov, K. D., Ohtani, E., Kagi, H., Jacobsen, S. D., and Ghosh, S. (2007). Temperature dependence and mechanism of hydrogen incorporation in olivine at 12.5-14.0 GPa. Geophysical Research Letters, 34:L16314.

Litasov, K. D., Shatskiy, A., Ohtani, E., and Katsura, T. (2011). Systematic study of hydrogen incorporation into Fe-free wadsleyite. Physics and Chemistry of Minerals, 38:75–84.

Litasov, K. D., Shatskiy, A. F., Katsura, T., and Ohtani, E. (2009). Water solubility in forsterite at 8–-14 GPa. Doklady Earth Sciences, 425A(3):432–435.

Liu, H. and Yang, X. (2020). Solubility of hydroxyl groups in pyroxenes: Effect of oxygen fugacity at 0.2-–3 GPa and 800–-1200℃. Geochimica et Cosmochimica Acta, 286:355–379.

Lu, R. and Keppler, H. (1997). Water solubility in pyrope to 100 kbar. Contributions to Mineralogy and Petrology, 129:35–42.

Mao, Z., Jacobsen, S. D., Frost, D. J., McCammon, C. A., Hauri, E. H., and Duffy, T. S. (2011). Effect of hydration on the single-crystal elasticity of Fe-bearing wadsleyite to 12 GPa. American Mineralogist, 96:1606–1612.

Mao, Z., Jacobsen, S. D., Jiang, F., Smyth, J. R., Holl, C. M., and Duffy, T. S. (2008). Elasticity of hydrous wadsleyite to 12 GPa: Implications for Earth's transition zone. Geophysical Research Letters, 35:1–5.

Mao, Z., Jacobsen, S. D., Jiang, F., Smyth, J. R., Holl, C. M., Frost, D. J., and Duffy, T. S. (2010). Velocity crossover between hydrous and anhydrous forsterite at high pressures. Earth and Planetary Science Letters, 293:250–258.

Mao, Z., Lin, J. F., Jacobsen, S. D., Duffy, T. S., Chang, Y. Y., Smyth, J. R., Frost, D. J., Hauri, E. H., and Prakapenka, V. B. (2012). Sound velocities of hydrous ringwoodite to 16 GPa and 673 K. Earth and Planetary Science Letters, 331-332:112–119.

McSween, H. and Huss, G. R. (2010). Cosmochemistry. Cambridge University Press.

Mierdel, K., Keppler, H., Smyth, J. R., and Langenhorst, F. (2007). Water Solubility in Aluminous Orthopyroxene and the Origin of Earth's Asthenosphere. Science, 315:364–368.

Mookherjee, M. and Karato, S. (2010). Solubility of water in pyrope-rich garnet at high pressures and temperature. Geophysical Research Letters, 37:L03310.

Mosenfelder, J. L., Deligne, N. I., Asimow, P. D., and Rossman, G. R. (2006). Hydrogen incorporation in olivine from 2-12 GPa. American Mineralogist, 91:285–294.

Ohtani, E., Mizobata, H., and Yurimoto, H. (2000). Stability of dense hydrous magnesium silicate phases in the systems Mg_2SiO_4-H_2O and $MgSiO_3$-H_2O at pressures up to 27 GPa. Physics and Chemistry of Minerals, 27:533–544.

Peslier, A. H., Schönbächler, M., Busemann, H., and Karato, S. I. (2017). Water in the Earth's Interior: Distribution and Origin. Space Science Reviews, 212:743–810.

Rauch, M. and Keppler, H. (2002). Water solubility in orthopyroxene. Contributions to Mineralogy and Petrology, 143:525–536.

Sakurai, M., Tsujino, N., Sakuma, H., Kawamura, K., and Takahashi, E. (2014). Effects of Al content on water partitioning between orthopyroxene and olivine: Implications for lithosphere-asthenosphere boundary. Earth and Planetary Science Letters, 400:284–291.

Schulze, K., Marquardt, H., Kawazoe, T., Boffa Ballaran, T., McCammon, C., Koch-Müller, M., Kurnosov, A., and Marquardt, K. (2018). Seismically invisible water in Earth's transition zone? Earth and Planetary Science Letters, 498:9–16.

Smyth, J. R., Frost, D. J., Nestola, F., Holl, C. M., and Bromiley, G. (2006). Olivine hydration in the deep upper mantle: Effects of temperature and silica activity. Geophysical Research Letters, 33(L15301):1 – 5.

Smyth, J. R., Holl, C. M., Frost, D. J., Jacobsen, S. D., Langenhorst, F., and Mccammon, C. A. (2003). Structural systematics of hydrous ringwoodite and water in Earth's interior. American Mineralogist, 88:1402–1407.

Smyth, J. R., Kawamoto, T., Jacobsen, S. D., Swope, R. J., Hervig, R. L., and Holloway, J. R. (1997). Crystal structure of monoclinic hydrous wadsleyite [β-$(Mg, Fe)_2SiO_4$]. American Mineralogist, 82(3-4):270–275.

Stixrude, L. and Lithgow-Bertelloni, C. (2005). Thermodynamics of mantle minerals - I. Physical properties. Geophysical Journal International, 162:610–632.

Stixrude, L. and Lithgow-Bertelloni, C. (2010). Thermodynamics of the Earth's mantle. Reviews in Mineralogy and Geochemistry, 71:465–484.

Stixrude, L. and Lithgow-Bertelloni, C. (2011). Thermodynamics of mantle minerals - II. Phase equilibria. Geophysical Journal International, 184(3):1180–1213.

Stixrude, L. and Lithgow-Bertelloni, C. (2022). Thermal expansivity, heat capacity and bulk modulus of the mantle. Geophysical Journal International, 228:1119–1149.

Stähler, S. C., Khan, A., Banerdt, W. B., Lognonné, P., Giardini, D., Ceylan, S., Drilleau, M., Duran, A. C., Garcia, R. F., Huang, Q., Kim, D., Lekic, V., Samuel, H., Schimmel, M., Schmerr, N., Sollberger, D., Éléonore Stutzmann, Xu, Z., Antonangeli, D., Charalambous, C., Davis, P. M., Irving, J. C. E., Kawamura, T., Knapmeyer, M., Maguire, R., Marusiak, A. G., Panning, M. P., Perrin, C., Plesa, A.-C., Rivoldini, A., Schmelzbach, C., Zenhäusern, G., Éric Beucler, Clinton, J., Dahmen, N., van Driel, M., Gudkova, T., Horleston, A., Pike, W. T., Plasman, M., and Smrekar, S. E. (2021). Seismic detection of the martian core. Science, 373(6553):443–448.

Sun, W., Yoshino, T., Sakamoto, N., and Yurimoto, H. (2018). Supercritical fluid in the mantle transition zone deduced from H–D interdiffusion of wadsleyite. Earth and Planetary Science Letters, 484:309–317.

Tenner, T. J., Hirschmann, M. M., Withers, A. C., and Ardia, P. (2012). H_2O storage capacity of olivine and low-Ca pyroxene from 10 to 13 GPa: Consequences for dehydration melting above the transition zone. Contributions to Mineralogy and Petrology, 163:297–316.

Tenner, T. J., Hirschmann, M. M., Withers, A. C., and Hervig, R. L. (2009). Hydrogen partitioning between nominally anhydrous upper mantle minerals and melt between 3 and 5 GPa and applications to hydrous peridotite partial melting. Chemical Geology, 262:42–56.

Thio, V., Cobden, L., and Trampert, J. (2016). Seismic signature of a hydrous mantle transition zone. Physics of the Earth and Planetary Interiors, 250:46–63.

Wang, D., Mookherjee, M., Xu, Y., and Karato, S.-i. (2006). The effect of water on the electrical conductivity of olivine. Nature, 443:977–980.

Wang, J., Sinogeikin, S. V., Inoue, T., and Bass, J. D. (2003). Elastic properties of hydrous ringwoodite at high-pressure conditions. American Mineralogist, 88:1608–1611.

Withers, A. C. and Hirschmann, M. M. (2007). H_2O storage capacity of $MgSiO_3$ clinoenstatite at 8–13 GPa, 1,100-1,400°C. Contributions to Mineralogy and Petrology, 154:663–674.

Withers, A. C. and Hirschmann, M. M. (2008). Influence of temperature, composition, silica activity and oxygen fugacity on the H_2O storage capacity of olivine at 8 GPa. Contributions to Mineralogy and Petrology, 156:595–605.

Withers, A. C., Hirschmann, M. M., and Tenner, T. J. (2011). The effect of Fe on olivine H_2O storage capacity: Consequences for H_2O in the martian mantle. American Mineralogist, 96:1039–1053.

Withers, A. C., Wood, B. J., and Carroll, M. R. (1998). The OH content of pyrope at high pressure. Chemical Geology, 147:161–171.

Zhang, K., Liu, H., Ionov, D. A., and Yang, X. (2022). Effects of Oxygen Fugacity on Hydroxyl Incorporation in Garnet at 1–-3 GPa and 800-–1000℃and Implications for Water Storage in the Mantle. Journal of Geophysical Research: Solid Earth, 127:e2022JB023948.

Zhao, Y. H., Ginsberg, S. B., and Kohlstedt, D. L. (2004). Solubility of hydrogen in olivine: Dependence on temperature and iron content. Contributions to Mineralogy and Petrology, 147:155–161.

Zhou, W. Y., Ren, Z., Zhang, J. S., Chen, B., Hao, M., Ohuchi, T., Miyagi, L., Zhang, D., Alp, E. E., Lavina, B., and Schmandt, B. (2021). The Water-Fe-Pressure dependent single-crystal elastic properties of wadsleyite: Implications for the seismic anisotropy in the upper Mantle Transition Zone. Earth and Planetary Science Letters, 565:116955.

Chapter 5

Conclusions

The presence and distribution of water in the Earth's interior was introduced in Chapter 1. The origins for water in the Earth's interior, and its effect on various physical properties were discussed. Distinct substitutions mechanisms were highlighted, which helped to better understand the variations in solubility between different mantle phases.

In Chapter 2, Brillouin scattering spectroscopy measurements were presented as clear evidence to confirm the presence of H in the crystal lattice of bridgmanite. The effect of water on the elasticity was isolated using the combination of finite strain fitting and comparison to previous studies on pure and Al-bearing bridgmanite (Murakami et al., 2012, 2007). Based the comparison of these results to geophysical reference models, an insignificant amount of water is expected to be present in the lower mantle. The use of Atom Probe Tomography in this work has been shown to be very useful to determine water contents and investigate its presence in silicate crystal lattices.

In Chapter 3, the phase transition from stishovite to $CaCl_2$-type SiO_2 was experimentally investigated. The transition pressure was determined to be ~30 GPa with Brillouin scattering spectroscopy. This method was found to be very robust, as it directly detected the elastic softening that happens as the crystal lattice transforms from a tetragonal to an orthorhombic configuration. The differential stress in the sample chamber were calculated to be smaller than 1 GPa, and is thus not expected to

significantly influence the transition pressure.

In Chapter 4, an algorithm was used to optimize thermodynamic parameters of hydrous endmembers for all relevant mantle phases present in Mars' mantle, based on available experimental data. Performing such optimizations of geophysical databases based on experimental data, is needed to bring geophysical modeling studies closer to laboratory observations. The interior of Mars is expected to contain the same mineral phases as the Earth's upper mantle and transition zone, even if their exact composition is likely to be different. Findings about the solubility of water in the Earth's mantle phases, and its effect on their elastic properties are therefore also valid for other rocky planetary interiors in which the same phases are expected, like Mars, Venus, Mercury or even rocky exoplanets.

5.1 Future work

The frequent crystallization of an accessory amount of superhydrous phase B during multianvil synthesis of hydrous bridgmanite complicates the quantification of water. *In-situ* synthesis of hydrous bridgmanite in a LHDAC, as was recently achieved by Yang et al. (2023), combined with *in-situ* Infrared Analysis at a Synchrotron source could be a robust enough method to bypass the formation of superhydrous phase B. This way water contents could unambiguously be assigned to bridgmanite and, as a consequence, to the lower mantle. Experimental data on the effect of H on the bulk modulus and its first pressure derivative for hydrous bridgmanite is still outstanding. The same sample used in this work could be measured by Broadband Impulsive Vibrational Spectroscopy to measure pressure wave velocities in a DAC. Moreover, the sample could also be used to perform electrical conductivity measurements. Comparison to geophysical electromagnetic sounding data would allow to reassess the water content of the lower mantle, and whether the conclusions drawn based on the comparison to PREM can be validated. Lastly, determining the exact site occupancy of hydrogen in bridgmanite would be highly valuable information to understand its incorporation mechanism and

allow for more accurate thermodynamic modeling of this phase. This could be achieved by performing Elastic Neutron Scattering measurements at a synchrotron facility.

To test the reproducibility of the stishovite softening observed at 30 GPa, another set of Brillouin measurements could be performed between 20 and 50 GPa using the same sample and a Ne pressure medium. It would also be interesting to test whether the elastic softening also happens when measuring pressure wave velocities. Theoretically, there would be no reason to assume it does not, but it would be valuable to know how intense the drop is to better constrain the interpretation of geophysical observations. Lastly, using Brillouin measurements to further constrain the effect of Al and H on the phase transition would be insightful. For this, stishovite samples containing either Al and H should be measured separately first, before using an Al-H-stishovite.

Once final results on the thermodynamic parameters for all the hydrous mantle endmembers are obtained, their effect on geophysical inversions of the mantle of Mars should be tested. Furthermore, once more experimental studies on water solubility in lower mantle mineral phases will be available, hydrous endmembers for these phases can be created. This would allow for a more robust assessment of the water content in the Earth's lower mantle, which is not singly reliant on a comparison to PREM (Chapt. 2), and where local deviations from the bulk lower mantle water contents could be considered.

Bibliography

A. Suzuki, E. Ohtani, T. K. (2000). A new hydrous phaseδ-AlOOH synthesized at 21 GPa and 1000℃. *Phys Chem Minerals*, 27:689–693.

Amulele, G., ichiro Karato, S., and Girard, J. (2021). Melting of Bridgmanite Under Hydrous Shallow Lower Mantle Conditions. *Journal of Geophysical Research: Solid Earth*, 126.

Andrut, M., Brandstätter, F., and Beran, A. (2003). Trace hydrogen zoning in diopside. *Mineralogy and Petrology*, 78:231–241.

Ardia, P., Hirschmann, M. M., Withers, A. C., and Tenner, T. J. (2012). H 2O storage capacity of olivine at 5-8GPa and consequences for dehydration partial melting of the upper mantle. *Earth and Planetary Science Letters*, 345-348:104–116.

Bali, E., Bolfan-Casanova, N., and Koga, K. T. (2008). Pressure and temperature dependence of H solubility in forsterite: An implication to water activity in the Earth interior. *Earth and Planetary Science Letters*, 268:354–363.

Bell, D. and Rossman, G. (1992). Water in Earth's Mantle: The Role of Nominally Anhydrous Minerals. *Science*, 255(5050):1391–1397.

Bell, D. R., Rossman, G. R., Maldener, J., Endisch, D., and Rauch, F. (2003). Hydroxide in olivine: A quantitative determination of the absolute amount and calibration of the IR spectrum. *Journal of Geophysical Research: Solid Earth*, 108(B2):2105.

Bell, D. R., Rossman, G. R., and Moore, R. O. (2004). Abundance and Partitioning of OH in a High-pressure Magmatic System: Megacrysts from the Monastery Kimberlite, South Africa. *Journal of Petrology*, 45(8):1539–1564.

Bindi, L., Nishi, M., Tsuchiya, J., and Irifune, T. (2014). Crystal chemistry of dense hydrous magnesium silicates: The structure of phase H, $MgSiH_2O_4$, synthesized at 45 GPa and 1000°C. *American Mineralogist*, 99:1802–1805.

Binns, R., Davis, R., and Reed, J. (1969). Ringwoodite, Natural $(Mg, Fe)_2SiO_4$ Spinel in the Tenham Meteorite. *Nature*, 221:943–944.

Bodnar, R., Azbej, T., Becker, S., Cannatelli, C., Fall, A., and Severs, M. (2013). Whole Earth geohydrologic cycle, from the clouds to the core: The distribution of water in the dynamic Earth system. In Bickford, M. E., editor, *The web of geological sciences : advances, impacts, and interactions*, volume 500 of *Special paper / Geological Society of America*, pages 431–461. Boulder, Colorado : The Geological Society of America.

Bolfan-Casanova, N. (2005). Water in the Earth's mantle. *Mineralogical Magazine*, 69:229–257.

Bolfan-Casanova, N., Keppler, H., and Rubie, D. C. (2000). Water partitioning between nominally anhydrous minerals in the MgO-SiO_2-H_2O system up to 24 GPa: Implications for the distribution of water in the Earth's mantle. *Earth and Planetary Science Letters*, 182:209–221.

Bolfan-Casanova, N., Keppler, H., and Rubie, D. C. (2003). Water partitioning at 660 km depth and evidence for very low water solubility in magnesium silicate perovskite. *Geophysical Research Letters*, 30:1–4.

Bolfan-Casanova, N., Mackwell, S., Keppler, H., McCammon, C., and Rubie, D. C. (2002). Pressure dependence of H solubility in magnesiowüstite up to 25 GPa: Implications for the storage of water in the Earth's lower mantle. *Geophysical Research Letters*, 29(10):1449.

Bolfan-Casanova, N., Schiavi, F., Novella, D., Bureau, H., Raepsaet, C., Khodja, H., and Demouchy, S. (2018). Examination of water quantification and incorporation in transition zone minerals: Wadsleyite, ringwoodite and phase D using ERDA (elastic recoil detection analysis). *Frontiers in Earth Science*, 6(76).

Boujibar, A., Bolfan-Casanova, N., Andrault, D., Ali Bouhifd, M., and Trcera, N. (2016). Incorporation of Fe^{2+} and Fe^{3+} in bridgmanite during magma ocean crystallization. *American Mineralogist*, 101:1560–1570.

Bower, D. J., Hakim, K., Sossi, P. A., and Sanan, P. (2022). Retention of Water in Terrestrial Magma Oceans and Carbon-rich Early Atmospheres. *The Planetary Science Journal*, 3:93.

Brodholt, J. (1997). Ab initio calculations on point defects in forsterite (Mg_2SiO_4) and implications for diffusion and creep. *American Mineralogist*, 82:1049–1053.

Bromiley, G. D. and Keppler, H. (2004). An experimental investigation of hydroxyl solubility in jadeite and Na-rich clinopyroxenes. *Contributions to Mineralogy and Petrology*, 147:189–200.

Buchen, J., Marquardt, H., Speziale, S., Kawazoe, T., Boffa Ballaran, T., and Kurnosov, A. (2018). High-pressure single-crystal elasticity of wadsleyite and the seismic signature of water in the shallow transition zone. *Earth and Planetary Science Letters*, 498:77–87.

Chang, Y. Y., Hsieh, W. P., Tan, E., and Chen, J. (2017). Hydration-reduced lattice thermal conductivity of olivine in Earth's upper mantle. *Proceedings of the National Academy of Sciences of the United States of America*, 114(16):4078–4081.

Chen, H., Leinenweber, K., Prakapenka, V., Prescher, C., Meng, Y., Bechtel, H., Kunz, M., and Shim, S. H. (2020). Possible H_2O storage in the crystal structure of $CaSiO_3$ perovskite. *Physics of the Earth and Planetary Interiors*, 299(August 2019):106412.

Chen, J., Inoue, T., Yurimoto, H., and Weidner, D. J. (2002). Effect of water on olivine-wadsleyite phase boundary in the $(Mg, Fe)_2SiO_4$ system. *Geophysical Research Letters*, 29(18):1875.

Chung, J. I. and Kagi, H. (2002). High concentration of water in stishovite in the MORB system. *Geophysical Research Letters*, 29(21):2020.

Churakov, S. V., Khisina, N. R., Urusov, V. S., and Wirth, R. (2003). First-principles study of (MgH_2SiO_4) - n(Mg_2SiO_4) hydrous olivine structures. I. Crystal structure modelling of hydrous olivine Hy-2a (MgH_2SiO_4) - 3(Mg_2SiO_4). *Physics and Chemistry of Minerals*, 30:1–11.

Clesi, V., Bouhifd, M. A., Bolfan-Casanova, N., Manthilake, G., Schiavi, F., Raepsaet, C., Bureau, H., Khodja, H., and Andrault, D. (2018). Low hydrogen contents in the cores of terrestrial planets. *Science Advances*, 4(3).

Cohen-Addad, C., Ducros, P., and Bertaut, E. F. (1967). Étude de la Substitution du Groupement SiO_4 par $(OH)_4$ dans les Composés $Al_2Ca_3(OH)_{12}$ et $Al_2Ca_3(SiO_4)_{2,16}(OH)_{3,36}$ de Type Grenat. *Acta Crystallographica*, 23:220–230.

Corgne, A., Liebske, C., Wood, B. J., Rubie, D. C., and Frost, D. J. (2005). Silicate perovskite-

melt partitioning of trace elements and geochemical signature of a deep perovskitic reservoir. *Geochimica et Cosmochimica Acta*, 69(2):485–496.

Criniti, G., Ishii, T., Kurnosov, A., Glazyrin, K., and Boffa Ballaran, T. (2023). High-pressure phase transition and equation of state of hydrous Al-bearing silica. *American Mineralogist*, 108:1558–1568.

Demouchy, S., Deloule, E., Frost, D. J., and Keppler, H. (2005). Pressure and temperature-dependence of water solubility in Fe-free wadsleyite. *American Mineralogist*, 90:1084–1091.

Deuss, A., Andrews, J., and Day, E. (2013). Seismic Observations of Mantle Discontinuities and Their Mineralogical and Dynamical Interpretation. In Karato, S.-i., editor, *Physics and Chemistry of the Deep Earth*, pages 297–232. John Wiley & Sons, Ltd, first edition.

Di Genova, D., Bondar, D., Zandonà, A., Valdivia, P., Al-Mukadam, R., Fei, H., Withers, A. C., Boffa Ballaran, T., Kurnosov, A., McCammon, C., Deubener, J., and Katsura, T. (2023). Viscosity of anhydrous and hydrous peridotite melts. *Chemical Geology*, 625(121440).

Dodd, D. M. and Fraser, D. B. (1965). The 3000-3900 cm^{-1} absorption bands and anelasticity in crystalline α-quartz. *Journal of Physics and Chemistry of Solids*, 26:673–686.

Drewitt, J. W., Walter, M. J., Brodholt, J. P., Muir, J. M., and Lord, O. T. (2022). Hydrous silicate melts and the deep mantle H_2O cycle. *Earth and Planetary Science Letters*, 581:117408.

Druzhbin, D., Fei, H., and Katsura, T. (2021). Independent hydrogen incorporation in wadsleyite from oxygen fugacity and non-dissociation of H_2O in the reducing mantle transition zone. *Earth and Planetary Science Letters*, 557:116755.

Duan, Y., Sun, N., Wang, S., Li, X., Guo, X., Ni, H., Prakapenka, V. B., and Mao, Z. (2018). Phase stability and thermal equation of state ofδ-AlOOH: Implication for water transportation to the Deep Lower Mantle. *Earth and Planetary Science Letters*, 494:92–98.

Elkins-Tanton, L. T. (2008). Linked magma ocean solidification and atmospheric growth for Earth and Mars. *Earth and Planetary Science Letters*, 271:181–191.

Faccincani, L., Criniti, G., Kurnosov, A., Ballaran, T. B., Withers, A. C., Mazzucchelli, M., Nestola, F., and Coltorti, M. (2023). Sound velocities and single-crystal elasticity of hydrous Fo90 olivine to 12 GPa. *Physics of the Earth and Planetary Interiors*, 337:107011.

Fan, D., Lu, C., Xu, J., Yan, B., Yang, B., and Chen, J. (2017). Effects of water on P-V-T equation of state of pyrope. *Physics of the Earth and Planetary Interiors*, 267:9–18.

Fan, D., Xu, J., Lu, C., Tkachev, S. N., Li, B., Ye, Z., Huang, S., Prakapenka, V. B., and Zhou, W. (2019). Elasticity of single-crystal low water content hydrous pyrope at high-pressure and high-temperature conditions. *American Mineralogist*, 104:1022–1031.

Fei, H. and Katsura, T. (2020). Pressure Dependence of Proton Incorporation and Water Solubility in Olivine. *Journal of Geophysical Research: Solid Earth*, 125.

Fei, H. and Katsura, T. (2021). Water Solubility in Fe-Bearing Wadsleyite at Mantle Transition Zone Temperatures. *Geophysical Research Letters*, 48.

Fei, H., Yamazaki, D., Sakurai, M., Miyajima, N., Ohfuji, H., Katsura, T., and Yamamoto, T. (2017). A nearly water-saturated mantle transition zone inferred from mineral viscosity. *Science Advances*, 3(e1603024).

Férot, A. and Bolfan-Casanova, N. (2012). Water storage capacity in olivine and pyroxene to 14 GPa: Implications for the water content of the Earth's upper mantle and nature of seismic discontinuities. *Earth and Planetary Science Letters*, 349-350:218–230.

Frost, D. J. and Fei, Y. (1998). Stability of phase D at high pressure and high temperature. *Journal of Geophysical Research: Solid Earth*, 103(B4):7463–7474.

Fukao, Y. and Obayashi, M. (2013). Subducted slabs stagnant above, penetrating through, and trapped below the 660 km discontinuity. *Journal of Geophysical Research: Solid Earth*, 118:5920–5938.

Fukuyama, K., Ohtani, E., Shibazaki, Y., Kagi, H., and Suzuki, A. (2017). Stability field of phase Egg, $AlSiO_3OH$ at high pressure and high temperature: Possible water reservoir in mantle transition zone. *Journal of Mineralogical and Petrological Sciences*, 112:31–35.

Gaetani, G. A. and Grove, T. L. (1998). The influence of water on melting of mantle peridotite. *Contributions to Mineralogy and Petrology*, 131:323–346.

Gavrilenko, P., Ballaran, T. B., and Keppler, H. (2010). The effect of Al and water on the compressibility of diopside. *American Mineralogist*, 95:608–616.

Geiger, C. A., Langer, K., Bell, D. R., Rossman, G. R., and Winkler, B. (1991). The hydroxide component in synthetic pyrope. *American Mineralogist*, 76:49–59.

Ghosh, S., Ohtani, E., Litasov, K. D., Suzuki, A., Dobson, D., and Funakoshi, K. (2013). Effect of water in depleted mantle on post-spinel transition and implication for 660 km seismic discontinuity. *Earth and Planetary Science Letters*, 371-372:103–111.

Ghosh, S. and Schmidt, M. W. (2014). Melting of phase D in the lower mantle and implications for recycling and storage of H_2O in the deep mantle. *Geochimica et Cosmochimica Acta*, 145:72–88.

Gu, T., Pamato, M. G., Novella, D., Alvaro, M., Fournelle, J., Brenker, F. E., Wang, W., and Nestola, F. (2022). Hydrous peridotitic fragments of Earth's mantle 660 km discontinuity sampled by a diamond. *Nature Geoscience*, 15:950–954.

Haiber, M., Ballone, P., and Parrinello, M. (1997). Structure and dynamics of protonated Mg_2SiO_4: An ab-initio molecular dynamics study. *American Mineralogist*, 82:913–922.

Hexiong Yang, Prewitt, C. T., and Frost, D. J. (1997). Crystal structure of the dense hydrous magnesium silicate, phase D. *American Mineralogist*, 82:651–654.

Hirose, K. (2006). Postperovskite phase transition and its geophysical implications. *Reviews of Geophysics*, (RG3001).

Hirschmann, M. M. (2006). Water, melting, and the deep Earth H_2O cycle. *Annual Review of Earth and Planetary Sciences*, 34:629–653.

Hirschmann, M. M., Aubaud, C., and Withers, A. C. (2005). Storage capacity of H_2O in nominally anhydrous minerals in the upper mantle. *Earth and Planetary Science Letters*, 236:167–181.

Hirth, G. and Kohlstedt, D. L. (1996). Water in the oceanic upper mantle: Implications for rheology, melt extraction and the evolution of the lithosphere. *Earth and Planetary Science Letters*, 144:93–108.

Hou, M., Zhou, W. Y., Hao, M., Hua, F. T. S., Kung, J., Zhang, D., Dera, P. K., and Zhang, J. S. (2022). Effect of structural water on the elasticity of orthopyroxene. *American Mineralogist*, 107:703–708.

Huang, X., Xu, Y., and Karato, S.-I. (2005). Water content in the transition zone from electrical conductivity of wadsleyite and ringwoodite. *Nature*, 434:746–749.

Hushur, A., Manghnani, M. I., Smyth, J. R., Nestola, F., and Frost, D. J. (2009). Crystal

chemistry of hydrous forsterite and its vibrational properties up to 41 GPa. *American Mineralogist*, 94:751–760.

ichiro Karato, S. (2015). Some notes on hydrogen-related point defects and their role in the isotope exchange and electrical conductivity in olivine. *Physics of the Earth and Planetary Interiors*, 248:94–98.

Ingrin, J. and Blanchard, M. (2006). Diffusion of Hydrogen in Minerals. In Keppler, H. and Smyth, J. R., editors, *Reviews in Mineralogy & Geochemistry: Water in Nominally Anhydrous Minerals*, volume 62, pages 291–320. The Mineralogical Society of America.

Inoue, T., Wada, T., Sasaki, R., and Yurimoto, H. (2010). Water partitioning in the Earth's mantle. *Physics of the Earth and Planetary Interiors*, 183(1-2):245–251.

Inoue, T., Weidner, D. J., Northrup, P. A., and Parise, J. B. (1998). Elastic properties of hydrous ringwoodite (γ-phase) in Mg_2SiO_4. *Earth and Planetary Science Letters*, 160:107–113.

Inoue, T., Yurimoto, H., and Kudoh, Y. (1995). Hydrous modified spinel, $Mg_{1.75}SiH_{0.5}O4$: A new water reservoir in the mantle transition region. *Geophysical Research Letters*, 22(2):117–120.

Irifune, T., Kubo, N., Isshiki, M., and Yamasaki, Y. (1998). Phase transformations in serpentine and transportation of water into the lower mantle. *Geophysical Research Letters*, 25(2):203–206.

Ito, E., Kubo, A., Katsura, T., and Walter, M. J. (2004). Melting experiments of mantle materials under lower mantle conditions with implications for magma ocean differentiation. *Physics of the Earth and Planetary Interiors*, 143:397–406.

Ito, E. and Takahashi, E. (1989). Postspinel Transformations in the System Mg_2SiO_4 -Fe_2SiO_4 and Some Geophysical Implications. *Journal of Geophysical Research*, 94:10637–10646.

Jacobsen, S. D., Demouchy, S., Frost, D. J., Ballaran, T. B., and Kung, J. (2005). A systematic study of OH in hydrous wadsleyite from polarized FTIR spectroscopy and single-crystal X-ray diffraction: Oxygen sites for hydrogen storage in Earth's interior. *American Mineralogist*, 90:61–70.

Jacobsen, S. D., Jiang, F., Mao, Z., Duffy, T. S., Smyth, J. R., Holl, C. M., and Frost, D. J. (2008). Effects of hydration on the elastic properties of olivine. *Geophysical Research Letters*, 35:L14303.

Jacobsen, S. D., Liu, Z., Ballaran, T. B., Littlefield, E. F., Ehm, L., and Hemley, R. J. (2010). Effect of H2O on upper mantle phase transitions in MgSiO3: Is the depth of the seismic X-discontinuity an indicator of mantle water content? *Physics of the Earth and Planetary Interiors*, 183(1-2):234–244.

Jacobsen, S. D. and Smyth, J. R. (2006). Effect of water on the sound velocities of ringwoodite in the transition zone. *Geophysical Monograph Series*, 168:131–145.

Jacobsen, S. D., Smyth, J. R., Spetzler, H., Holl, C. M., and Frost, D. J. (2004). Sound velocities and elastic constants of iron-bearing hydrous ringwoodite. *Physics of the Earth and Planetary Interiors*, 143:47–56.

Jenkins, J., Deuss, A., and Cottaar, S. (2017). Converted phases from sharp 1000 km depth mid-mantle heterogeneity beneath Western Europe. *Earth and Planetary Science Letters*, 459:196–207.

Kakizawa, S., Inoue, T., Nakano, H., Kuroda, M., Sakamoto, N., and Yurimoto, H. (2018). Stability of Al-bearing superhydrous phase B at the mantle transition zone and the uppermost lower mantle. *American Mineralogist*, 103:1221–1227.

Kaneshima, S. and Helffrich, G. (1998). Subduction Zone Using Short-Period Array Data. *Journal of Geophysical Research*, 103:4825–4838.

Kang, L. and Karato, S.-I. (2023). Hydrogen Partitioning Between Olivine and Orthopyroxene: Implications for the Lithosphere-Asthenosphere Structure. *Journal of Geophysical Research: Solid Earth*, 128.

Kanzaki, M. (1991). Stability of hydrous magnesium silicates in the mantle transition zone. *Physics of the Earth and Planetary Interiors*, 66:307–312.

Kanzaki, M. (1993). Calculated powder X-ray patterns of phase B, anhydrous B and superhydrous B: re-assessment of previous studies. *Mineralogical Journal*, 16(5):278–285.

Karato, S. (1990). The role of hydrogen in the electrical conductivity of the upper mantle. *Nature*, 347:272–273.

Karato, S. (2008). Effects of pressure and water. In *Deformation of Earth Materials: An Introduction to the Rheology of Solid Earth*, chapter 10, pages 168–198. Cambridge Universtiy Press.

Karato, S. and Jung, H. (1998). Water, partial melting and the origin of the seismic low velocity and high attenuation zone in the upper mantle. *Earth and Planetary Science Letters*, 157:193–207.

Karato, S. I. (2006). Remote sensing of hydrogen in Earth's mantle. In Keppler, H. and Smyth, J. R., editors, *Reviews in Mineralogy and Geochemistry: Water in Nominally Anhydrous Minerals*, volume 62, pages 343–375. Mineralogical Society of America.

Karato, S. I. (2011). Water distribution across the mantle transition zone and its implications for global material circulation. *Earth and Planetary Science Letters*, 301:413–423.

Karato, S.-I., Karki, B., and Park, J. (2020). Deep mantle melting, global water circulation and its implications for the stability of the ocean mass. *Progress in Earth and Planetary Science*, 7(76).

Karato, S.-I., Paterson, M., and Fitzgerald, D. (1986). Rheology of Synthetic Olivine Aggregates: Influence of Grain Size and Water. *Journal of Geophysical Research*, 91(B8):8151–8176.

Karki, B. B., Ghosh, D. B., and Karato, S.-I. (2021). Behavior and properties of water in silicate melts under deep mantle conditions. *Scientific Reports*, 11:10588.

Katayama, I., Hirose, K., Yurimoto, H., and Nakashima, S. (2003). Water solubility in majoritic garnet in subducting oceanic crust. *Geophysical Research Letters*, 30(22):2155.

Kawamoto, T. (2004). Hydrous phase stability and partial melt chemistry in H_2O-saturated KLB-1 peridotite up to the uppermost lower mantle conditions. *Physics of the Earth and Planetary Interiors*, 143:387–395.

Kawamoto, T., Hervig, R. L., and Holloway, J. R. (1996). Experimental evidence for a hydrous transition zone in the early Earth's mantle. *Earth and Planetary Science Letters*, 142:587–592.

Kelbert, A., Schultz, A., and Egbert, G. (2009). Global electromagnetic induction constraints on transition-zone water content variations. *Nature*, 460:1003–1006.

Keppler, H. and Bolfan-Casanova, N. (2006). Thermodynamics of water solubility and partitioning. *Water in Nominally Anhydrous Minerals*, 62:193–230.

Kind, R., Yuan, X., Saul, J., Nelson, D., Sobolev, S. V., Mechie, J., Zhao, W., Kosarev, G., Ni, J., Achauer, U., and Jiang, M. (2002). Seismic images of crust and upper mantle beneath Tibet: Evidence for Eurasian plate subduction. *Science*, 298:1219–1221.

Kobayashi, S. and Shoji, T. (1983). Infrared analysis of the grossular-hydrogrossular series. *Mineralogical Journal*, 11(7):331–343.

Koch-Müller, M., Matsyuk, S., and Wirth, R. (2004). Hydroxyl in omphacites and omphacitic clinopyroxenes of upper mantle to lower crustal origin beneath the Siberian platform. *American Mineralogist*, 89:921–931.

Koch-Müller, M., Matsyuk, S. S., Rhede, D., Wirth, R., and Khisina, N. (2006). Hydroxyl in mantle olivine xenocrysts from the Udachnaya kimberlite pipe. *Physics and Chemistry of Minerals*, 33:276–287.

Kohlstedt, D. L., Keppler, H., and Rubie, D. C. (1996). Solubility of water in the α, β and γ phases of $(\mathrm{Mg,Fe})_2\mathrm{SiO}_4$. *Contributions to Mineralogy and Petrology*, 123:345–357.

Kohn, S. C. (1996). Solubility of $\mathrm{H_2O}$ in nominally anhydrous mantle minerals using ^{1}H MAS NMR. *American Mineralogist*, 81:1523–1526.

Kovács, I., O'neIll, H. S. C., Hermann, J., and Hauri, E. H. (2010). Site-specific infrared O-H absorption coefficients for water substitution into olivine. *American Mineralogist*, 95:292–299.

Kudoh, Y. (2008). Crystal structural features hydrous forsterite: Effect of Fe on the M-site vacancies, possible hydrogen positions and variation of the unit cell dimensions. *Journal of Mineralogical and Petrological Sciences*, 103:371–375.

Kudoh, Y., Kuribayashi, T., Mizobata, H., and Ohtani, E. (2000). Structure and cation disorder of hydrous ringwoodite, γ-$Mg_{1.89}Si_{0.98}H_{0.30}O_4$. *Phys Chem Minerals*, 27:474–479.

Kudoh, Y., Nagase, T., Sasaki, S., Tanaka, M., and Kanzaki, M. (1997). Phase F, a new hydrous magnesium silicate synthesized at 1000 °C and 17 GPa: Crystal structure and estimated bulk modulus. *Physics and Chemistry of Minerals*, 24(601).

Lakshtanov, D. L., Sinogeikin, S. V., Litasov, K. D., Prakapenka, V. B., Hellwig, H., Wang, J., Sanches-Valle, C., Perrillat, J.-P., Chen, B., Somayazulu, M., Li, J., Ohtani, E., and Bass, J. D. (2007). The post-stishovite phase transition in hydrous alumina-bearing $\mathrm{SiO_2}$ in the lower mantle of the earth. *Proceedings of the National Academy of Sciences*, 104(34):13588–13590.

Lawrence, J. and Wysession, M. E. (2006). Seismic evidence for subduction-transported water in the lower mantle. In Jacobsen, S. D. and van der Lee, S., editors, *Geophyscal Monograph 168: Earth's Deep Water Cycle*, pages 251–261. American Geophysical Union.

Lemaire, C., Kohn, S. C., and Brooker, R. A. (2004). The effect of silica activity on the incorporation mechanisms of water in synthetic forsterite: A polarised infrared spectroscopic study. *Contributions to Mineralogy and Petrology*, 147:48–57.

Li, J., Wang, X., Wang, X., and Yuen, D. A. (2013). P and SH velocity structure in the upper mantle beneath Northeast China: Evidence for a stagnant slab in hydrous mantle transition zone. *Earth and Planetary Science Letters*, 367:71–81.

Li, X., Speziale, S., Koch-Müller, M., Husband, R. J., and Liermann, H. P. (2022). Phase Stability of Al-Bearing Dense Hydrous Magnesium Silicates at Topmost Lower Mantle Conditions: Implication for Water Transport in the Mantle. *Geophysical Research Letters*, 49.

Li, Y., Vočadlo, L., Sun, T., and Brodholt, J. P. (2020). The Earth's core as a reservoir of water. *Nature Geoscience*, 13:453–458.

Libowitzky, E. and Beran, A. (1995). OH defects in forsterite. *Physics and Chemistry of Minerals*, 22:387–392.

Litasov, K. and Ohtani, E. (2008). Systematic study of hydrogen incorporation into Fe-bearing wadsleyite and water storage capacity of the transition zone. *AIP Conference Proceedings*, 987:113–118.

Litasov, K., Ohtani, E., Langenhorst, F., Yurimoto, H., Kubo, T., and Kondo, T. (2003). Water solubility in Mg-perovskites and water storage capacity in the lower mantle. *Earth and Planetary Science Letters*, 211:189–203.

Litasov, K. D. (2010). The influence of Al_2O_3 on the H_2O content in periclase and ferropericlase at 25 GPa. *Russian Geology and Geophysics*, 51:644–649.

Litasov, K. D., Kagi, H., Shatskiy, A., Ohtani, E., Lakshtanov, D. L., Bass, J. D., and Ito, E. (2007a). High hydrogen solubility in Al-rich stishovite and water transport in the lower mantle. *Earth and Planetary Science Letters*, 262:620–634.

Litasov, K. D. and Ohtani, E. (2007). Effect of water on the phase relations in Earth's mantle and deep water cycle. *Special Paper of the Geological Society of America*, Special Pa:115–156.

Litasov, K. D., Ohtani, E., Kagi, H., and Ghosh, S. (2006). Influence of water on olivine-wadsleyite phase transformation and water partitioning near 410-km seismic discontinuity. *AIP Conference Proceedings*, 833(150).

Litasov, K. D., Ohtani, E., Kagi, H., Jacobsen, S. D., and Ghosh, S. (2007b). Temperature dependence and mechanism of hydrogen incorporation in olivine at 12.5-14.0 GPa. *Geophysical Research Letters*, 34:L16314.

Litasov, K. D., Shatskiy, A., Ohtani, E., and Katsura, T. (2011). Systematic study of hydrogen incorporation into Fe-free wadsleyite. *Physics and Chemistry of Minerals*, 38:75–84.

Litasov, K. D., Shatskiy, A. F., Katsura, T., and Ohtani, E. (2009). Water solubility in forsterite at 8–14 GPa. *Doklady Earth Sciences*, 425A(3):432–435.

Liu, C., Yoshino, T., Yamazaki, D., Tsujino, N., Gomi, H., Sakurai, M., Zhang, Y., Wang, R., Guan, L., Lau, K., Tange, Y., and Higo, Y. (2023). Effect of water on seismic attenuation of the upper mantle: The origin of the sharp lithosphere–asthenosphere boundary. *Proceedings of the National Academy of Sciences*, 120(32):e2221770120.

Liu, H. and Yang, X. (2020). Solubility of hydroxyl groups in pyroxenes: Effect of oxygen fugacity at 0.2–3 GPa and 800–1200°C. *Geochimica et Cosmochimica Acta*, 286:355–379.

Liu, L.-g. (1987). Effects of H_2O on the phase behaviour of the forsterite-enstatite system at high pressures and temperatures and implications for the Earth. *Physics of the Earth and Planetary Interiors*, 49:142–167.

Liu, Z., Park, J., and Karato, S.-I. (2016). Seismological detection of low-velocity anomalies surrounding the mantle transition zone in Japan subduction zone. *Geophysical Research Letters*, 43:2480–2487.

Liu, Z., Park, J., and Karato, S.-I. (2018). Seismic evidence for water transport out of the mantle transition zone beneath the European Alps. *Earth and Planetary Science Letters*, 482:93–104.

Lu, R. and Keppler, H. (1997). Water solubility in pyrope to 100 kbar. *Contributions to Mineralogy and Petrology*, 129:35–42.

Maguire, R., Ritsema, J., and Goes, S. (2018). Evidence of Subduction-Related Thermal and Compositional Heterogeneity Below the United States From Transition Zone Receiver Functions. *Geophysical Research Letters*, 45:8913–8922.

Malavergne, V., Bureau, H., Raepsaet, C., Gaillard, F., Poncet, M., Surblé, S., Sifré, D., Shcheka, S., Fourdrin, C., Deldicque, D., and Khodja, H. (2019). Experimental constraints

on the fate of H and C during planetary core-mantle differentiation. Implications for the Earth. *Icarus*, 321:473–485.

Manghnani, M. H., Hushur, A., Smyth, J. R., Nestola, F., Dera, P., Sekar, M., Amulele, G., and Frost, D. J. (2013). Compressibility and structural stability of two variably hydrated olivine samples ($Fo_{97}Fa_3$) to 34 GPa by X-ray diffraction and Raman spectroscopy. *American Mineralogist*, 98:1972–1979.

Mans, W., Zhang, J. S., Hao, M., Smyth, J. R., Zhang, D., Finkelstein, G. J., and Dera, P. (2019). Hydrogen effect on the sound velocities of upper mantle omphacite. *Minerals*, 9:690.

Mao, Z., Jacobsen, S. D., Frost, D. J., McCammon, C. A., Hauri, E. H., and Duffy, T. S. (2011). Effect of hydration on the single-crystal elasticity of Fe-bearing wadsleyite to 12 GPa. *American Mineralogist*, 96:1606–1612.

Mao, Z., Jacobsen, S. D., Jiang, F., Smyth, J. R., Holl, C. M., Frost, D. J., and Duffy, T. S. (2010). Velocity crossover between hydrous and anhydrous forsterite at high pressures. *Earth and Planetary Science Letters*, 293:250–258.

Mao, Z., Jacobsen, S. D., Jiang, F. M., Smyth, J. R., Holl, C. M., Frost, D. J., and Duffy, T. S. (2008). Single-crystal elasticity of wadsleyites, β-Mg_2SiO_4, containing 0.37-1.66 wt.% H_2O. *Earth and Planetary Science Letters*, 268(3-4):540–549.

Mao, Z., Lin, J. F., Jacobsen, S. D., Duffy, T. S., Chang, Y. Y., Smyth, J. R., Frost, D. J., Hauri, E. H., and Prakapenka, V. B. (2012). Sound velocities of hydrous ringwoodite to 16 GPa and 673 K. *Earth and Planetary Science Letters*, 331-332:112–119.

Marquardt, H. and Thomson, A. R. (2020). Experimental elasticity of Earth's deep mantle. *Nature Reviews Earth and Environment*, 1:455–469.

Marzotto, E., Hsieh, W. P., Ishii, T., Chao, K. H., Golabek, G. J., Thielmann, M., and Ohtani, E. (2020). Effect of Water on Lattice Thermal Conductivity of Ringwoodite and Its Implications for the Thermal Evolution of Descending Slabs. *Geophysical Research Letters*, 47.

Mashino, I., Murakami, M., and Ohtani, E. (2016). Sound velocities ofδ-AlOOH up to core-mantle boundary pressures with implications for the seismic anomalies in the deep mantle. *Journal of Geophysical Research: Solid Earth*, 121:595–609.

Matsyuk, S. S. and Langer, K. (2004). Hydroxyl in olivines from mantle xenoliths in kimberlites of the Siberian platform. *Contributions to Mineralogy and Petrology*, 147:413–437.

Mierdel, K. and Keppler, H. (2004). The temperature dependence of water solubility in enstatite. *Contributions to Mineralogy and Petrology*, 148:305–311.

Mierdel, K., Keppler, H., Smyth, J. R., and Langenhorst, F. (2007). Water Solubility in Aluminous Orthopyroxene and the Origin of Earth's Asthenosphere. *Science*, 315:364–368.

Miller, G. H., Rossman, G. R., and Harlow, G. E. (1987). The Natural Occurrence of Hydroxide in Olivine. *Physics and Chemistry of Minerals*, 14:461–472.

Mookherjee, M. and Karato, S. (2010). Solubility of water in pyrope-rich garnet at high pressures and temperature. *Geophysical Research Letters*, 37:L03310.

Mosenfelder, J. L., Deligne, N. I., Asimow, P. D., and Rossman, G. R. (2006). Hydrogen incorporation in olivine from 2-12 GPa. *American Mineralogist*, 91:285–294.

Muir, J. M. and Brodholt, J. P. (2018). Water distribution in the lower mantle: Implications for hydrolytic weakening. *Earth and Planetary Science Letters*, 484:363–369.

Murakami, M., Hirose, K., Yurimoto, H., Nakashima, S., and Takafuji, N. (2002). Water in Earth's Lower Mantle. *Science*, 295:1885–1887.

Murakami, M., Ohishi, Y., Hirao, N., and Hirose, K. (2012). A perovskitic lower mantle inferred from high-pressure, high-temperature sound velocity data. *Nature*, 485:90–94.

Murakami, M., Sinogeikin, S. V., Hellwig, H., Bass, J. D., and Li, J. (2007). Sound velocity of $MgSiO_3$ perovskite to Mbar pressure. *Earth and Planetary Science Letters*, 256:47–54.

Nakajima, A., Sakamaki, T., Kawazoe, T., and Suzuki, A. (2019). Hydrous magnesium-rich magma genesis at the top of the lower mantle. *Scientific Reports*, 9:7420.

Nakatsuka, A., Yoshiasa, A., Ohkawa, M., and Ito, E. (2022). Aluminous hydrous magnesium silicate as a lower-mantle hydrogen reservoir: a role as an agent for material transport. *Scientific Reports*, 12(3594).

Németh, P., Leinenweber, K., Ohfuji, H., Groy, T., Domanik, K. J., Kovács, I. J., Kovács, J. S., and Buseck, P. R. (2017). Water-bearing, high-pressure Ca-silicates. *Earth and Planetary Science Letters*, 469:148–155.

Nishi, M., Irifune, T., Tsuchiya, J., Tange, Y., Nishihara, Y., Fujino, K., and Higo, Y. (2014). Stability of hydrous silicate at high pressures and water transport to the deep lower mantle. *Nature Geoscience*, 7:224–227.

Nisr, C., Leinenweber, K., Prakapenka, V., Prescher, C., Tkachev, S., and Shim, S. H. (2017). Phase transition and equation of state of dense hydrous silica up to 63 GPa. *Journal of Geophysical Research: Solid Earth*, 122:6972–6983.

Niu, F. and Kawakatsu, H. (1996). Complex Structure of Mantle Discontinuities at the Tip of the Subducting Slab beneath Northeast China. *Journal of Physics of the Earth*, 44:701–711.

Niu, F., Kawakatsu, H., and Fukao, Y. (2003). Seismic evidence for a chemical heterogeneity in the midmantle: A strong and slightly dipping seismic reflector beneath the Mariana subduction zone. *Journal of Geophysical Research: Solid Earth*, 108(B9).

Ohira, I., Jackson, J. M., Sturhahn, W., Finkelstein, G. J., Kawazoe, T., Toellner, T. S., Suzuki, A., and Ohtani, E. (2021). The influence ofδ-(Al,Fe)OOH on seismic heterogeneities in Earth's lower mantle. *Scientific Reports*, 11(12036).

Ohira, I., Ohtani, E., Sakai, T., Miyahara, M., Hirao, N., Ohishi, Y., and Nishijima, M. (2014). Stability of a hydrousδ-phase, AlOOH–$MgSiO_2(OH)_2$, and a mechanism for water transport into the base of lower mantle. *Earth and Planetary Science Letters*, 401:12–17.

Ohtani, E. (2015). Hydrous minerals and the storage of water in the deep mantle. *Chemical Geology*, 418:6–15.

Ohtani, E. (2020). The role of water in Earth's mantle. *National Science Review*, 7:224–232.

Ohtani, E. (2021). Hydration and dehydration in earth's interior. *Annual Review of Earth and Planetary Sciences*, 49:253–278.

Ohtani, E., Kudoh, Y., Naito, H., and Arashi, H. (1998). Stability of dense hydrous magnesium silicate phase G in the transition zone and the lower mantle. *Mineralogical Journal*, 20(4):163–169.

Ohtani, E., Mizobata, H., Kudoh, Y., Nagase, T., Arachi, H., Yurimoto, H., and Isoji, M. (1997). A new hydrous silicate, a water reservoir, in the upper part of the lower mantle. *Geophysical Research Letters*, 24(9):1047–1050.

Ohtani, E., Mizobata, H., and Yurimoto, H. (2000). Stability of dense hydrous magnesium

silicate phases in the systems Mg_2SiO_4-H_2O and $MgSiO_3$-H_2O at pressures up to 27 GPa. *Physics and Chemistry of Minerals*, 27:533–544.

Ohtani, E., Toma, M., Kubo, T., Kondo, T., and Kikegawa, T. (2003). In situ X-ray observation of decomposition of superhydrous phase B at high pressure and temperature. *Geophysical Research Letters*, 30(2):1029.

Omori, S., Komabayashi, T., and Maruyama, S. (2004). Dehydration and earthquakes in the subducting slab: Empirical link in intermediate and deep seismic zones. *Physics of the Earth and Planetary Interiors*, 146:297–311.

Ono, S., Mibe, K., and Yoshino, T. (2002). Aqueous fluid connectivity in pyrope aggregates: Water transport into the deep mantle by a subducted oceanic crust without any hydrous minerals. *Earth and Planetary Science Letters*, 203:895–903.

Otsuka, K. and ichiro Karato, S. (2011). Control of the water fugacity at high pressures and temperatures: Applications to the incorporation mechanisms of water in olivine. *Physics of the Earth and Planetary Interiors*, 189(1-2):27–33.

Pacalo, R. and Parise, J. (2000). Crystal structure of superhydrous B, a hydrous magnesium at silicate synthesized 1400°C and 20 GPa. *American Mineralogist*, 77:681–684.

Panero, W., Pigott, J. S., Reaman, D. M., Kabbes, J., and Liu, Z. (2014). Journal of Geophysical Research : Solid Earth. *Journal of Geophysical Research, Solid Earth*, 120:984–908.

Panero, W. R., Thomas, C., Myhill, R., Pigott, J. S., Raepsaet, C., and Bureau, H. (2020). Dehydration Melting Below the Undersaturated Transition Zone. *Geochemistry, Geophysics, Geosystems*, 21.

Pawley, A. R., Mcmillan, P. F., and Holloway, J. R. (2019). Hydrogen in Stishovite , with Implications for Mantle Water Content. *Science*, 261(5124):1024–1026.

Pearson, D. G., Brenker, F. E., Nestola, F., McNeill, J., Nasdala, L., Hutchison, M. T., Matveev, S., Mather, K., Silversmit, G., Schmitz, S., Vekemans, B., and Vincze, L. (2014). Hydrous mantle transition zone indicated by ringwoodite included within diamond. *Nature*, 507:221–224.

Peslier, A. H. (2010). A review of water contents of nominally anhydrous natural minerals in the mantles of Earth, Mars and the Moon. *Journal of Volcanology and Geothermal Research*, 197:239–258.

Peslier, A. H., Schönbächler, M., Busemann, H., and Karato, S. I. (2017). Water in the Earth's Interior: Distribution and Origin. *Space Science Reviews*, 212:743–810.

Pigott, J. S., Wright, K., Gale, J. D., and Panero, W. R. (2015). Calculation of the energetics of water incorporation in majorite garnet. *American Mineralogist*, 100:1065–1075.

Price, G. D., Putnis, A., Agrell, S. O., and Smith, D. G. (1983). Wadsleyite, natural β-$(Mg, Fe)_2SiO_4$ from the Peace River meteorite. *Canadian Mineralogist*, 21:29–35.

Rauch, M. and Keppler, H. (2002). Water solubility in orthopyroxene. *Contributions to Mineralogy and Petrology*, 143:525–536.

Ringwood, A. E. and Major, A. (1967). High-pressure reconnaissance investigations in the system Mg_2SiO_4 - MgO - H_2O. *Earth and Planetary Science Letters*, 2:130–133.

Rossman, G. R., Beran, A., and Langer, K. (1989). The hydrous component of pyrope from the Dora Maira Massif, Western Alps. *European Journal of Mineralogy*, 1:151–154.

Sakamaki, T., Suzuki, A., and Ohtani, E. (2006). Stability of hydrous melt at the base of the Earth's upper mantle. *Nature*, 439:192–194.

Sakurai, M., Tsujino, N., Sakuma, H., Kawamura, K., and Takahashi, E. (2014). Effects of Al content on water partitioning between orthopyroxene and olivine: Implications for lithosphere-asthenosphere boundary. *Earth and Planetary Science Letters*, 400:284–291.

Sano, A., Ohtani, E., Kondo, T., Hirao, N., Sakai, T., Sata, N., Ohishi, Y., and Kikegawa, T. (2008). Aluminous hydrous mineralδ-AlOOH as a carrier of hydrogen into the core-mantle boundary. *Geophysical Research Letters*, 35:L03303.

Sano, A., Ohtani, E., Kubo, T., and Funakoshi, K. I. (2004). In situ X-ray observation of decomposition of hydrous aluminum silicate $AlSiO_3OH$ and aluminum oxide hydroxide d-AlOOH at high pressure and temperature. *Journal of Physics and Chemistry of Solids*, 65:1547–1554.

Sano-Furukawa, A., Kagi, H., Nagai, T., Nakano, S., Fukura, S., Ushijima, D., Iizuka, R., Ohtahtahtani, E., and Yagi, T. (2009). Change in compressibility ofδ-AlOOH andδ-AlOOD at high pressure: A study of isotope effect and hydrogen-bond symmetrization. *American Mineralogist*, 94:1255–1261.

Satta, N., Criniti, G., Kurnosov, A., Boffa Ballaran, T., Ishii, T., and Marquardt, H. (2021).

High-Pressure Elasticity of δ-(Al,Fe)OOH Single Crystals and Seismic Detectability of Hydrous MORB in the Shallow Lower Mantle. *Geophysical Research Letters*, 48.

Schmandt, B., Dueker, K., Humphreys, E., and Hansen, S. (2012). Hot mantle upwelling across the 660 beneath Yellowstone. *Earth and Planetary Science Letters*, 331-332:224–236.

Schmandt, B., Jacobsen, S. D., Becker, T. W., Liu, Z., and Dueker, K. G. (2014). Dehydration melting at the top of the lower mantle. *Science*, 344(6189):12265–1268.

Schönbächler, M., Carlson, R., Horan, M., Mock, T., and Hauri, E. (2010). Heterogeneous Accretion and the Moderately Volatile Element Budget of Earth. *Science*, 328:884–887.

Schulze, K., Marquardt, H., Kawazoe, T., Boffa Ballaran, T., McCammon, C., Koch-Müller, M., Kurnosov, A., and Marquardt, K. (2018). Seismically invisible water in Earth's transition zone? *Earth and Planetary Science Letters*, 498:9–16.

Sheng, Y. M., Xia, Q. K., Dallai, L., Yang, X. Z., and Hao, Y. T. (2007). H_2O contents and D/H ratios of nominally anhydrous minerals from ultrahigh-pressure eclogites of the Dabie orogen, eastern China. *Geochimica et Cosmochimica Acta*, 71:2079–2103.

Shieh, S. R., Mao, H. K., Hemley, R. J., and Ming, L. C. (1998). Decomposition of phase D in the lower mantle and the fate of dense hydrous silicates in subducting slabs. *Earth and Planetary Science Letters*, 159:13–23.

Shim, S. H., Chizmeshya, A., and Leinenweber, K. (2022). Water in the crystal structure of $CaSiO_3$ perovskite. *American Mineralogist*, 107:631–641.

Simmons, N. A. and Gurrola, H. (2000). Multiple seismic discontinuities near the base of the transition zone in the Earth's mantle. *Nature*, 405:559–562.

Simpson, F. and Tommasi, A. (2005). Hydrogen diffusivity and electrical anisotropy of a peridotite mantle. *Geophysical Journal International*, 160:1092–1102.

Skogby, H. (1994). OH incorporation in synthetic clinopyroxene. *American Mineralogist*, 79:240–249.

Skogby, H. (2006). Water in Natural Mantle Minerals I: Pyroxenes. *Reviews in Mineralogy and Geochemistry*, 62:155–167.

Skogby, H., Bell, D. R., and Rossman, G. R. (1990). Hydroxide in pyroxene: variations in the natural environment. *American Mineralogist*, 75:764–774.

Smyth, J. R. and Frost, D. J. (2002). The effect of water on the 410-km discontinuity: An experimental study. *Geophysical Research Letters*, 29(10):123–1–123–4.

Smyth, J. R., Frost, D. J., and Nestola, F. (2005). Hydration of olivine and the Earth's deep water cycle. *Geochimica et Cosmochimica Acta*, 69:A746—-A746.

Smyth, J. R., Holl, C. M., Frost, D. J., Jacobsen, S. D., Langenhorst, F., and Mccammon, C. A. (2003). Structural systematics of hydrous ringwoodite and water in Earth's interior. *American Mineralogist*, 88:1402–1407.

Smyth, J. R. and Jacobsen, S. D. (2006). Nominally Anhydrous Minerals and Earth's Deep Water Cycle. In Jacobsen, S. D. and van der Lee, S., editors, *Geophysical Monograph Series 168: Earth's Deep Water Cycle*, pages 1–12. American Geophysical Union.

Smyth, J. R., Kawamoto, T., Jacobsen, S. D., Swope, R. J., Hervig, R. L., and Holloway, J. R. (1997). Crystal structure of monoclinic hydrous wadsleyite [β-$(\mathrm{Mg,Fe})_2\mathrm{SiO}_4$]. *American Mineralogist*, 82(3-4):270–275.

Song, Z., Wu, Z., Wang, W., Hao, S., and Sun, D. (2022). Elasticity of Phase H Under the Mantle Temperatures and Pressures: Implications for Discontinuities and Water Transport in the Mid-Mantle. *Journal of Geophysical Research: Solid Earth*, 127.

Stalder, R. (2002). Synthesis of enstatite single crystals at high pressure. pages 637–640.

Stocker, R. L. and Gordon, R. B. (1975). Velocity and internal friction in partial melts. *Journal of Geophysical Research*, 80(35):4828–4836.

Su, X., Liu, J., Zhuang, Y., Lv, C., Pang, X., Liu, F., Yu, X., and Sun, Q. (2023). High-pressure electrical conductivity and elasticity of iron-bearingδ-AlOOH. *American Mineralogist*, 108:950–958.

Su, X., Zhao, C., Lv, C., Zhuang, Y., Salke, N., Xu, L., Tang, H., Gou, H., Yu, X., Sun, Q., and Liu, J. (2021). The effect of iron on the sound velocities ofδ-AlOOH up to 135 GPa. *Geoscience Frontiers*, 12:937–946.

Suetsugu, D., Inoue, T., Yamada, A., Zhao, D., and Obayashi, M. (2006). Towards Mapping the Three-dimensional Distribution of Water in the Transition Zone From P-Velocity Tomography and 660-km Discontinuity Depths. In Jacobsen, S. and van der Lee, S., editors, *Geophyscal Monograph 168: Earth's Deep Water Cycle*, pages 237–250. American Geophysical Union.

Sun, W., Yoshino, T., Sakamoto, N., and Yurimoto, H. (2018). Supercritical fluid in the mantle transition zone deduced from H–D interdiffusion of wadsleyite. *Earth and Planetary Science Letters*, 484:309–317.

Takei, Y. (2002). Effect of pore geometry on V_P/V_S : From equilibrium geometry to crack. *Journal of Geophysical Research: Solid Earth*, 107(B2).

Tauzin, B., Van Der Hilst, R. D., Wittlinger, G., and Ricard, Y. (2013). Multiple transition zone seismic discontinuities and low velocity layers below western United States. *Journal of Geophysical Research: Solid Earth*, 118:2307–2322.

Tenner, T. J., Hirschmann, M. M., Withers, A. C., and Ardia, P. (2012). H_2O storage capacity of olivine and low-Ca pyroxene from 10 to 13 GPa: Consequences for dehydration melting above the transition zone. *Contributions to Mineralogy and Petrology*, 163:297–316.

Tenner, T. J., Hirschmann, M. M., Withers, A. C., and Hervig, R. L. (2009). Hydrogen partitioning between nominally anhydrous upper mantle minerals and melt between 3 and 5 GPa and applications to hydrous peridotite partial melting. *Chemical Geology*, 262:42–56.

Townsend, J. P., Tsuchiya, J., Bina, C. R., and Jacobsen, S. D. (2016). Water partitioning between bridgmanite and postperovskite in the lowermost mantle. *Earth and Planetary Science Letters*, 454:20–27.

Tschauner, O., Chi, M., Beckett, J. R., Prescher, C., Prakapenka, V. B., and Rossman, G. R. (2014). Discovery of bridgmanite, the most abundant mineral in Earth, in a shocked meteorite. *Science*, 346(6213):1100–1102.

Tsuchiya, J. (2013). First principles prediction of a new high-pressure phase of dense hydrous magnesium silicates in the lower mantle. *Geophysical Research Letters*, 40:4570–4573.

Tsuchiya, J. and Tsuchiya, T. (2009). Elastic properties ofδ-AlOOH under pressure: First principles investigation. *Physics of the Earth and Planetary Interiors*, 174:122–127.

Tsuchiya, T. and Tsuchiya, J. (2006). Effect of impurity on the elasticity of perovskite and post-perovskite: Velocity contrast across the postperovskite transition in $(\mathrm{Mg,Fe,Al})(\mathrm{Si,Al})\mathrm{O_3}$. *Geophysical Research Letters*, 33(L12S04).

Umemoto, K., Wentzcovitch, R. M., Hirschmann, M. M., Kohlstedt, D. L., and Withers, A. C. (2011). A first-principles investigation of hydrous defects and IR frequencies in forsterite: The case for Si vacancies. *American Mineralogist*, 96:1475–1479.

Walker, A. M., Demouchy, S., and Wright, K. (2006). Computer modelling of the energies and vibrational properties of hydroxyl groups in α- and β-Mg_2SiO_4. *European Journal of Mineralogy*, 18:529–543.

Wang, B., Zhang, Y., Fu, S., Yan, W., Takahashi, E., Li, L., Lin, J. F., and Song, M. (2022). Single-crystal elasticity of phase Egg $AlSiO_3OH$ andδ-AlOOH by Brillouin spectroscopy. *American Mineralogist*, 107:147–152.

Wang, D., Mookherjee, M., Xu, Y., and Karato, S.-i. (2006a). The effect of water on the electrical conductivity of olivine. *Nature*, 443:977–980.

Wang, J., Sinogeikin, S. V., Inoue, T., and Bass, J. D. (2003). Elastic properties of hydrous ringwoodite at high-pressure conditions. *American Mineralogist*, 88:1608–1611.

Wang, J., Sinogeikin, S. V., Inoue, T., and Bass, J. D. (2006b). Elastic properties of hydrous ringwoodite at high-pressure conditions. *Geophysical Research Letters*, 33:2–5.

Wang, W., Walter, M. J., Peng, Y., Redfern, S., and Wu, Z. (2019). Constraining olivine abundance and water content of the mantle at the 410-km discontinuity from the elasticity of olivine and wadsleyite. *Earth and Planetary Science Letters*, 519:1–11.

Waszek, L., Schmerr, N. C., and Ballmer, M. D. (2018). Global observations of reflectors in the mid-mantle with implications for mantle structure and dynamics. *Nature Communications*, 9:385.

Weidner, D. J. and Wang, Y. (1998). Chemical- and Clapeyron-induced buoyancy at the 660 km discontinuity. *Journal of Geophysical Research*, 103:7431–7441.

Wirth, R., Vollmer, C., Brenker, F., Matsyuk, S., and Kaminsky, F. (2007). Inclusions of nanocrystalline hydrous aluminium silicate "Phase Egg" in superdeep diamonds from Juina (Mato Grosso State, Brazil). *Earth and Planetary Science Letters*, 259:384–399.

Withers, A. C. and Hirschmann, M. M. (2007). H_2O storage capacity of $MgSiO_3$ clinoenstatite at 8-13 GPa, 1,100-1,400°C. *Contributions to Mineralogy and Petrology*, 154:663–674.

Withers, A. C. and Hirschmann, M. M. (2008). Influence of temperature, composition, silica activity and oxygen fugacity on the H_2O storage capacity of olivine at 8 GPa. *Contributions to Mineralogy and Petrology*, 156:595–605.

Withers, A. C., Hirschmann, M. M., and Tenner, T. J. (2011). The effect of Fe on olivine

H_2O storage capacity: Consequences for H_2O in the martian mantle. *American Mineralogist*, 96:1039–1053.

Withers, A. C., Wood, B. J., and Carroll, M. R. (1998). The OH content of pyrope at high pressure. *Chemical Geology*, 147:161–171.

Wood, B. (1995). The Effect of H_2O on the 410-Kilometer Seismic Discontinuity. *Science*, 268(5207):74–76.

Wookey, J., Kendall, J. M., and Barruol, G. (2002). Mid-mantle deformation inferred from seismic anisotropy. *Nature*, 415:777–780.

Wright, K. (2006). Atomistic models of OH defects in nominally anhydrous minerals. In Keppler, H. and Smyth, J. R., editors, *Reviews in Mineralogy & Geochemistry: Water in Nominally Anhydrous MineralsWater in Nominally Anhydrous Minerals*, volume 62, pages 67–84.

Xia, Q. K., Sheng, Y. M., Yang, X. Z., and Yu, H. M. (2005). Heterogeneity of water in garnets from UHP eclogites, eastern Dabieshan, China. *Chemical Geology*, 224:237–246.

Xu, C. and Inoue, T. (2019). Melting of Al-Rich Phase D up to the Uppermost Lower Mantle and Transportation of H_2O to the Deep Earth. *Geochemistry, Geophysics, Geosystems*, 20:4382–4389.

Xue, X., Kanzaki, M., Turner, D., and Loroch, D. (2017). Hydrogen incorporation mechanisms in forsterite: New insights from ^{1}H and ^{29}Si NMR spectroscopy and first-principles calculation. *American Mineralogist*, 102(3):519–536.

Yamada, A., Inoue, T., and Irifune, T. (2004). Melting of enstatite from 13 to 18 GPa under hydrous conditions. *Physics of the Earth and Planetary Interiors*, 147:45–56.

Yang, Y. N., Du, Z., Lu, W., Qi, Y., Zhang, Y. Q., Zhang, W. F., and Zhang, P. F. (2023). NanoSIMS analysis of water content in bridgmanite at the micron scale: An experimental approach to probe water in Earth's deep mantle. *Frontiers in Chemistry*, 11.

Ye, Y., Brown, D. A., Smyth, J. R., Panero, W. R., Jacobsen, S. D., Chang, Y. Y., Townsend, J. P., Thomas, S. M., Hauri, E. H., Dera, P., and Frost, D. J. (2012). Compressibility and thermal expansion of hydrous ringwoodite with 2.5(3) wt% H_2O. *American Mineralogist*, 97:573–582.

Yusa, H. and Inoue, T. (1998). Compressibility of hydrous wadsleyite (β-phase) in Mg_2SiO_4 by high pressure X-ray diffraction. *Geophysical Research Letters*, 24(14):1831–1834.

Zhang, H., Egbert, G. D., and Huang, Q. (2022a). A relatively dry mantle transition zone revealed by geomagnetic diurnal variations. *Science Advances*, 8:eabo3293.

Zhang, K., Liu, H., Ionov, D. A., and Yang, X. (2022b). Effects of Oxygen Fugacity on Hydroxyl Incorporation in Garnet at 1–3 GPa and 800–1000°C and Implications for Water Storage in the Mantle. *Journal of Geophysical Research: Solid Earth*, 127:e2022JB023948.

Zhang, Y., Fu, S., ichiro Karato, S., Okuchi, T., Chariton, S., Prakapenka, V. B., and Lin, J. F. (2022c). Elasticity of Hydrated Al-Bearing Stishovite and Post-Stishovite: Implications for Understanding Regional Seismic VS Anomalies Along Subducting Slabs in the Lower Mantle. *Journal of Geophysical Research: Solid Earth*, 127:e2021JB023170.

Zhao, Y. H., Ginsberg, S. B., and Kohlstedt, D. L. (2004). Solubility of hydrogen in olivine: Dependence on temperature and iron content. *Contributions to Mineralogy and Petrology*, 147:155–161.

Zhou, W. Y., Ren, Z., Zhang, J. S., Chen, B., Hao, M., Ohuchi, T., Miyagi, L., Zhang, D., Alp, E. E., Lavina, B., and Schmandt, B. (2021). The Water-Fe-Pressure dependent single-crystal elastic properties of wadsleyite: Implications for the seismic anisotropy in the upper Mantle Transition Zone. *Earth and Planetary Science Letters*, 565:116955.

Zhu, H., Bozdağ, E., Duffy, T. S., and Tromp, J. (2013). Seismic attenuation beneath Europe and the North Atlantic: Implications for water in the mantle. *Earth and Planetary Science Letters*, 381:1–11.